DYNAMIC STALL CHARACTERISTICS OF A PITCHING SWEPT FINITE ASPECT RATIO WING

A Thesis
Submitted to the Graduate Facility
of the
North Dakota State University
of Agriculture and Applied Science

By

Kristopher Ladd Tomek

In Partial Fulfillment of the Requirements
for the Degree of
MASTER OF SCIENCE

Major Department:
Mechanical Engineering

April 2019

Fargo, North Dakota

North Dakota State University
Graduate School

Title

Dynamic Stall Characteristics of a Pitching Swept Finite Aspect Ratio Wing

By

Kristopher Ladd Tomek

The Supervisory Committee certifies that this ***disquisition*** complies with North Dakota State University's regulations and meets the accepted standards for the degree of

MASTER OF SCIENCE

SUPERVISORY COMMITTEE:

Dr. Jordi Estevadeordal
Chair

Dr. Yildirim Suzen

Dr. Majura Selekwa

Dr. Jacob Glower

Approved:

4/16/19
Date

Dr. Alan Kallmeyer
Department Chair

ABSTRACT

This research will investigate various swept wing models, designing the mechanism for their pitching motion and control, designing wind tunnel implementation, and performing data measurements and analysis using particle image velocimetry. A NACA0012 section with an aspect ratio of AR = 4, free stream velocity of U_∞=34 m/s, and Reynolds Number is $Re_c=2x10^5$. Swept airfoils of Λ=0°, 15°, and 30° will be pitched sinusoidally between an AoA of 4°and 22°, at a reduced frequency of $k=\pi fc/U_\infty=0.2$. Higher sweep angles developing arch-type vortices interact with wing tip flow and abrupt tip stall is observed. Lower sweep angles possessed defined leading edge vortices persist near the tip after lift has collapsed at mid span. Stall angle was delayed during dynamic motion of the wing as well as the presence of arch and ring type vortices increased with sweep angle and contributed to flow reattachment along the top surface of the wing.

ACKNOWLEDGEMENTS

Air Force Research Laboratory, Wright-Patterson AFB, OH for the computational results, wing fabrication, and funding the equipment used in this research.

Al Habib Ullah and Charles Fabijanic for all their time and hard work assisting in testing.

DEDICATION

Dedicated to my Mother for all her love and encouragement throughout my graduate education.

TABLE OF CONTENTS

LIST OF FIGURES

Figure Page

LIST OF ABBREVIATIONS

AFRL	.....	air force research laboratory
DSV	.....	dynamic stall vortex
LEV	.....	leading edge vortex
LSB	.....	laminar separation bubble
M	.....	Mach number
PIV	.....	Particle Image Velocimetry
PSP	.....	Pressure Sensitive Paint

LIST OF SYMBOLS

c	.....	wing chord length
C_L	.....	lift coefficient about quarter chord
C_D	.....	drag coefficient about quarter chord
C_M	.....	moment coefficient about quarter chord
f	.....	frequency (Hz)
k	.....	reduced frequency
t	.....	time (seconds)
U_∞	.....	free stream velocity
α	.....	angle of attack
α	.....	pitching rate (°/second)
γ	.....	specific heat ratio (=1.4 for air)
Λ	.....	sweep angle
ρ_∞	.....	free stream density
Ω	.....	pitching rate (rad/sec)

CHAPTER 1. INTRODUCTION

Purpose

The understanding of the quasistatic aerodynamic stall characteristics of a fixed aspect ratio wing has been thoroughly studied and well understood in industry throughout time. Though commercial applications of these quasistatic wings goes well beyond a constant wing geometry, aerodynamic performance regarding dynamic motion and the stall performance of a wing is still a current area of research. With the growing interest in small, unmanned aerial vehicles capable of performing swift, sharp maneuvers, and nimble maneuvers, demonstrations of this type and application of flight hold value in this area of research. Computational analysis of a pitching wing has been conducted exhaustively, but the empirical data which demonstrates this has further yet to be explored. By having a greater understanding with both computational and empirical data of a wings dynamic stall performance will give us a better understanding of the application and improvements that can be implemented.

Thesis Outline

This thesis aims to provide an experimental demonstration of a wings dynamic stall performance and provide affirmation to current computational research. The following section, Chapter 2, provides background and history for the application of similar swept wings and the current understanding of their stall performance. Further details about the current computational research being conducted is explored in the subsequent Chapter 3. This chapter explains the parameters which the wings under testing will be subject to as well as provide a scope of evaluation to build an outline for following chapters. Results have been taken from prior work conducted by the Air Force Research Laboratory and will be used for evaluation concurrently alongside the

discussion in later chapters. Chapter 4 describes the experimental setup and how the empirical results were actually captured to generate the results of this experiment and all associated methods and parameters. A variety of equipment were used and a special apparatus was constructed for this experiment and are discussed in this chapter. Chapter 5 contains data from the experiment including snapshots of the flow at particular states as well as their generated vector fields which reflect their performance. Additionally, certain properties under potential consideration are explored here. This chapter also discusses more details about the actual experiment, hypothetical considerations, suspected issues with experiment, and potential future work. Lastly, Chapter 6 condenses all of the results from the previous chapters into a concise summary of the results and provides information regarding potential future work which can be done to continue this subject of study.

CHAPTER 2. BACKGROUND

An airfoil that experiences an unsteady increase in incidence which carries it beyond its static stall angle is known to develop an increase in lift without any detectable change in the lift-curve slope [1]. This has been observed in modern application of swept wings also extends into other air vehicles such as helicopter rotors, wind turbines, and other maneuvering aircraft such as unmanned aerial vehicles and other aircraft systems. These subsonic applications utilize swept wings for a variety of reasons including stability, low perturbation velocities at low Mach numbers, and prolonged critical value of pressure coefficient [2]. The dynamic stall process is characterized by the formation and propagation of large-scale dynamic stall vortex (DSV) that induces undesirable variations in aerodynamic forces and moments [3]. Though the stall characteristics of a static, pitched airfoil are known for sweep angles less than 15°, further detail about the complex 3D unsteady flow remain to be explored. The interactions of the formation of the 3D unsteady flow components of dynamic stall characteristics and their influence on a wings aerodynamic performance will be the highlight of this investigation. Dynamic Stall is used to describe the complex, 3D flow, which is observed during large amplitude motion of aerodynamic bodies or lifting surfaces [4]. Because the application of subsonic flow over a swept airfoil has broad applications including unmanned aerial vehicles, helicopter and prop aircraft rotors, and wind turbines, a greater understanding of the nature of the complex flow these applications possess, can potentially increase their effectiveness in their respective industries in the near future. Various models and cases of computational fluid dynamics have been exhaustively performed since the late 1980's, but further, empirical demonstration of this particular case is yet to be fulfilled.

It is generally observed that as an airfoil pitches upward, it will reach a point where a surge in the airfoils lift force and a negative roll off in pitching moment occurs. Additionally, it can be

seen that a vortex will begin to grow and shed from the leading edge region on the top surface relative to flow direction. This region of flow reversal is also known as the Laminar Separation Bubble and is typically indicative of the early stages of flow reversal. This separation region grows until the reattachment region near the trailing edge separates from the airfoil surface and a sudden loss in lift occurs [1]. In order to gain a reference to compare the dynamic performance of an airfoil, we must first consider the airfoils static performance. The static performance of the NACA0012 airfoil is very well understood and much data of its static performance is readily available. Figure 1 below shows the Static Lift Performance of a NACA 0012 Airfoil from the NASA Langley Research Center.

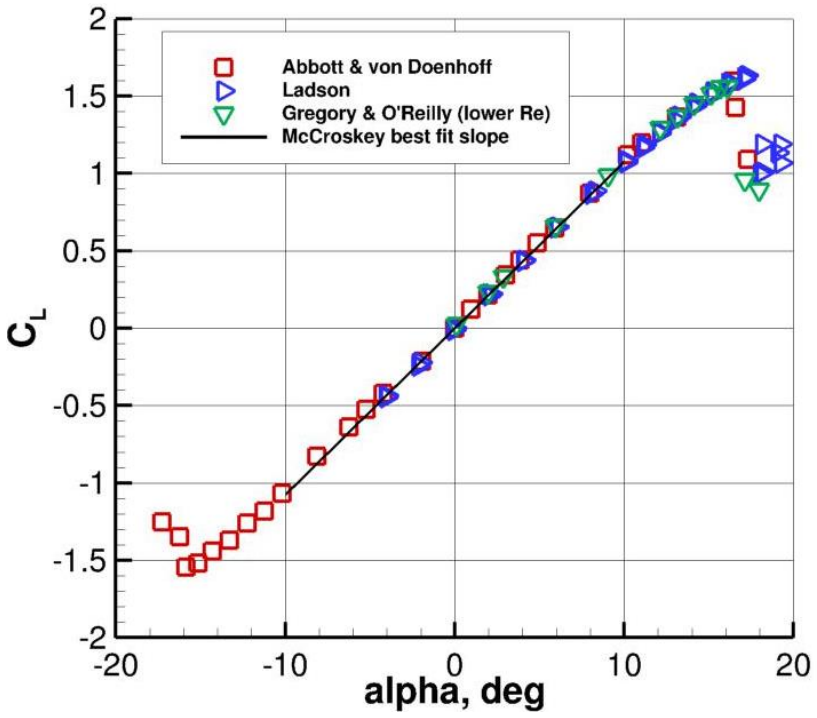

Figure 1. Static lift performance of a NACA 0012 airfoil [5]

For incompressible flow, the NACA 0012 Airfoil has a static stall angle of approximately 16º relative to the direction of flow. It should also be noted that this data is for an unswept (Λ=0º) NACA 0012 airfoil

For a swept airfoil of a finite aspect ratio, the effects of wingtip and leading edge vortices and their effect of downwash, drag, and flow separation regarding its aerodynamic performance at static pitching angles, are well understood. Though these events which together make up 3D flow, its complexity goes beyond the Prandtl lifting-line theory as the interaction of these events is dependent on a number of factors including dynamic wing geometry, turbulent flow models, free stream properties and more, as suggested by computational results[6]. Though contemporary practices which mitigate the undesired effects of wing tip vortices such as winglets, the computational results used for comparison simply possess a simple, rounded tip. This simpler geometry may decrease the actual effectiveness of the wing, but to our benefit the lower complexity will contribute to both simpler calculations and a more prominent effect in the actual experiment. Thus, the wing tip vortices and its resulting effects and how they interact with other dynamic stall characteristics, will be easier to observe. Additionally, the effect of leading edge vortices is rather dependent on apparent angle of attack. It is expected that the magnitude of these effects will increase significantly with angle in respect to flow. This is not to dismiss the other major affects which contribute to leading edge vortices like aspect ratio and wing profile, however, for the sake of simplicity, these factors will both be held at a constant. The effects of leading edge vortices is expected to be rather prominent as the wing being tested can be considered to be a "non-slender" wing due to its relatively moderate aspect ratio[7]. Furthermore, these effects should be observable to the formation of a Laminar Separation Bubble. Several computational studies have shown a strong presence of a laminar separation bubble and its formation over a finite wing, thus, its affects and formation will be closely observed during the experimentation. It is previously known that is that sweep angle has the potential to strongly influence the effects of both previously described effects, hence, a strong emphasis will be placed on understanding the effect of sweep

angle on this 3D complex flow and its vertical components. It is anticipated that the effects of the wingtip vortices will have a strong influence on flow separation further down the span of the wing. This interaction is expected to create a station of secondary vorticity near the trailing edge above the surface separate from the laminar separation region.

CHAPTER 3. PRELIMINARY RESULTS

Preliminary Overview

Extensive computational analysis of a pitching swept wing has been conducted by the AFRL and the computational results from Visbal and Garmann's "Computational Investigation of the Effect of Sweep on a Pitching Finite-Aspect-Ratio Wing" will be used for this analysis. This practical experimental investigation will strive to reconstruct the computational experiment and to affirm its results by using NDSU's advanced flow diagnostic tools including PIV and Tomographic PSP and lab equipment constructed specifically for this experiment. The airfoil will first be tested at a various, stationary pitching angles and then will be pitched at a given frequency between a minimum and maximum pitching angle. Because the major use of an airfoil is dependent on its pitching angle in respect to flow direction, the following experiments will include minimum and maximum angles of attack between $\alpha = 4°$ and 22°, respectively pertaining to the NACA0012. Base parameters for flow and the selected airfoil to demonstrate these dynamic stall properties were previously investigated by Visbal and Garmann[8], who established a moderate aspect ratio of AR = 4 and chord Reynolds number of $Re_c = 2x10^5$ will be selected for this experiment. Additionally, in order to neglect compressibility effects, a free stream velocity of $M_\infty = 0.1$ will also be used. The airfoils will be pitch sinusoidally with a nominal reduced frequency of $k = \pi fc/U_\infty = 0.2$.

Three different sweep angles of the same finite airfoil will all be tested equally. The influence of sweep angle on both major effects and their resulting interactions will be closely observed. Three different sweep angles of the same NACA0012, finite aspect ratio (AR=4) airfoils will be subject to the rapid pitching motion. These three sweep angles include $\Lambda = 0°$, 15°, and 30°, swept backwards relative to the span wise direction. Recent computational results conducted

by Visbal and Garmann[8] indicate that for $\Lambda = 0°$ sweep angle, arch vortices formed on the side of the wing due to the interacting leading edge and wing tip vortices develop at a span wise location and moves farther towards the wing tip as sweep angle is increased. Additionally, the dynamic stall vortices evolve into an arch type vortex which is then shed from the top surface of the wing following its transformation into a ring shaped vortex. Velocity and pressure distribution in the span wise direction of the wing will be evaluated at various span position along the wing, mainly near the wing tip and leading edge. The following sections explore the computational results and highlight certain areas of interest which contribute to dynamic stall while performing a pitching maneuver as well as some particular behaviors of these wings and the effects that sweep and pitching angle incur on its performance. Understanding these effects can help improve this wing's performance and expand its area of applicability in low speed flow.

Experimental Parameters

It is desired to recreate the flow as closely to the computational experiment as possible. Therefore, all parameters including free stream velocity, temperature, pitching frequency, pitching angle, etc. can all be controlled and will be done so to reflect the computational experiment. Details of the actual computational fluid dynamics, its discretization, mesh, and solving method can be found in Visbal and Garmann's research paper previously mentioned.

Free Stream Flow Parameters

In order to neglect compressibility effects, a relatively low freestream Mach number is used at $M_\infty = 0.1$ (or approximately 34.6 m/s at T = 25ºC). The Reynolds number based on the wing

chord will be $Re_c = 2x10^5$. Furthermore, kinematic viscosity is taken at the same ambient temperature and will be $\nu = 1.562x10^{-5}$ m^2/s.

Wing and Pitching Rate Parameters

The wings have a nominal aspect ratio AR = b/c = 4 and have wing tip geometry rounded at the end by one half of the airfoil's profile about its symmetry line. The minimum and maximum pitching angles relative to the free stream flow will be $\alpha_{min} = 4^o$ and $\alpha_{max} = 22^o$, respectively, giving a maximum pitching range of $\Delta\alpha = \alpha_{max} - \alpha_{min} = 18^o$. With this pitching range and the controlled environment defined by the free stream flow parameters, a nominal reduced frequency of $k = \pi fc/U_\infty = 0.2$ is chosen. Discussed in detail later, if the wing chord is c = 76.2 mm, the resulting actuating frequency, *f* will equate to be approximately 34.2 Hz.

Scope and Domain of Analysis

The scope of this analysis will mainly be focused on the top surface of the airfoil while undergoing a pitching maneuver. Freestream flow immediately before and after the airfoil will also be considered in order to gain information about how the incident flow will interact with the airfoil as well as how flow is shed from the airfoil. Areas which contribute to the stall performance of the airfoil such as the leading edge, top surface, and wing tip will be of the greater focus. The scope of this investigation is on the qualitative analysis of these airfoils and to affirm the computational results provided. Each air foil with the three different sweep angles will all be considered at various stations along the wingspan. Due to limitations of the available equipment during the time of this analysis and restrictions of the wind tunnel, flow will be evaluated at x/c= 0.4, 0.6, 0.8 and 1.0 of the wing span. PIV will be conducted at each of these stations for every

sweep angle. Substantial data should be extracted from this domain for analysis with the selected method. Figure 2 below shows the desired locations where data will be captured.

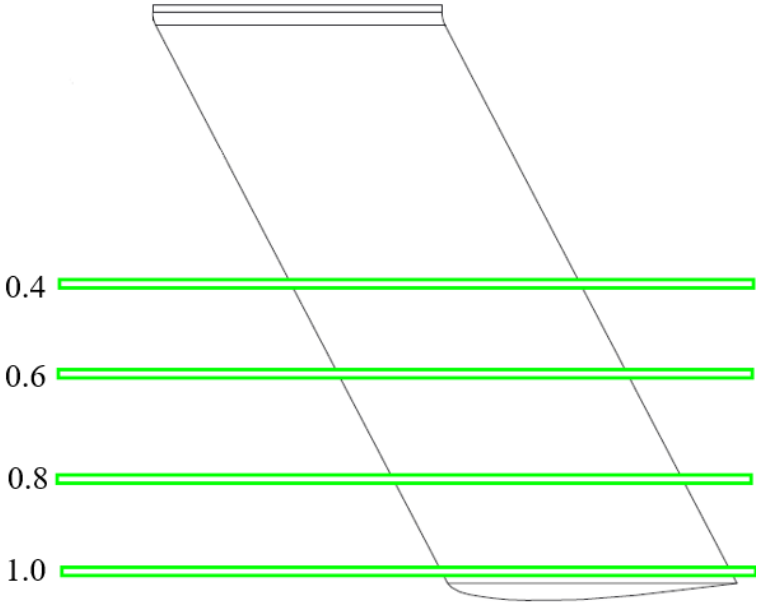

Figure 2. Spanwise locations of data collection

The reason why data will only be captured at these locations and not closer to the wing root is due to the performance and visible area from top surface of the wind tunnel. Though it would be ideal to capture more data near the wing root, these four sections should provide a substantial amount of data for the scope of this analysis.

Flow Structure and Reversal

According the Kutta Condition, which states that "A body with a sharp trailing edge which is moving through a fluid will create about itself a circulation of sufficient strength to hold the rear stagnation point at the trailing edge," flow reversal is strongly indicative of complete stall where flow becomes completely detached from the object surface. Flow reversal can be easily observed with the mode of two dimensional PIV used in this investigation and will be useful for understanding when the airfoil will stall and when flow completely detaches.

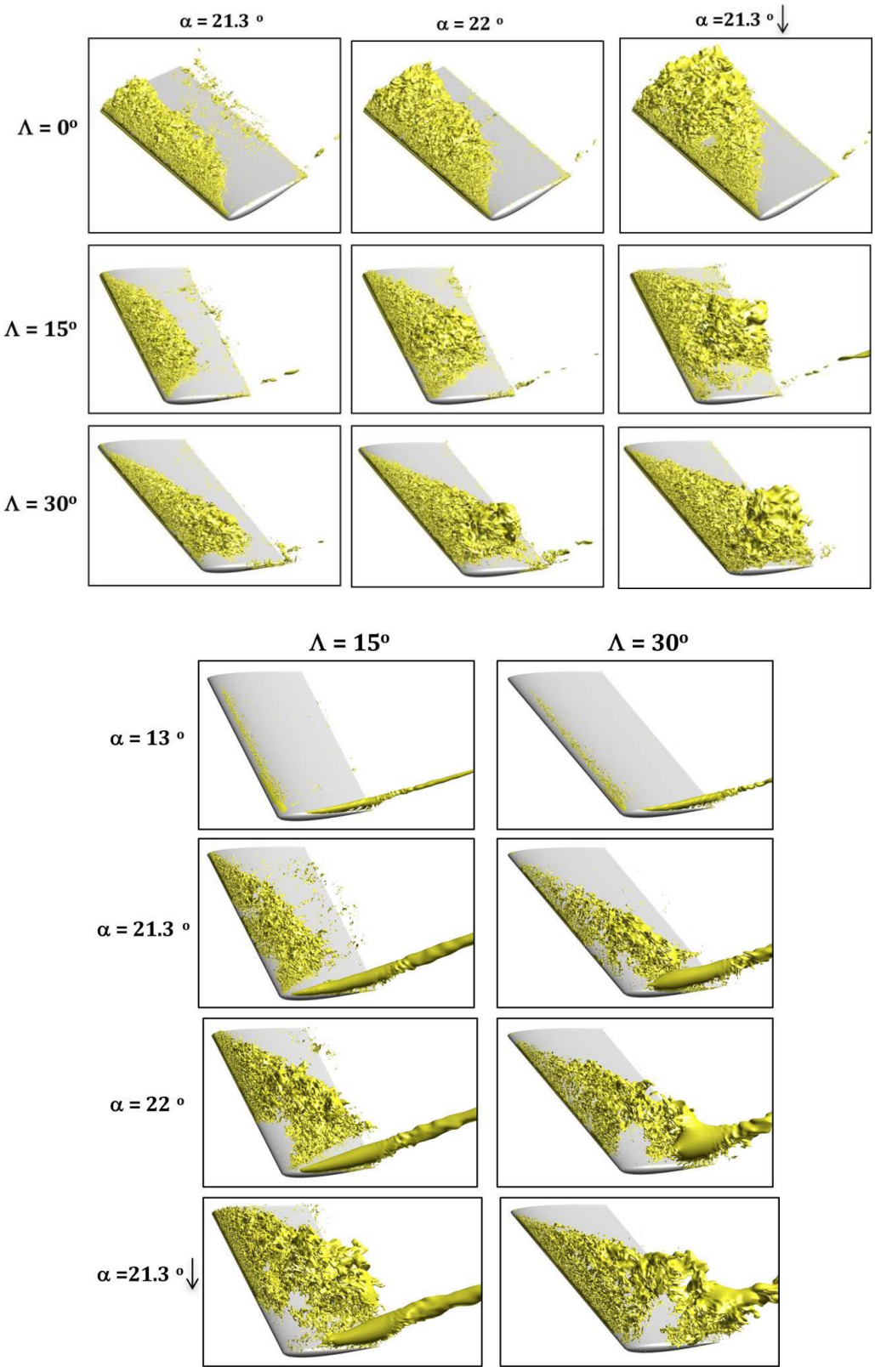

Figure 3. Streamwise (top) and spanwise (bottom) reversal near maximum angle of attack[8]

Figure 3 above shows the streamwise flow reversal for all three sweep angles near their stall angle. It can be seen that streamwise stall is mostly evenly distributed along the unswept airfoil and tends to move spanwise as sweep angle is increased. Flow reversal is more uniform and evenly distributed for the unswept case while becoming more aggressive in the spanwise direction.

Flow Structure and Ring/Arch Type Vortex Formation

Figure 4 below indicates that leading edge stall can be observed while pitching upwards past 21.3°. After the maximum pitching angle is achieved, the airfoil begins to pitch downward and the initial stages of arch vortex formation begins. The arch vortex remains dominantly near the surface of the airfoil, but proceeds to detach and form a ring type vortex near 16.4° while pitching downward. Subsequently, the ring vortex is shed into the freestream flow as the airfoil continues to pitch downward.

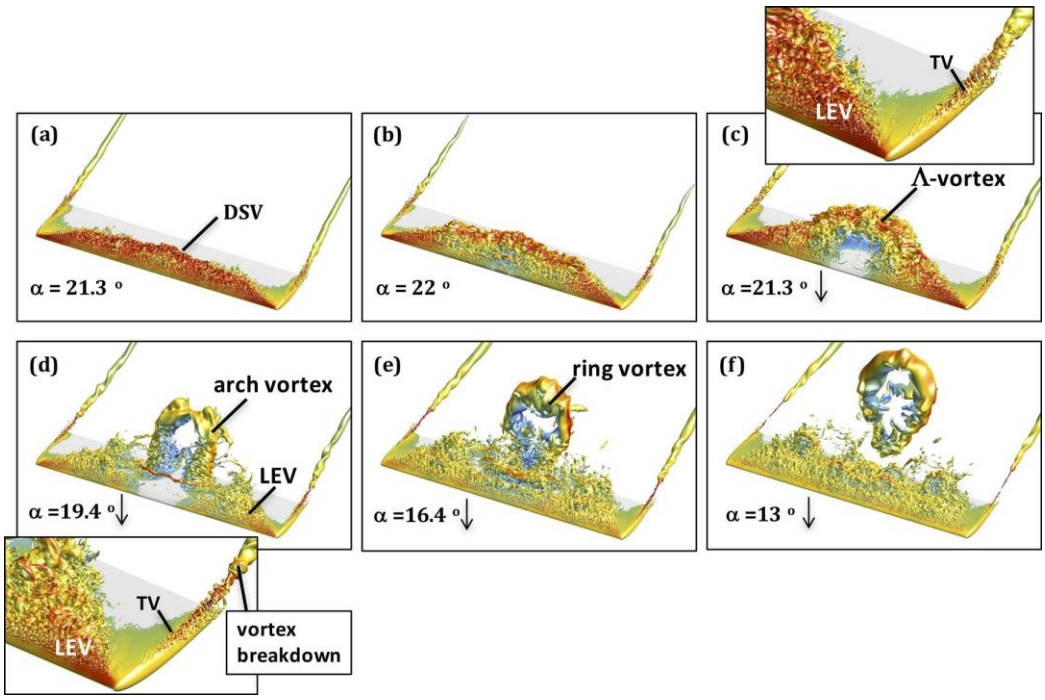

Figure 4. Three-dimensional flow structure during pitching cycle for Λ = 0° [8]

We see that trailing edge vortices are present for the extent of the pitching cycle, yet make no interaction with the arch or ring type vortex at any time during the cycle. Flow remains to be modernly uniform in between the two vortex formations. One of the major areas of investigation is the effect of sweep angle on the airfoils performance. More specifically in this context, its effect on stall characteristics. When the sweep angle is changed to 15° relative to the spanwise direction, the flow characteristics are subject to minor changes. Figure 5 below shows that the arch type vortices will also begin to develop when approaching its stall angle from an upwards pitching maneuver of 21.3°, however, with the case of a swept wing, the arch vortex begins to develop further along the wingspan closer to x/c = 0.5. When the airfoil reaches a downward stroke of about 18.8°, the arch vortices will shed to form a ring vortex.

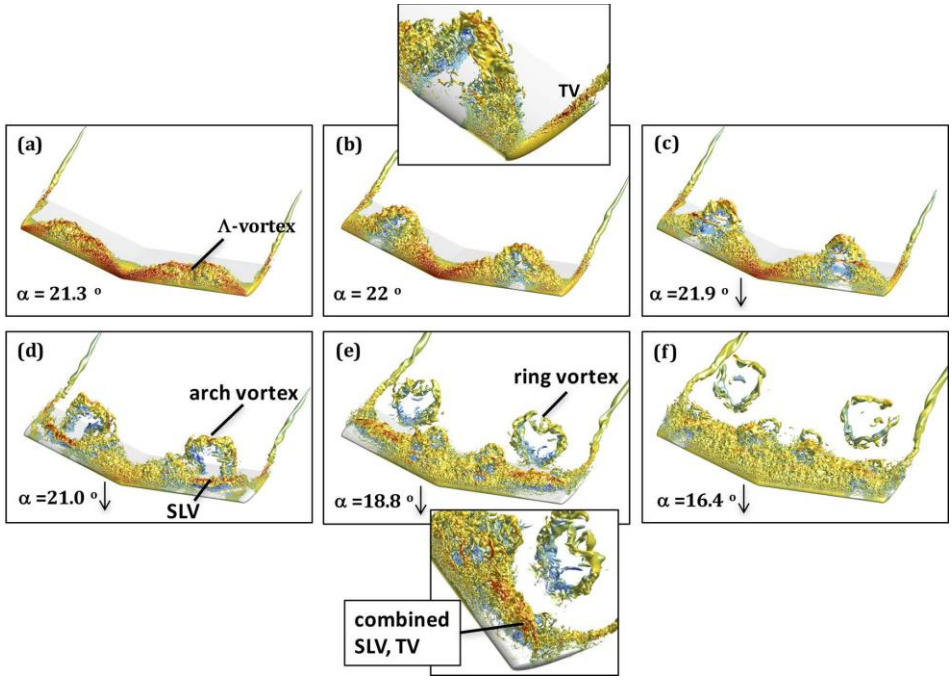

Figure 5. Three-dimensional flow structure during pitching cycle for Λ = 15° [8]

The same pattern of development for the Λ = 15° case as the unswept case, however, the ring vortex has shifted down the wingspan slightly. Because of this, there is expected to be a minor interaction with the wing tip vortices near downward pitching angles below 16.4°. It is unsure if

these ring vortices will carry an appreciable effect on lift while interacting with the wingtip vortices, but this will be explored further in subsequent sections.

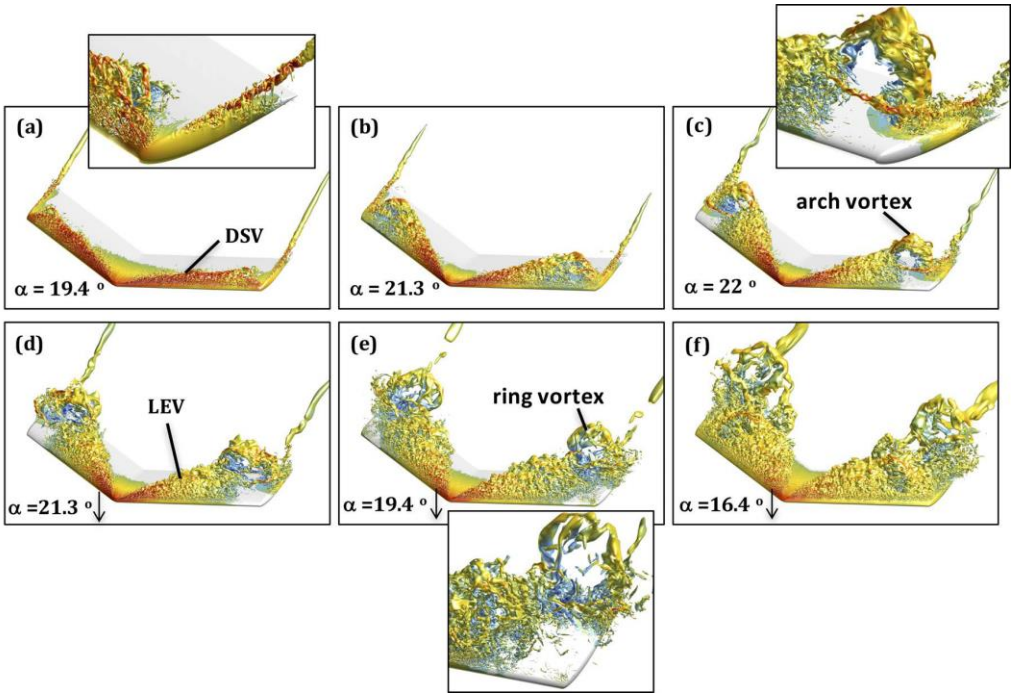

Figure 6. Three-dimensional flow structure during pitching cycle for $\Lambda = 27.6°$ [8]

Increasing the sweep angle further to $\Lambda = 27.6°$ produces arch vortices similar to the previous cases, however, the emergence of the vortices is delayed in the pitching motion. Rather than beginning pre-reversal approaching the stall angle, the vorticities begin to form and continue to move spanwise while the down stoke begins past $\alpha = 22°$. The arch vortices formed in this case remain attached to the surface of the airfoil before coming in contact with the wing tip vortices midway through the down stoke. A highly disordered flow can be observed during the interaction of these two vortices. The arch vortex is then shed at the bottom of the downstroke and the cycle begins once again. Figure 7 below shows a detailed sectional view of the flows vorticity at particular span sections. These sections of vorticity will be a particular area of interest during this evaluation.

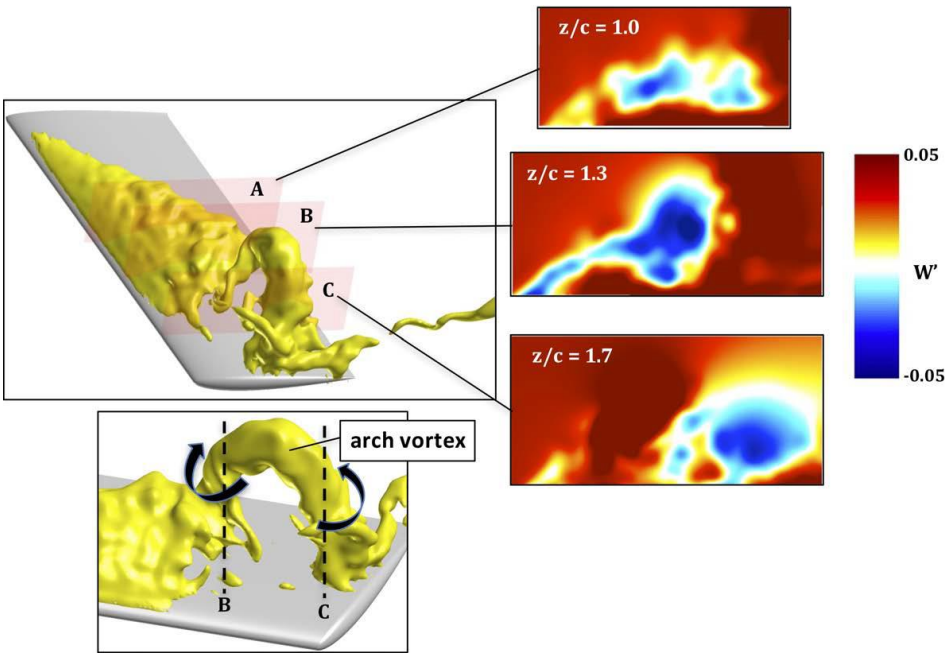

Figure 7. Arch vortex formation during down stroke [8]

Interestingly, the formation of this attached arch vortex may be beneficial in maintaining a slightly higher sectional lift when compared to the unswept case. Figure 8 below shows that the lift coefficient remains higher in the along the spanwise region while pitching upwards.

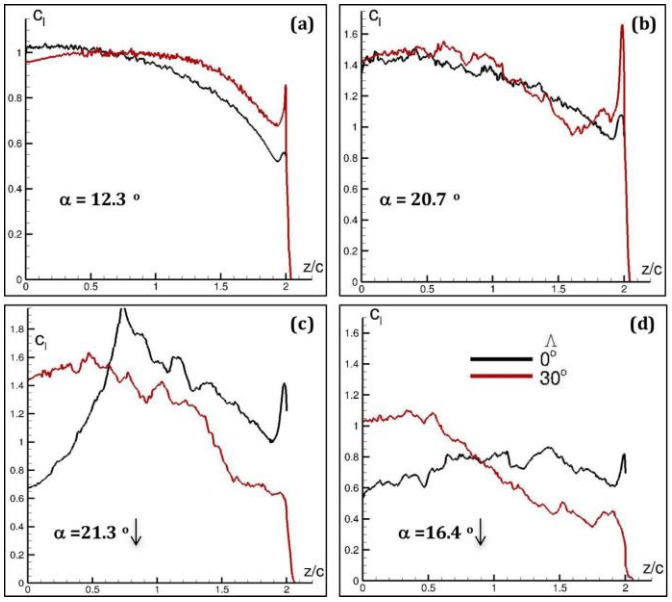

Figure 8. Sectional lift properties for Λ = 0° and 30° [8]

Conversely, while the swept wing may help increase sectional lift while pitching upwards, the previous figure suggests that sectional lift coefficient is significantly decreased throughout the remainder of the downstroke.

CHAPTER 4. EXPERIMENTAL SETUP

Experimental Overview

In order to simulated the sinusoidal pitching motion demonstrated in the computational results, an apparatus capable of actuating an airfoil sinusoidally was constructed. The actuator must be capable of actuating the airfoil between a minimum and maximum angle of attack and at a defined pitching frequency. Furthermore, the actuator must possess the ability to be adjusted for various ranges of pitching angles as well as modular to accept various shapes and sizes of airfoils. The constructed actuator must work alongside the wind tunnel where the airfoil will be subject to the prescribed flow conditions described in the aforementioned chapter. Data will be collected at various points along the wingspan using PIV which will then be evaluated against the computational results and relative pitching angle will be measured at the line of symmetry in the DaVis software.

Test Wing Geometry

Since three different sweep angles will be evaluated, three individual airfoils will need to be made. The airfoils will be 3D printed from ABS with two holes running with the pitch angle; one at 25% chord length and another 25 mm behind that. It's important to note that in order to ensure free stream boundary conditions at the, span of the airfoil has to be limited to half of the wind tunnel throat. This means the maximum span length of the airfoil will be approximately 152 mm or 6 inches. Both holes will be printed about the axis of symmetry. In order to reduce material consumption and mass, a medium infill of 50% will be used for the bulk of the airfoil. Figure 9 below contains a cross section of a test airfoil which was successfully printed with a sweep angle of 27.6°.

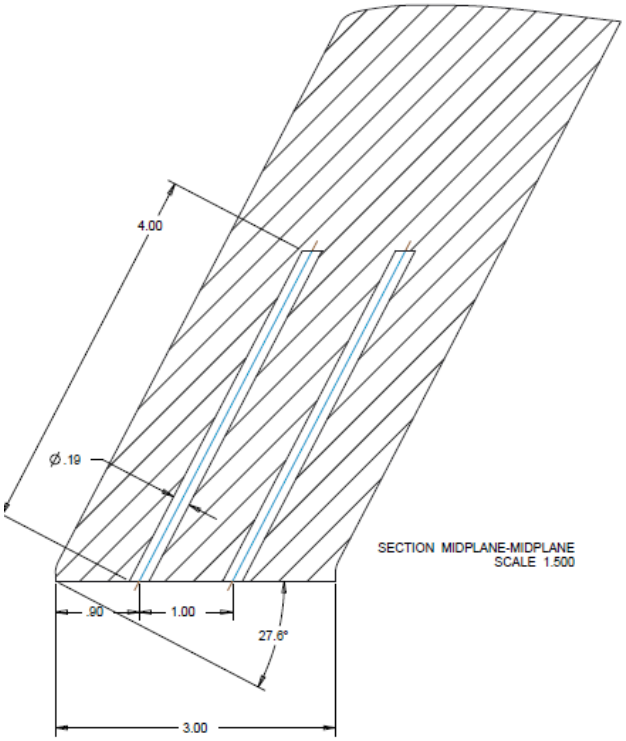

Figure 9. NACA0012 airfoil, $\Lambda = 27.6°$

The printed airfoils will be surmounted to a fixed column and allowed to rotate about its aerodynamic center as previously described. Inserted into the airfoils, will be two, 3.5 mm rods which will be used to support the entirety of the airfoil and permanently to the inside of the airfoil with an adhesive. The rods will be angled in accordance to the required sweep angle of the airfoil. The rods will protrude from the airfoil by 30 mm and will be used to surmount the airfoil to the actuating apparatus attached to the wind tunnel. Figure 10 shows a test section of the airfoil with the threaded rods inserted. As previously stated, the airfoil will be mounted and rotate about its quarter chord. The connecting rod behind the rod inserted at its quarter chord will be connected to the actuating arm displayed in the subsequent sections. Figure 11. shows the actual $\Lambda = 27.6°$ airfoil mounted in the throat of the wind tunnel.

Figure 10. Airfoil test print with supporting rods

Figure 11. $\Lambda = 27.6°$ airfoil mounted in the wind tunnel

Wind Tunnel

The data which will be collected for this investigation will be captured using equipment and methods currently used and practiced at NDSU. Any apparatus needed to actuate the airfoil will be constructed to replicate the rapid airfoil oscillation. NDSU is currently equipped with a FloTek 1440 wind tunnel which will be used to carry out these tests shown in Figure 12. The wind tunnel is capable of delivering a consistent free stream velocity of $U_\infty = 35$ m/s and the throat has

dimensions of 12” x 12”. This simple wind tunnel will be capable of recreating flow conditions in the computational experiments.

Figure 12. NDSU’s FloTek 1440 wind tunnel and workstation

Actuator Design

In order to actuate the airfoil at the desired frequency, a type of oscillator will need to be constructed. The entire actuating apparatus was constructed in the Dolve machine shop and made entirely from original parts. The entire unit was mounted to 80/20 aluminum rails rigidly mounted below the wind tunnel such that the whole fixture could be moved in any relative direction. The airfoil will be fixed to a column such that it can rotate freely along its center axis. The actuation rod behind the center axis will be attached to an actuating linear shaft. This shaft rides along a set of linear bearings to keep it on track. A counter weight and connecting arm was machined out of aluminum and arranged in a crankshaft formation in order to produce a sinusoidal action. Mounted at the center of the counterweight was a UL 12V DC motor capable of delivering up to 3000 RPM. The connecting arm is located 15 mm radially away from the center of rotation to produce a maximum stroke of 30 mm. The counterweight was made out of stock aluminum and intended to possess a high moment of inertia in order to maintain stability at high frequencies. To achieve greater dynamic balance, half of the counter weight was machined off on one side to counter act

the moment applied by weight of the rod and any loads induced by the airfoil. The entire fixture is surmounted to a thick piece of aluminum which will be connected to a platform adjacent to the wall of the wind tunnel.

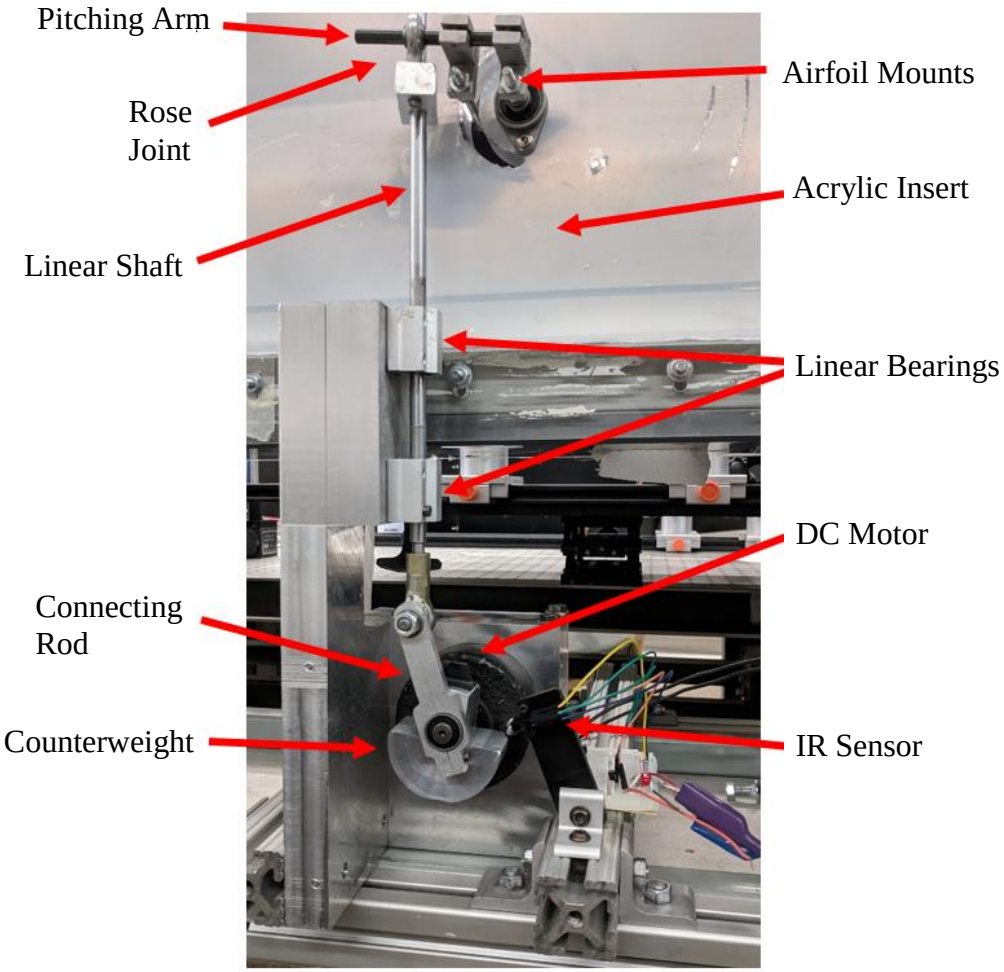

Figure 13. Entire actuator assembly

Fixed to the end of the linear shaft was a rose joint which traveled freely on another shaft called the pitching arm. The pitching arm was connected to the rods which were inserted into the airfoil and protruded through the acrylic insert. Though the model does deliver above the necessary parameters, it still produces a considerable amount of transverse vibration due to the unbalanced dynamic load. Future considerations can be implemented in order to eliminate unwanted interference from the apparatus while in operation as a more balance counter weight,

lighter push rod, and a more robust connecting solution to fix it to the pivoted airfoil. The counterweight, connecting rod, pitching arm connector, and rigid base of the actuator were all machined by hand and all other components were either pulled from other scrap equipment. The linear bearings and shaft were some of the few parts which were purchased new for this current design. Figure 14 shows the actuator pitching at a few select angles.

Figure 14. Testing the maximum range of motion of the actuator

Particle Image Velocimetry

In order to compare preexisting computational results previously mentioned, flow will be captured using a combination of Particle Image Velocimetry and Pressure Sensitive paint, which will be described in detail in this section. Fundamentally, PIV will capture two instances of flow, one after another, separated by a few microseconds and cross-correlation can be used to determine the displacement of each particle in the flow. Once displacement and time are known for each particle, velocity of the said particle can be determined. Figure 15 shows a brief example of the two frames and the two frame cross-correlation. It is intended to capture velocity fields around

the top and bottom surfaces of the airfoil at several predetermined locations. Data captured from the flow field will be collected from several points of interest and compared to computational data.

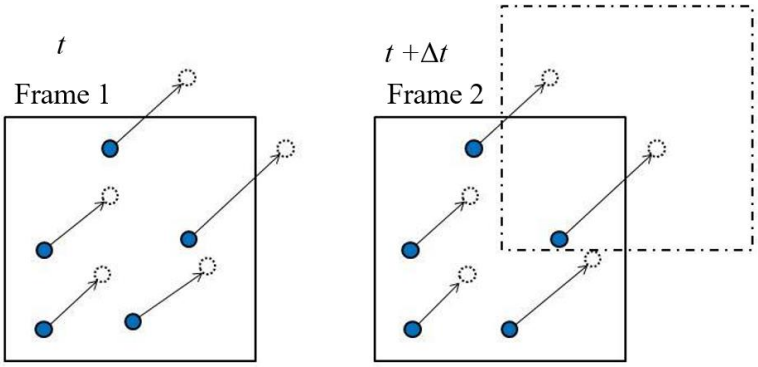

Figure 15. Two frame cross-correlation[9]

It's important to note that since this is an oscillating system, but our point of interest is at a specified angle of attack, the PIV will need to be synchronized in order to capture data at the desired point. A feedback system will be incorporated to the actuator in order to consistently capture data at a desired moment of actuation and is discussed in the subsequent section.

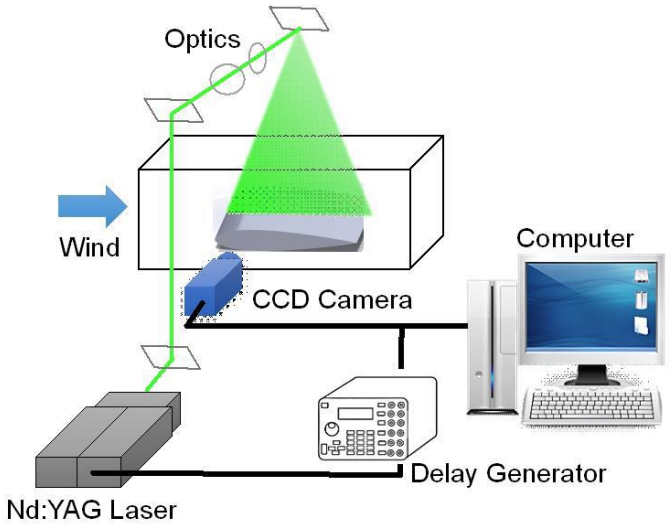

Figure 16. Basic PIV arrangement [11]

The fundamental setup of the PIV system can be seen in Figure 16 above. The airfoil will be placed in the middle of the test section of the wind tunnel. Illumination will be provided by a

double-pulsed Nd:YAG laser (NewWave MiniLase-III) emitting two laser pulses of 100 mJ at a wavelength of 532 nm with a repetition rate of 15 Hz. The laser beam can then be shaped to a laser sheet (thickness <1 mm) by using a set of mirrors, spherical and cylindrical lenses. The flow will then be seeded with atomized DEHS oil droplets to achieve particle sizes less than 1μm. Two La Vision IMAGER LX 2M cameras with a resolution of 1608 x 1208 and interframe capability of 200 ns will be set up with its axis perpendicular to the laser sheet for image acquisition. For the desired flow speed, the time between images taken was set to $\Delta t = 25\mu s$. The cameras and the Nd:YAG lasers were connected to a workstation and controlled with ISSI PSG-2 Pulse Generator and secondary delay generator which controls the timing of the laser illumination and the image acquisition. LaVision DaVis 8.1 software was used for control of the parameters of the imaging and controlled by an external trigger. Figure 17 below shows an image captured during testing while the laser is firing. The airfoil being tested and seeded particles can be seen in the center of the wind tunnel section.

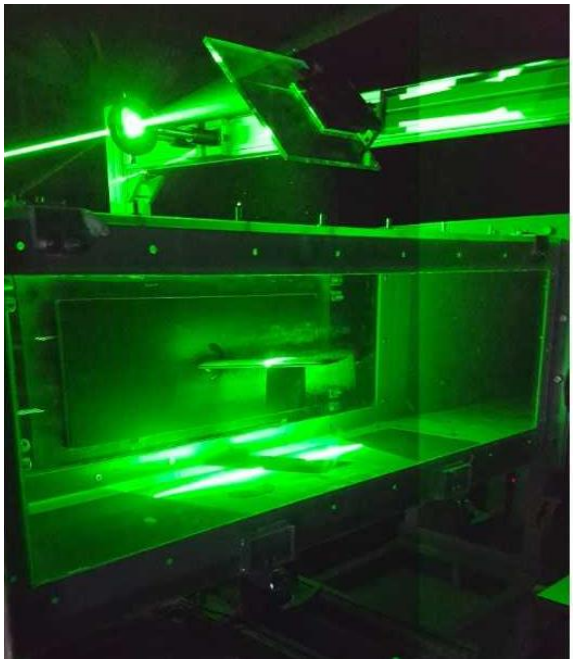

Figure 17. Laser firing during a test

Synchronous Triggering Method

In order to capture data at specific pitching angles at any point during the pitching cycle, a method was created to synchronize the actuator to the lasers and camera. A basic circuit was made using an inferred sensor and a transistor which would be the source of the external trigger. A small piece of tape would pass between the beam of the inferred sensor which would close the gate to a 2222N transistor and create a pulse. This output pulse could be measured easily with an oscilloscope to obtain frequency of rotation. Figure 18 below shows the basic function of the rudimentary trigger circuit.

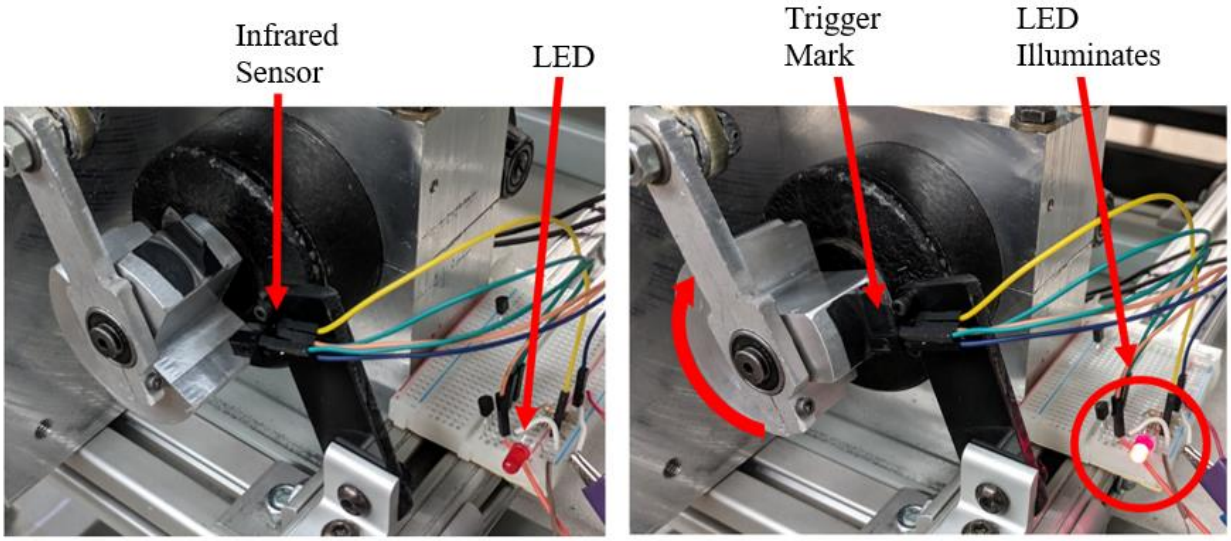

Figure 18. Rotating counterweight

Since the period of rotation is the same for the rotating crank as it is with the pitching cycle, the delay necessary to offset the laser can easily be calculated. The DaVis 8.1 Software used to capture data with PIV can accept an external signal to trigger the cameras to capture data. The same pulse delay generator was used to control all of the cameras and lasers shown previously in Figure 16, but instead of the pulse signal being generated by the ISSI PSG-2 software, and external trigger was used. Figure 19 shows the connection between the external trigger circuit and the output to the delay generator.

Figure 19. ISSI PSG-2 pulse generator with external trigger input

The output of the external trigger will be a square wave and the frequency can be measured by an oscilloscope. Figure 20 below shows an example of the external trigger (yellow) and the signal sent to the laser (green). The frequency of both signals can be seen outlined at the bottom.

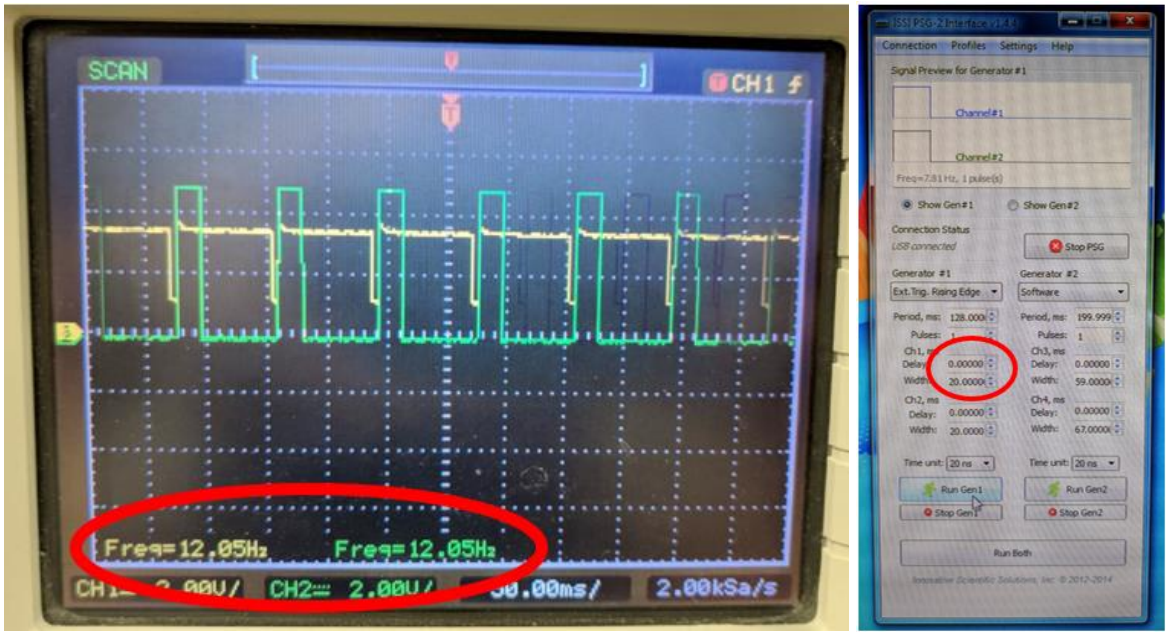

Figure 20. External trigger source (yellow), laser signal pulse (green), and the ISSI trigger delay (right)

For this event, the laser is firing at a delay of 0.000 ms offset by the external trigger on its falling edge. Intrinsically, when there is no delay on the trigger, the laser will fire when the air

foil is at 16º pitching up. Knowing the frequency of actuation, the time delay can be calculated from the period and the desired angle of attack. An example of all the time delays necessary to fire at specific pitching angles can be seen in Appendix A.1.

CHAPTER 5. RESULTS AND DISCUSSION

It was observed that all three airfoils with the three different sweep angles stalled at decreasing pitching angles as well as in relation to the sweep angle. The unswept airfoil was able to achieve the highest pitching angle before complete stall while also possessing the smallest laminar separation bubble while pitching upwards. Interestingly, after the airfoil had achieved its maximum pitching angle and started to pitch downward, the laminar separation bubble would collapse and flow would reattach to the top surface near the leading edge earlier than expected. Three frames between the critical angles of 19º↑ and 12º↓ were selected for discussion. Additional pitching angles between these ranges for all three sweep angles can be found in Appendix B for qualitative observation. The following results consist of actual instances of flows at specific pitching angles right before, during, and after stall. The leading edge is shown to the left and the trialing edge is to the right. The velocity gradient of each flow instance is shown below each figure. Overlaid the velocity gradient, the streamlines show the direction and pattern of flow over the surface as well as reveals instances of flow rotation and vorticity.

Flow Structure Over Pitching Unswept Wing, $\Lambda=0^{o}$

The unswept case provided some of the most consistent and expected results to that of the CFD analysis and rudimentary theory correlating with previous data. Under the dynamic motion, the airfoil began to show a high degree of flow reversal at approximately 18º referenced to free stream flow. Figures 21-23 below show the formation of the separation region and its stall and then sequence of reattachment while pitching upwards, reaching is maximum angle, and then pitching down. The unswept wing was shown to have the highest stall angle over the other two swept airfoils.

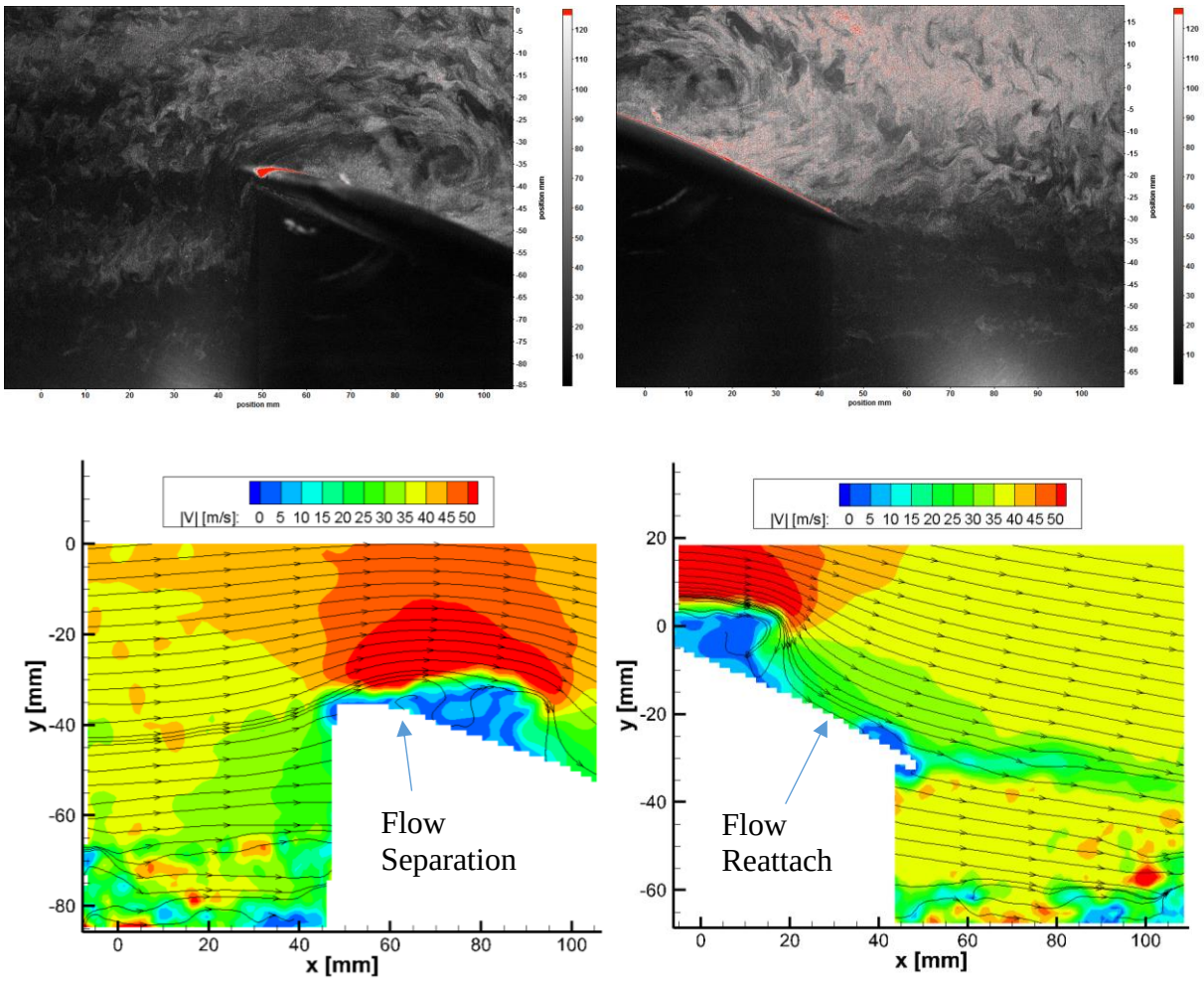

Figure 21. Leading (left) and trailing (right) edge flow structure at α = 21.1°↑, x/c = 0.4 (174)

Stall was observed by the total separation of flow over the top surface of the wing while pitching upwards followed by chaotic, turbulent flow from the leading edge and into the freestream behind it. While undergoing dynamic motion, the unswept airfoil would begin to stall at approximately 21.1° relative to the free stream flow. The laminar separation bubble for the unswept case was spanned about half of the entire chord length prior to complete stall. When the airfoil began pitching downward, flow would begin to reattach to the leading edge and the laminar separation bubble would shed off the trailing edge and flow continued to reattach at the leading edge. Flow reversal leading to stall can be observed to begin at approximately 21.1°↑ and subsequently reattach at the leading edge at about 16.4°↓.

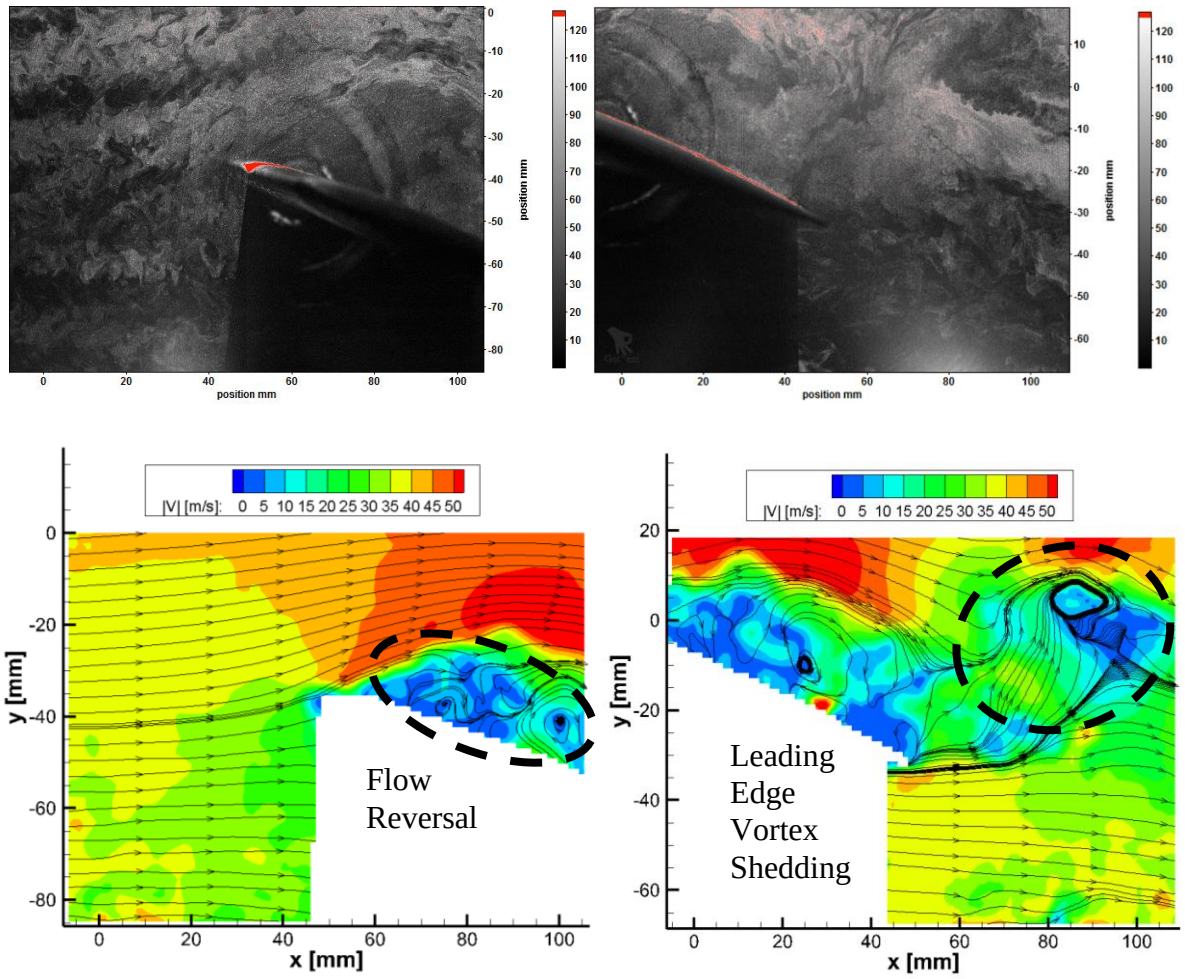

Figure 22. Leading (left) and trailing (right) edge flow structure at α = 21.2°↓, x/c = 0.4 (186)

Following the formation of the laminar separation bubble and the shedding flow reversal, it can be seen in Figure 23 that larger eddies are shed from the surface of the airfoil when returning to the freestream. During the upstroke, flow continued over the top surface as normal over the laminar separation bubble, but begins to collapse as the airfoil begins to pitch down and the laminar separation bubble is shed as flow reattaches to the top surface. There was little indication that there was any formation of arch or ring vortex formation above and behind the airfoil. Data along the 0.4 chord length suggests some early, turbulent formation of arch vortices, however, the presence of the arch vortex formation is not immediately apparent.

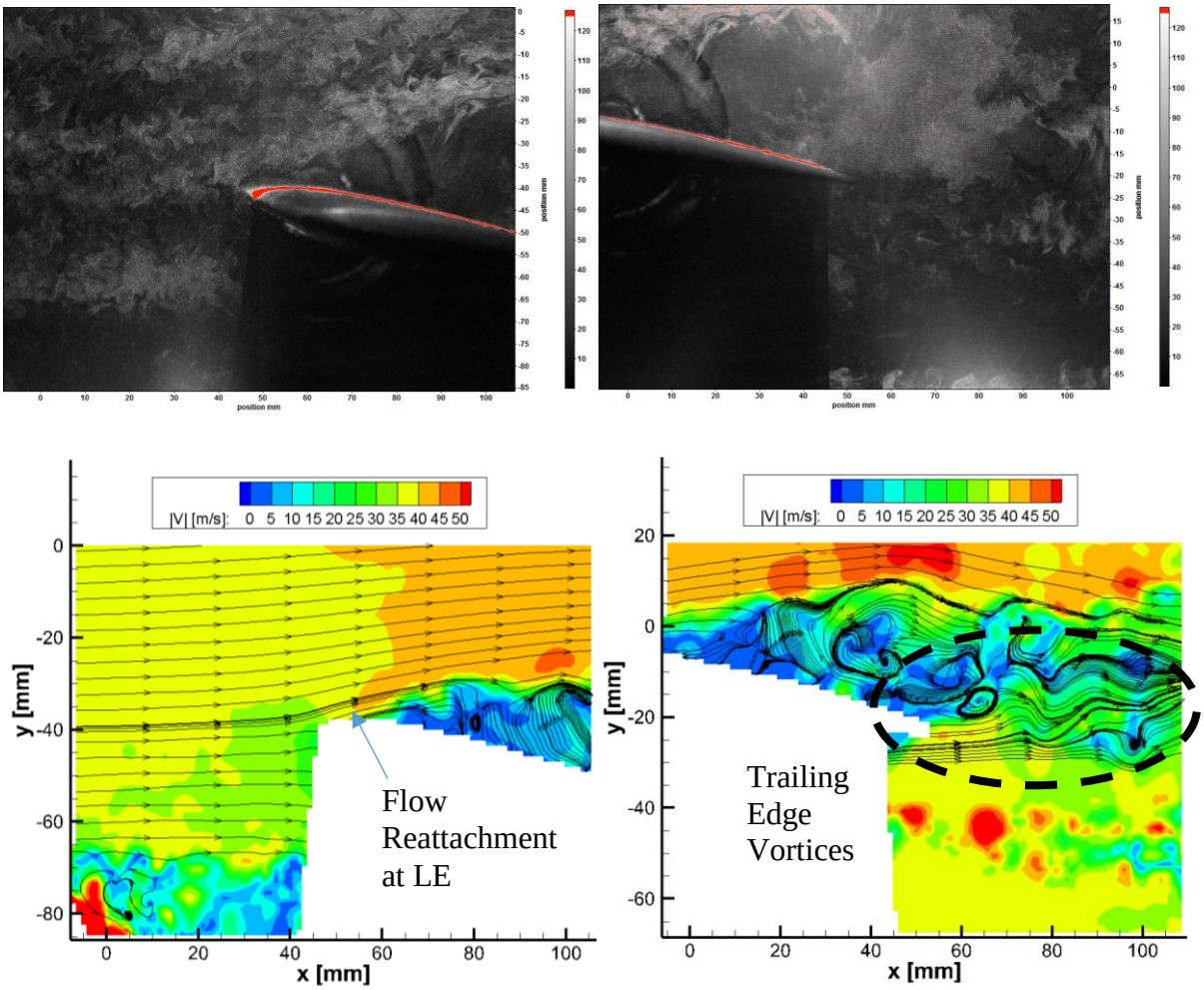

Figure 23. Leading (left) and trailing (right) edge flow structure at $\alpha = 14.4^{o}\downarrow$, x/c = 0.4 (328)

The unswept airfoil with its rounded tip showed typical wing tip vortex generation at most pitching angles. Figures 23 show vortices being shed from the trailing edge during the pitching motion. Interestingly, the trailing edge vortices that were formed while pitching downward were much more prominent than those formed during the upwards pitching motion. It is possible that this is due to the strong flow reversal shedding off the leading edge and upper surface during this upward motion which seeds these smaller wing tip vortices.

Flow Structure Over Pitching Swept Wing, Λ=15º

It can be seen in Figures 24-26, for comparable pitching angles, that flow remains attached for a longer duration during the pitching cycle than the unswept case. Figure 24 does suggest some leading edge reversal, but due to background noise and surface reflection, it cannot be stated for sure. It was noticed that much more defined flow reversal started much later in the pitching cycle above 20º↑. Interestingly, flow reversal at the top surface seemed to increase as the airfoil began to pitch downwards in Figure 25. Flow reattachment at the leading edge while pitching downward was not observed until closer to 14 º↓.

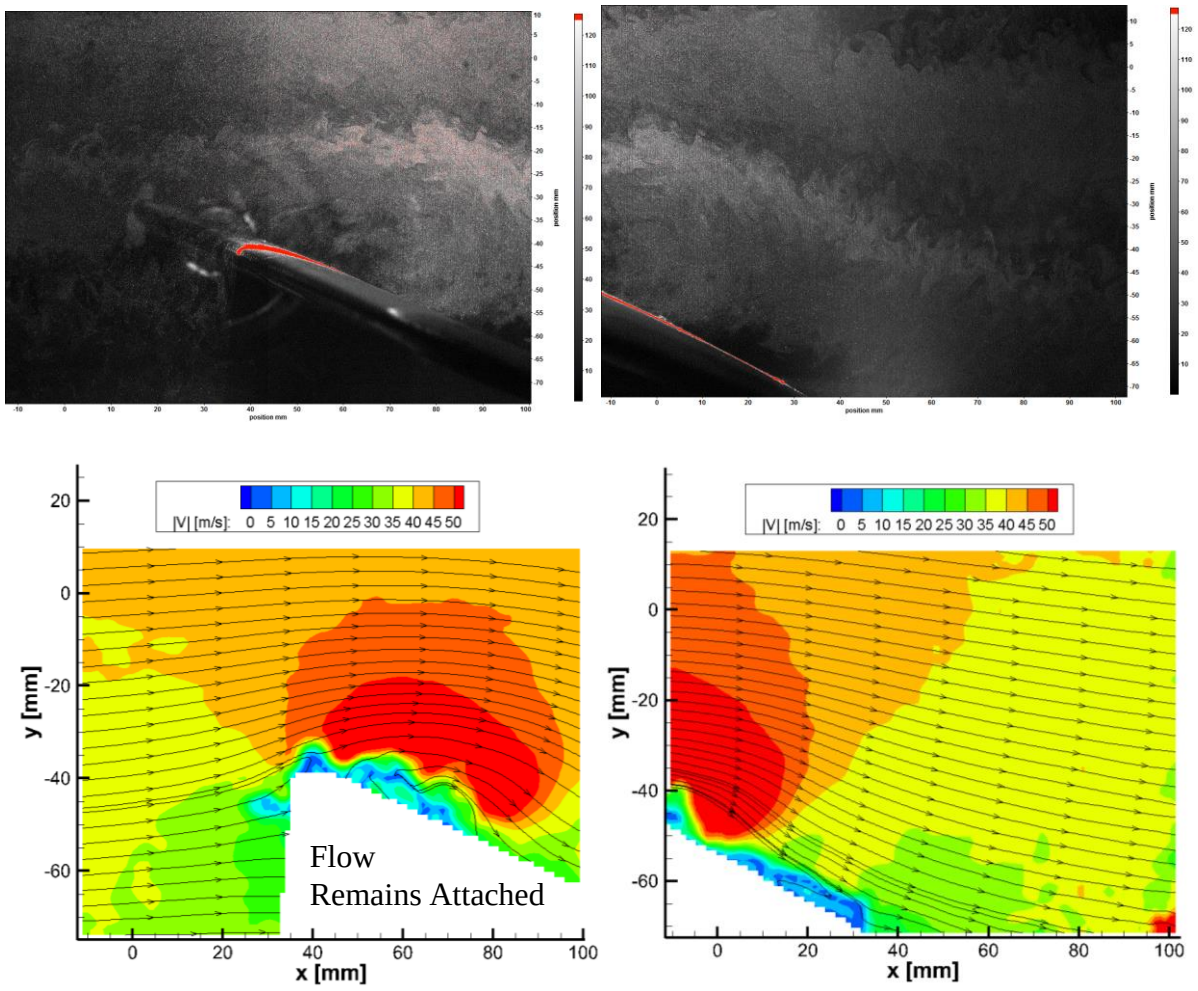

Figure 24. Leading (left) and trailing (right) edge flow structure at α = 22.1º↑, x/c = 0.4 (424)

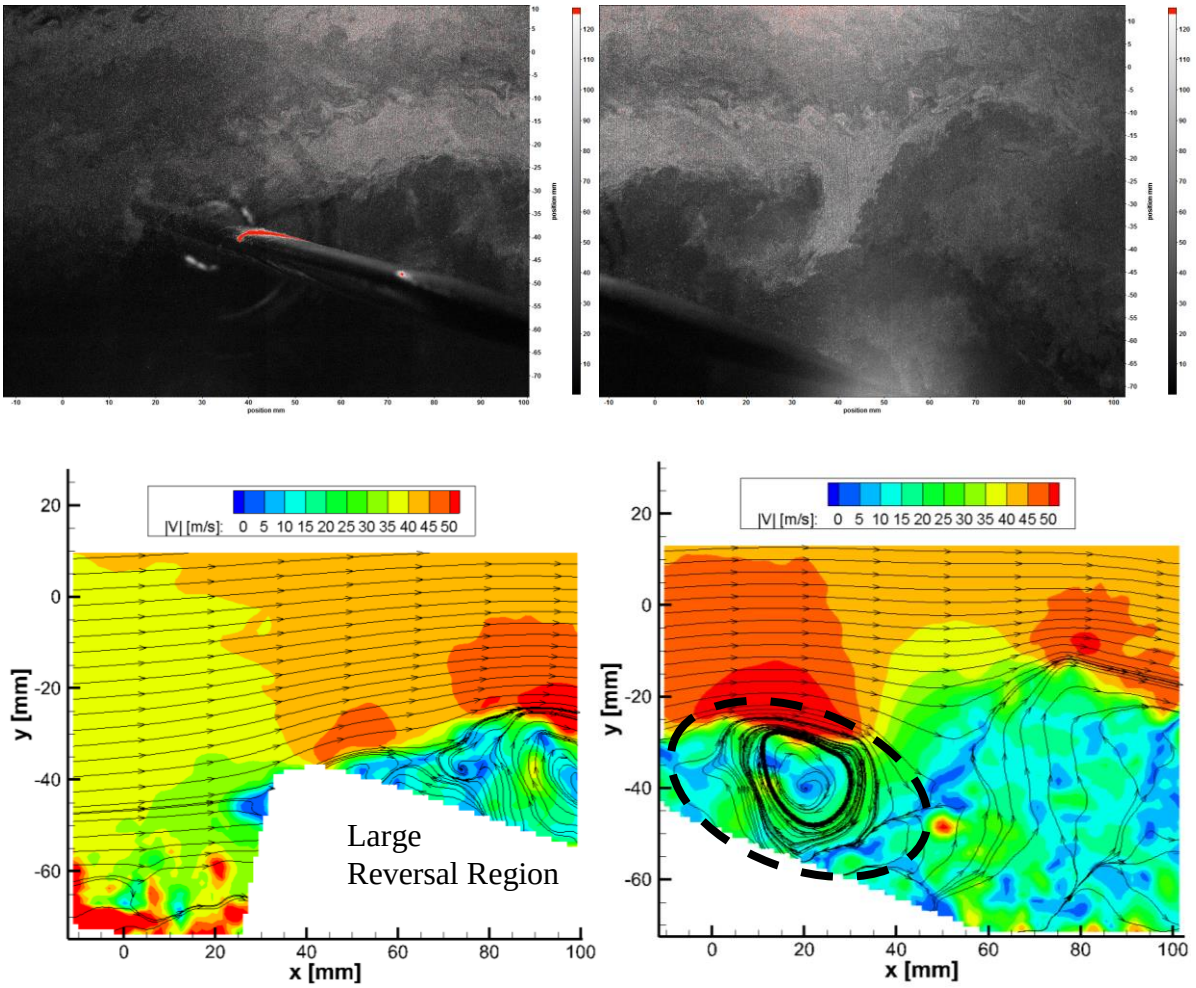

Figure 25. Leading (left) and trailing (right) edge flow structure at α = 19.5º↓, x/c = 0.4 (425)

It is possible that this is due to the larger reversed region which travels back to free stream before flow is allowed to reattach. Flow over the laminar separation bubble is comparable to the unswept case in the sense that flow continues over the reversed region, however the wake following the reversed region for the swept case is much greater than the unswept. Furthermore, Figure 26 show that the shed turbulent region over the remainder of the separation region possesses a larger magnitude of rotation when compared to the unswept case during the down stroke. Interestingly, the leading edge reattachment seems to be prolonged to further in the pitching cycle for the swept airfoil than the unswept case.

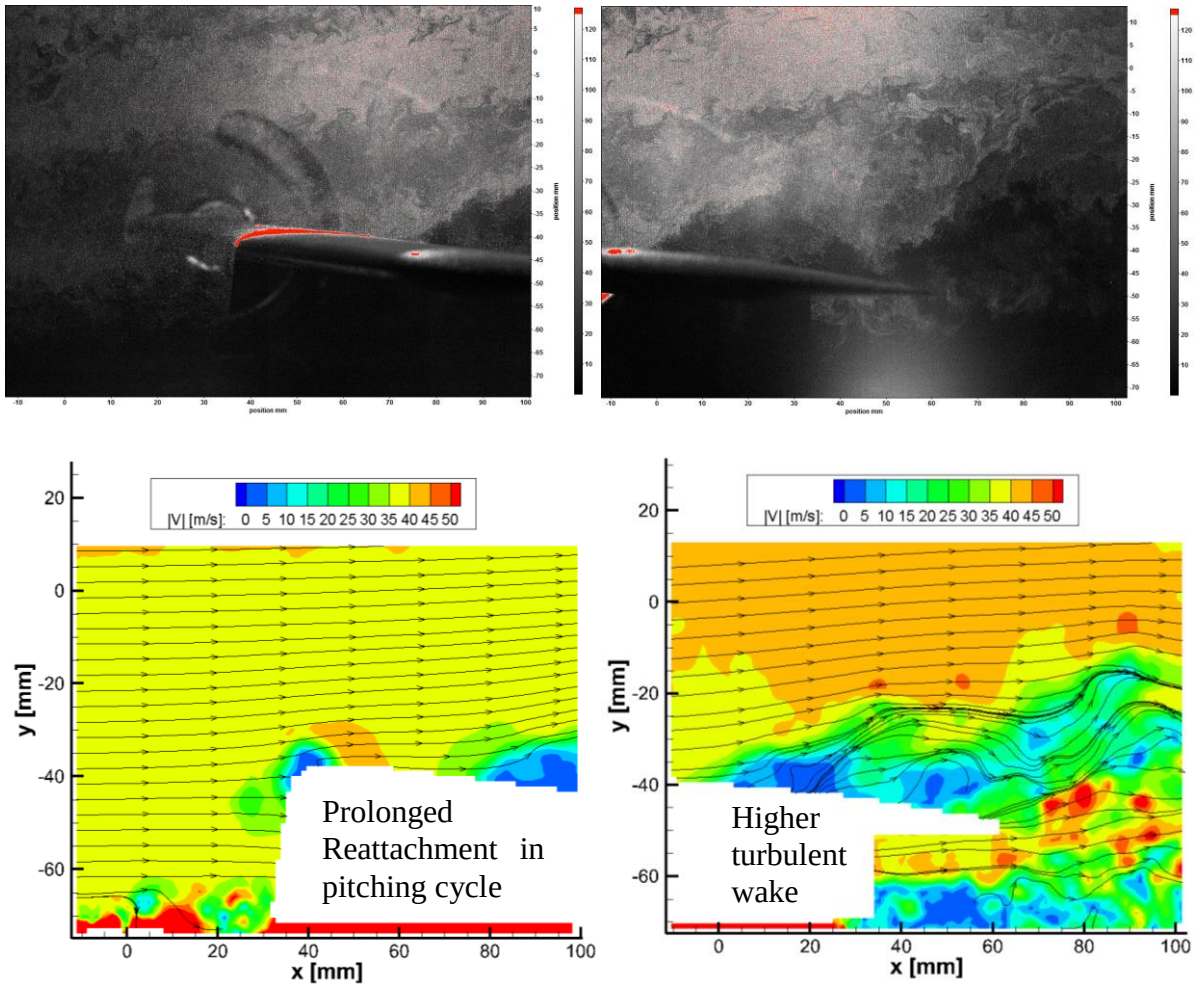

Figure 26. Leading (left) and trailing (right) edge flow structure at α = 12.8º↓, x/c = 0.4 (426)

Flow Structure Over Pitching Swept Wing, Λ=27.6º

It was observed that noticeable flow reversal was prolonged further than the previous swept case to beyond 22º↑. Flow reversal in Figure 27 is not entirely evident at these higher angles pitching upward, like the previous cases. This continues to suggest that flow may have the ability to remain attached at higher pitching angles as sweep angle is increased during a dynamic pitching cycle.

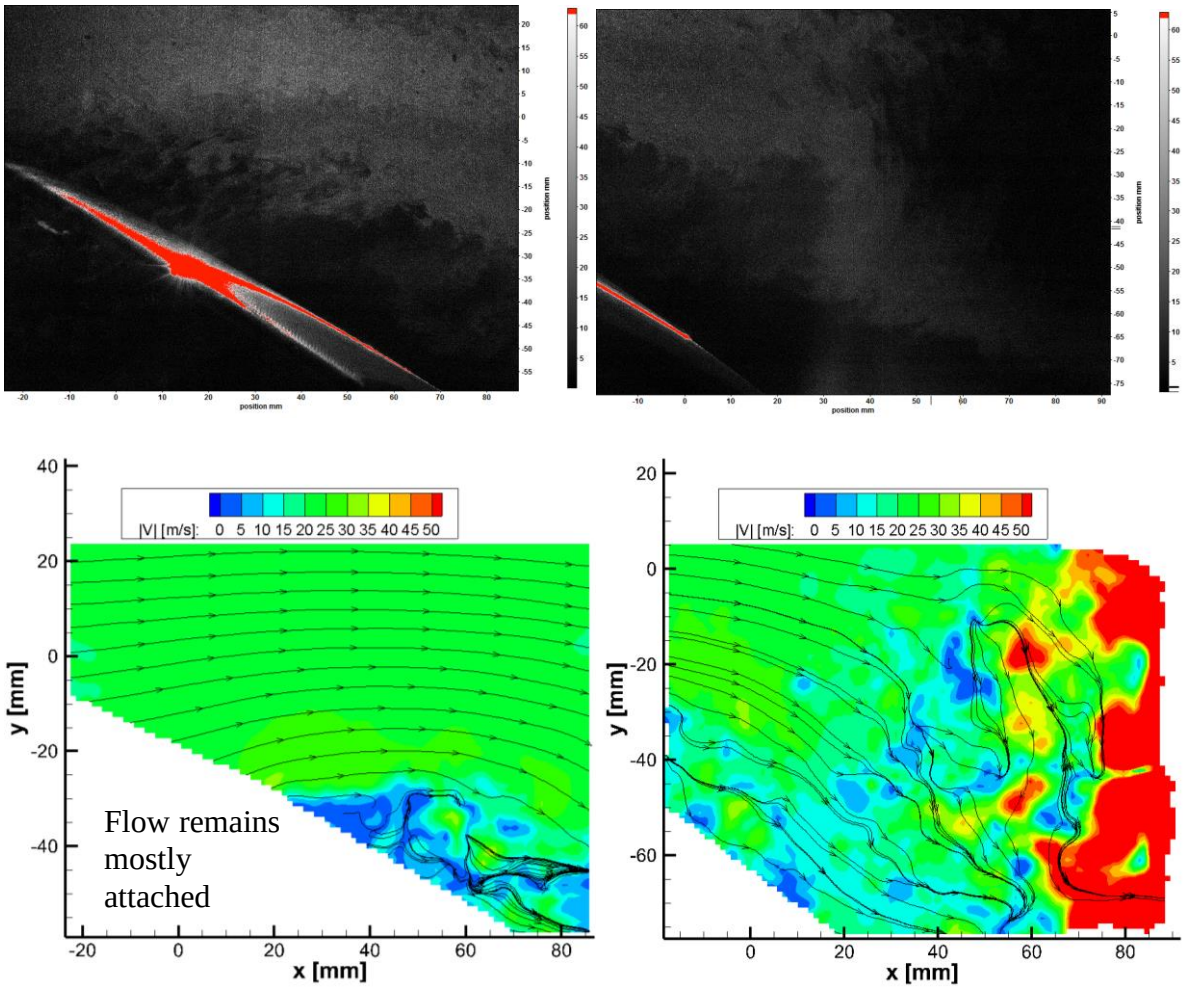

Figure 27. Leading (left) and trailing (right) edge flow structure at α = 22.5º↑, x/c = 0.6 (372)

While pitching downward in Figure 28, it was noticed that the forming reversal region was large enough to the point where a laminar separation bubble was not formed and sustained passed its maximum pitching angle and then reformed as the airfoil pitched down and reattached to the top surface. As the pitching angle increased, approaching stall, the reversal region became smaller and the flow was maintained to a closer proximity to the trailing edge. As the airfoil began to pitch down, the reversal region enabled the airfoil to reattach at the leading edge noticeably earlier than the lower swept angles. This particular behavior may indicate that higher degrees of sweep angle may benefit flow reattachment proceeding wing stall during a pitching maneuver.

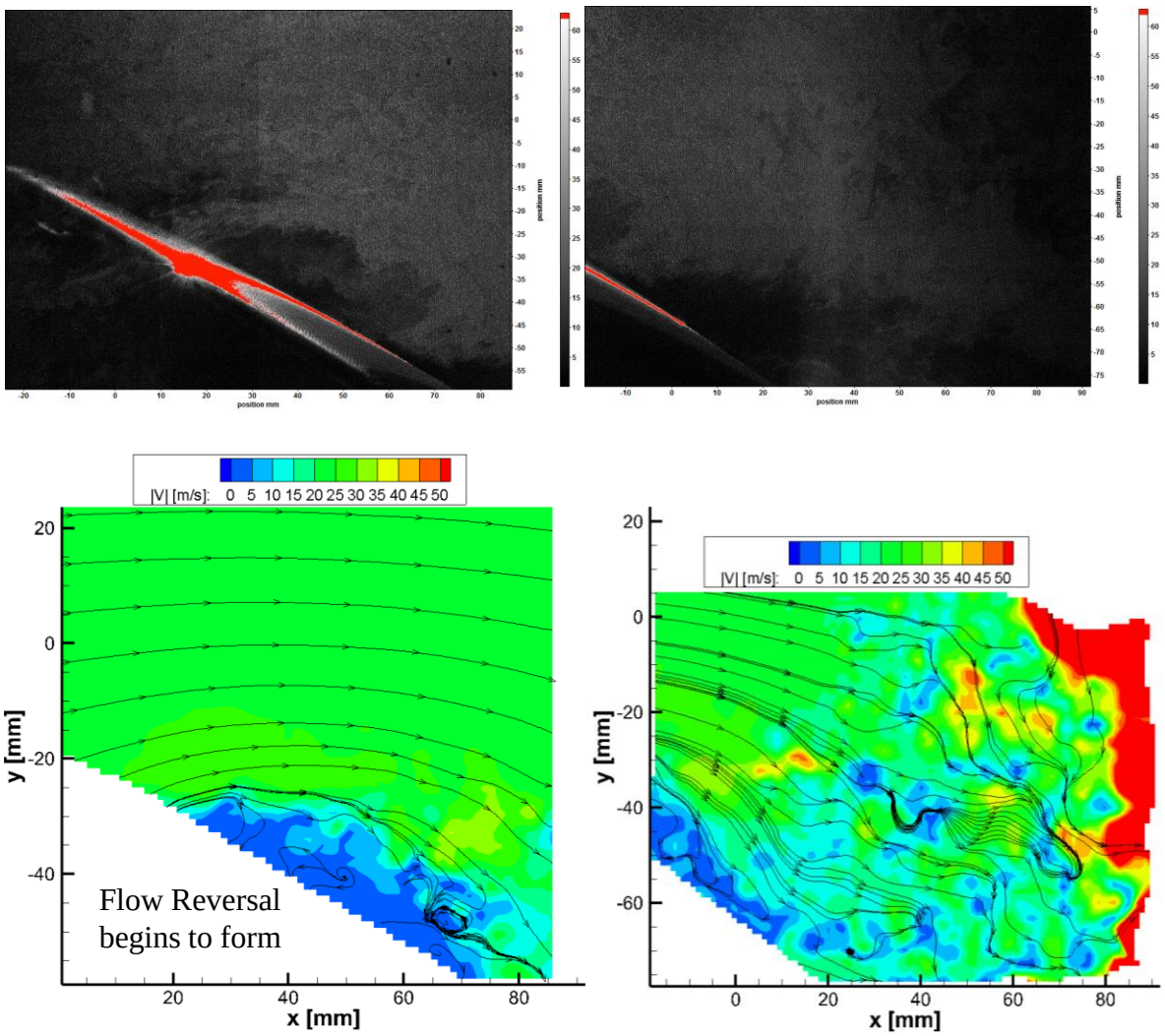

Figure 28. Leading (left) and trailing (right) edge flow structure at α = 22.0º↓, x/c = 0.6 (349)

This is also suggested in the previous section, the airfoil described that the large amount of flow reversal may reduce prolonged flow attachment. At lower, increasing pitching angles, the reversal region was significantly larger than the unswept case. Because of this, further analysis for the presence of vortex formation is explored for this case in the following section. Flow at the wing tip remained mostly turbulent and unattached for this specific swept case. It was expected that strong wing tip vortices would be observed proceeding the leading edge, however, only minor vortices were observed to shed from the wing tip during all pitching angles.

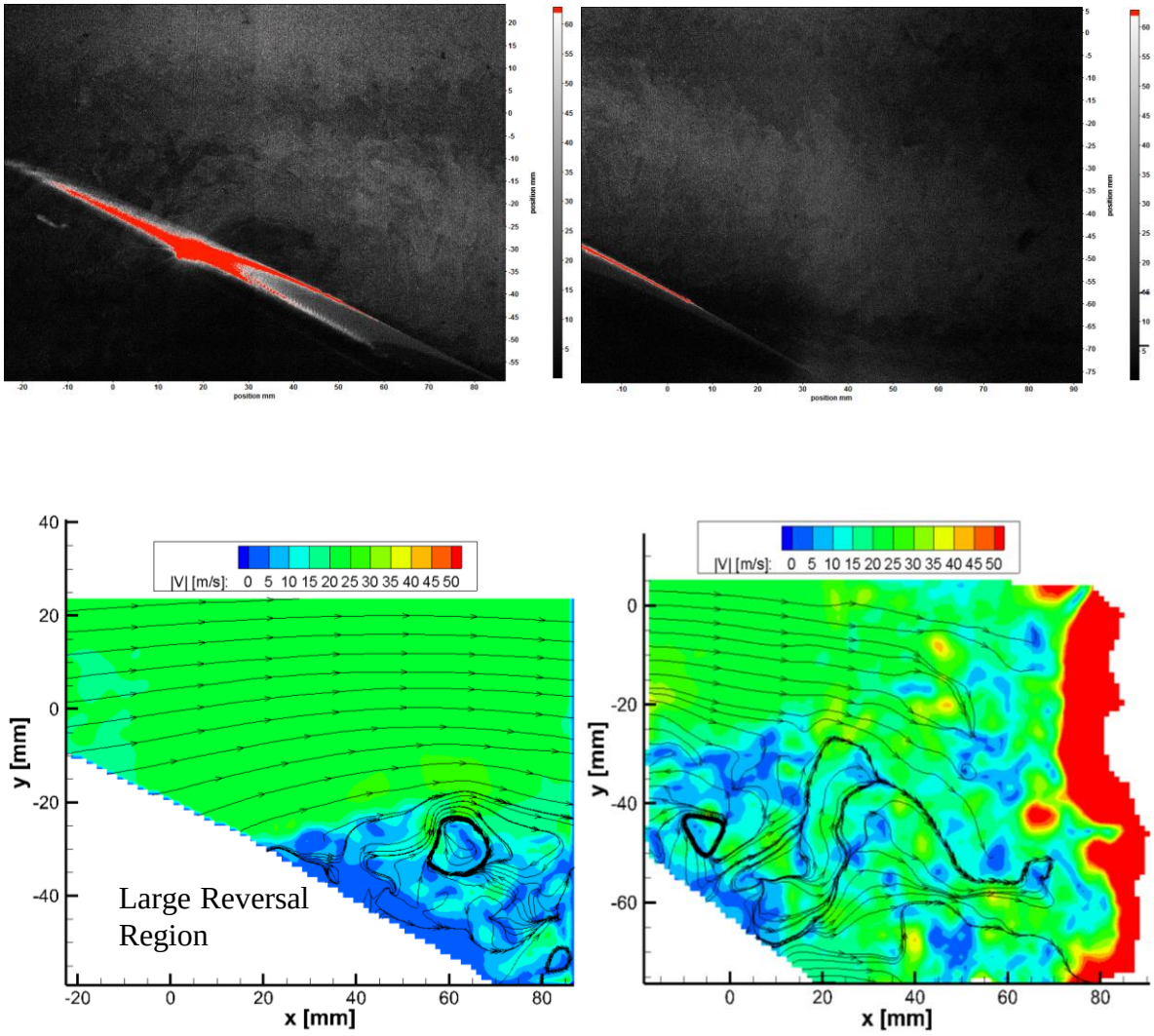

Figure 29. Leading (left) and trailing (right) edge flow structure at $\alpha = 21.1^{o}\downarrow$, x/c = 0.6 (370)

Though the presence of wing tip vortices should not be completely dismissed, they can still be seen at high pitching angles much like previous cases. In other flow instances, near the wing tip, the vortices shed off the tip mixed strongly with the attached flow reversal region and flow shed off the surface. Furthermore, further investigation should be conducted to verify wing tip vortices. For some instances, the wing tip had left the frame and substantial wing tip behavior was unable to be observed for this specific case. Nonetheless, wing tip behavior is only a secondary observation in this investigation. The particular flow behavior indicated by the preliminary CFD

suggests that the formation of these arch vortices may assist in flow reattachment. Although the presence of these arch vortices specifically are not clear for the unswept and 15º swept case with two dimensional PIV, the 27.6° swept case did have additional, rotational flow above and behind the top surface. Figure 30 show a strong presence of vorticity similar to that of the CFD results. Much like the observations in the previous two cases, further tomographic PIV will need to be conducted in further research to verify the validity of this speculation.

Arch and Ring Vortex Formation

A peculiar property from the computational results suggests the presence of the evolution of attached then detached vortices forming at the top surface of the wing which increases in magnitude as the sweep angle is increase. There was a distinctly heavier presence of detached flow vortices seen for the case with the highest sweep angle. Further data was taken at additional wing spans in order to verify this phenomenon. The previous CFD results discussed earlier suggest that arch/ring vortices may form above the swept airfoils distinctly above the surface near the trailing edge and shown again in Figure 30.

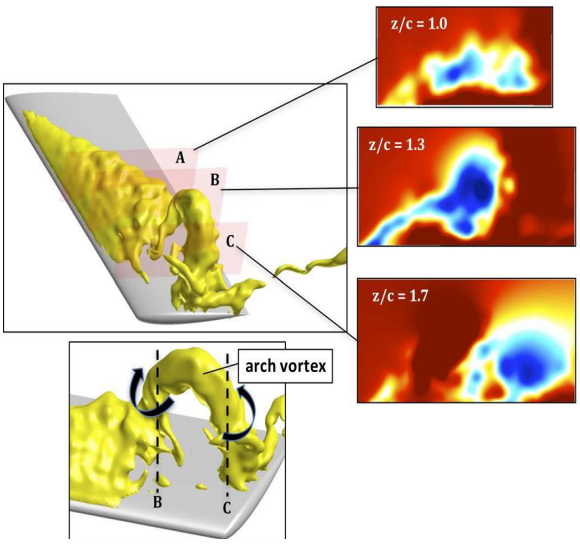

Figure 30. Arch vortex formation on the 27.6º swept wing [8]

Observing Figure 29 above, a strong area of rotation other than the anticipated attached flow reversal, can be observed above the surface of the wing at about 0.8 of the chord length. The separation region can be identified by the turbulent region closer to the surface below where the strong areas of flow reversal begin. The leading and trailing edge overlap affirm one another on this distinct region of flow. What separates this vortex formation from the attached flow region is that the reversal region will reattach to the trailing edge of the wing. The vortex separated from this region results in a turbulent, chaotic flow following its formation.

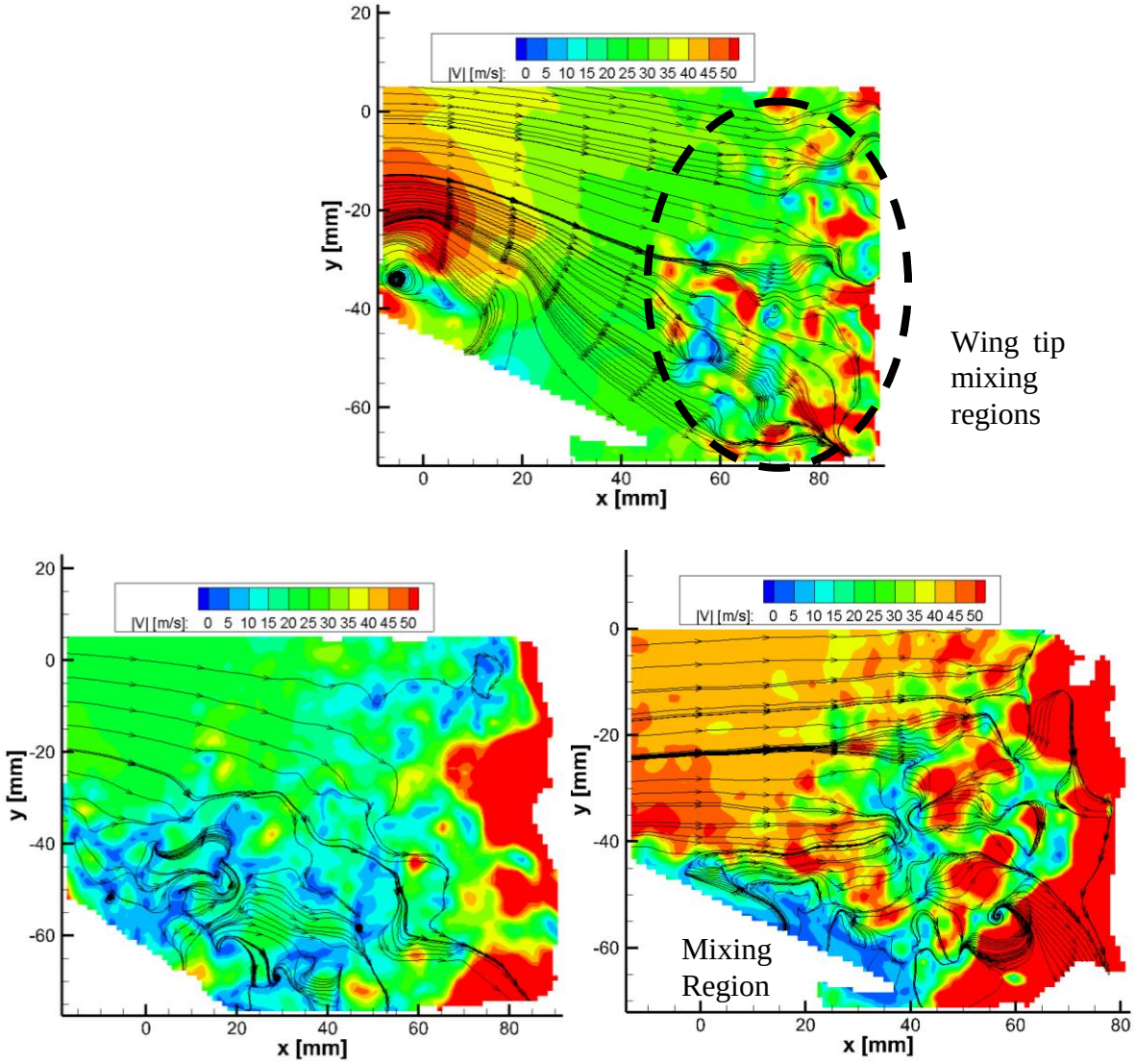

Figure 31. Mixing regions above the trailing edges at x/c = 0.6, 0.8, and 1.0

The formation of these special vortices lie between 0.4 and 0.8 of the wing span and merge with the wing tip vortices at higher pitching angles. Figure 31 shows strong areas of mixing near the beginning of the separation region to be narrower in the 0.4 and 0.8 region and larger in the 0.6 region. This may indicate the presence of the arch vortex formation, however, it may be coincidental. Further 3D flow analysis and tomography will need to be done in order to verify this speculation. The preliminary results strongly suggested that as the sweep angle increases, the presence of wing tip vortices may also increase as well.

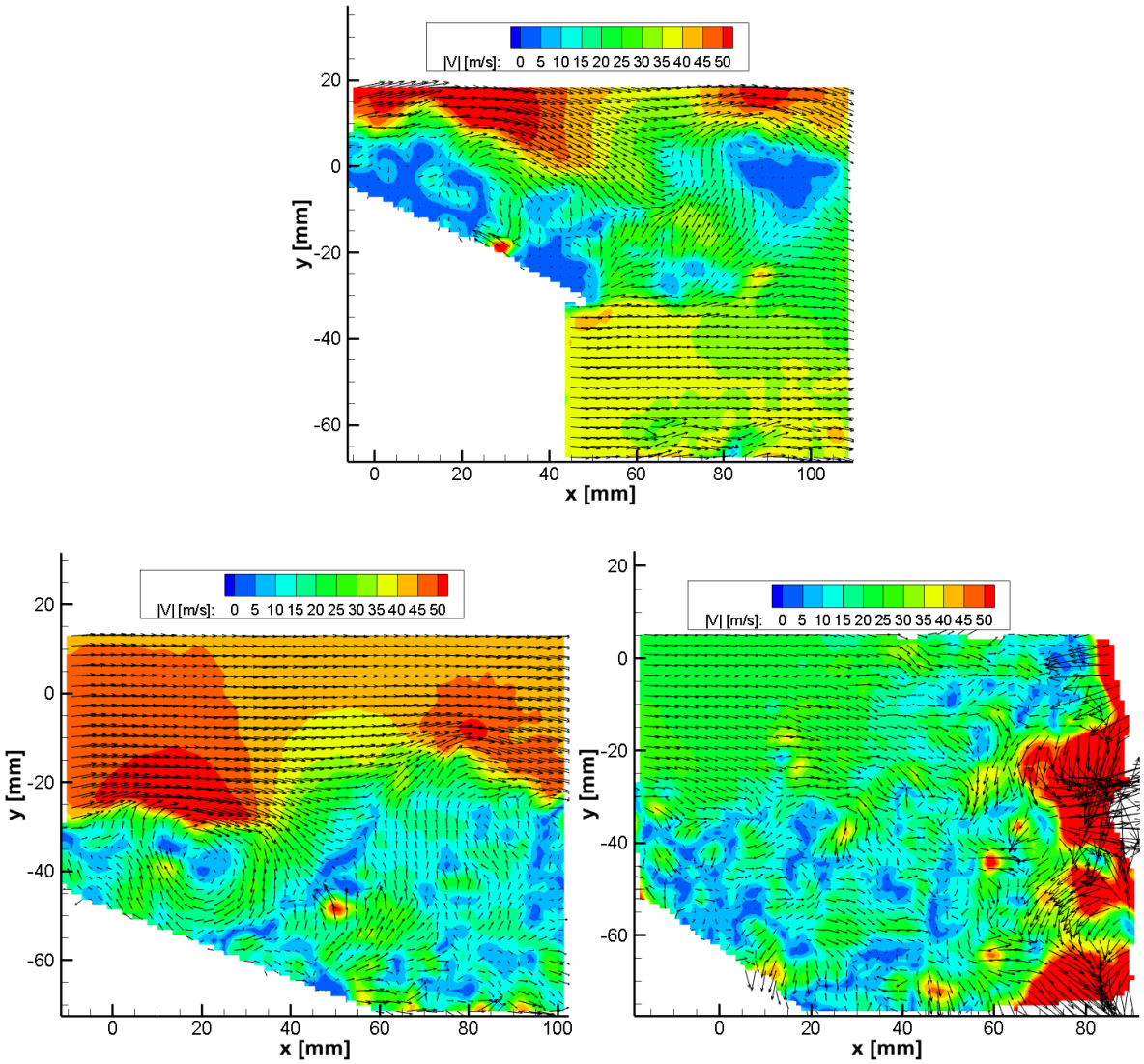

Figure 32. Flow reversal and mixing region comparison

Mixing Region and Flow Reversal Comparison

For the three sweep angles, the mixing region at the wing tip (x/c = 1.0) was evaluated. It was noticed for similar pitching angles, that magnitude of flow mixing increased near the wing tip as sweep angle was increased. Additionally, as the sweep angle was increased, the area of flow reversal became more chaotic and the separation region increased in size. The flow shedding off the separation region was also consequently more turbulent and less uniform. Figure 32 above compares the separation region at mid span just after stall for the three swept cases.

CHAPTER 6. CONCLUSION

In this research, the dynamic stall characteristics of a pitching finite aspect ratio were explored. The effect of dynamic motion, sweep angle, and wingspan location were all considered for this analysis. It was found that the angle at which flow separates from the surface of the airfoil was prolonged by about 5-7º before undergoing complete stall as indicated by flow reversal preceding turbulent flow separation. After the airfoil reached its maximum pitching angle, it was observed flow would reattach on the down stroke after its maximum stall angle was reached. It was found that the pitching angle where flow would begin to reattach was influenced by its relative sweep angle. Leading edge reattachment was prolonged down the length of the wing span and as sweep angle was increased. For the unswept case, flow reattachment at the leading edge occurred approximately the same angle which it stalled at, whereas for the 15º and 27.6° swept cases, flow separation would be prolonged closer to 20° and 22°. Respectively. Additionally, flow would reattach sooner near the root of the wing and later near the wing tip. The swept cases showed a higher degree of mixing further down the wing span likely due to the mixing of leading edge and wing tip vortex shedding. Detached arch and ring vortices were not confidently identified for the 0º and 15º swept cases, although some prolonged flow reversal was observed. However, a strong presence of secondary vorticity and mixing was observed for the 27.6º swept case. It was speculated that this secondary vorticity could be indicative of arch vortex shedding in which its rotational presence may assist in an earlier flow reattachment during the pitching cycle.

Future Work

This analysis only scratched the surface in exploring the dynamic stall of a swept wing. Two dimensional PIV was only capable of investigating flow at a few points of interest. Since

dynamic flow structure is so complicated, a three dimensional analysis should be used for future work. The application of Tomographic PIV would give a more accurate representation of flow across the entirety of the wing span. Further research beyond this thesis utilizing three dimensional analysis are planned to be carried out in the future.

REFERENCES

[1] Kenneth W. McAlister, Lawrence W. Carr and William J. McCroskey, “Dynamic Stall Experiments on the NACA 0012 Airfoil,” January 1978, NASA Technical Paper 1100, pp. 2-5

[2] D. Kuchemann and J. Weber, “The Subsonic Flow Past Swept Wings at Zero Lift Without and With Body,” Aeronautical Research Council of London England, March 1953, pp. 3-9

[3] Miguel R. Visbal and Daniel J. Garmann, “Computational Investigation of the Effect of Sweep on a Pitching Finite-Aspect-Ratio Wing,” January 2018, Kissimmee Florida, pp. 2

[4] Miguel R. Visbal and J. S. Shang. "Investigation of the flow structure around a rapidly pitching airfoil," AIAA Journal, Vol. 27, No. 8 (1989), pp. 1044-1051.

[5] Houghton, E. L.; Carpenter, P.W, Butterworth Heinmann, ed. “Aerodynamics for Engineering Students” (5th ed.), 2003, pp. 24

[6] Christopher Rumsey, “2D NACA 0012 Airfoil Validation Case,” Turbulence Modeling Resource, April 11th, 2018, NASA Langley Research Center, Available Online

[7] I. Gursul, Z. Wang, E. Vardaki, “Review of flow control mechanisms of leading-edge vortices,” Department of Mechanical Engineering, University of Bath, Bath BA2 7AY, UK, Available online 10 October 2007.

[8] Miguel R. Visbal and Daniel J. Garmann, “High-Fidelity Simulation of Dynamic Stall over a Finite-Aspect-Ratio Wing,” AIAA Paper 2016-4243, June 2016, pp. 2-9

[9] Brian Lander, “Mixing Characteristics of Turbulent Twin Impinging Axisymmetric Jets at Various Impingement Angles,” University of Cincinnati, Engineering and Applied Science: Aerospace Engineering, June 2016, pp. 11

[10] Y. Zhang, S. Bhusal, J. Krech, and J. Estevadeordal, "Effects of Leading-Edge Structures on Stall Behaviors of a NACA0015 Airfoil: A Multi-plane PIV Study." Proceeding of 34th AIAA Applied Aerodynamics Conference. Washington D.C., 2016, pp. 4-13

[11] Adam Stolt, Jordi Estevadeordal, Jesstin Krech, and Yan Zhang, "A tomographic PIV and TSP Study of Leading-Edge Structures on Stall Behaviors of NACA0015." January 2017, Department of Mechanical Engineering, North Dakota State University, Fargo, ND, 58108, pp. 3

[12] SAE, "Going with the flow." Aerospace Engineering & Manufacturing, March 2009, Society of Automotive Engineers, pp. 26-27

APPENDIX A. EXTERNAL TRIGGER TIME DELAY EXAMPLE – F = 30 Hz

Global Parameters:

U	35.907345	38.5 Actual	f	30	Hz
α,min	0	deg	Ang vel	10800	deg/s
α,max	22	deg	Pitching Rate	1320	deg/s
Δα	22	deg		0.0007576	s/degree
Δα,tot	44	deg	Pitching Period	33.33333333	ms/period
Chord Length	0.0762	m			
α,initial,forward	12.5				
α,initial,reverse	15.3		Camera-Laser	0.165	ms
k factor	0.2		Delay		
Λ					

	x/c	0		
Test Number	α	Direction	Camera Delay (ms)	Laser Delay (ms)
1	10.9	UP	30	29.835
2	13	UP	31.59090909	31.42590909
3	19.4	UP	3.106060606	2.941060606
4	21.3	UP	3.792470156	3.627470156
5	22	UP	3.403386482	3.238386482
6	21.3	DOWN	3.108626123	2.943626123
7	18.8	DOWN	4.248959184	4.083959184
8	16.4	DOWN	5.037090291	4.872090291
9	13	DOWN	6.391735069	6.226735069

APPENDIX B. EXTENDED RESULTS FOR FLOW STRUCTURE OVER Λ=0º

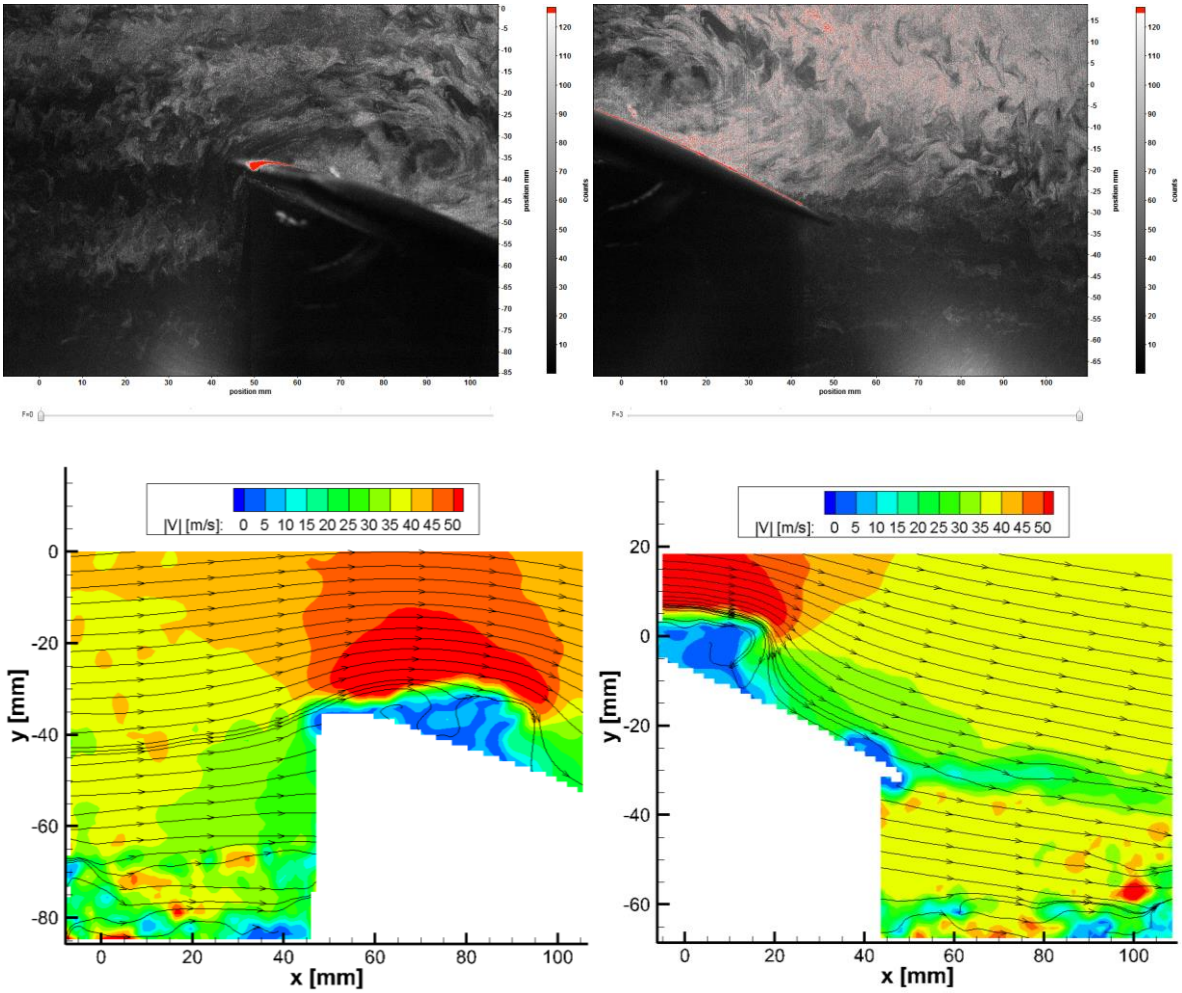

α = 21.1º↑, x/c = 0.4 (174)

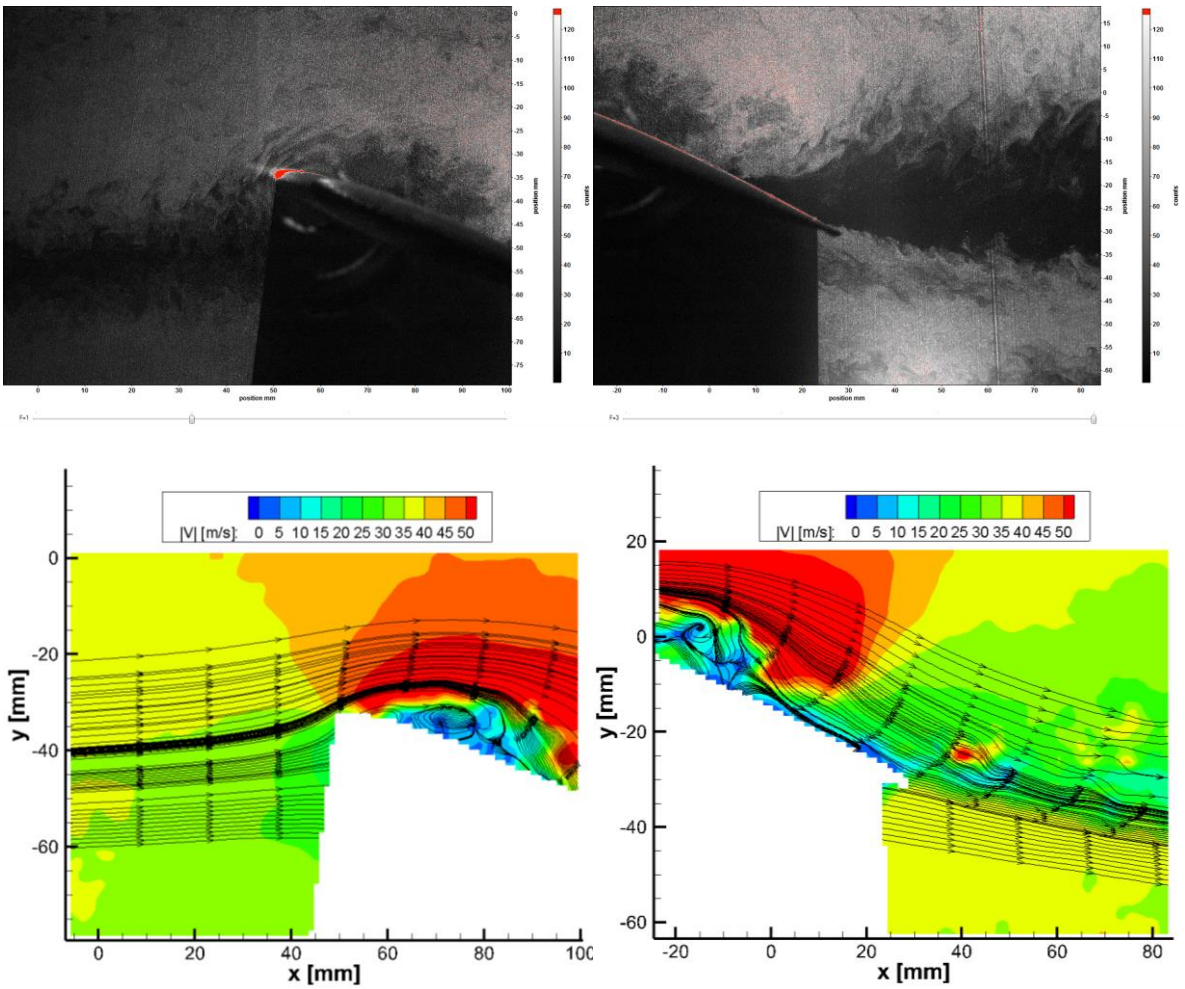

α = 20.9º↑, x/c = 0.6 (287)

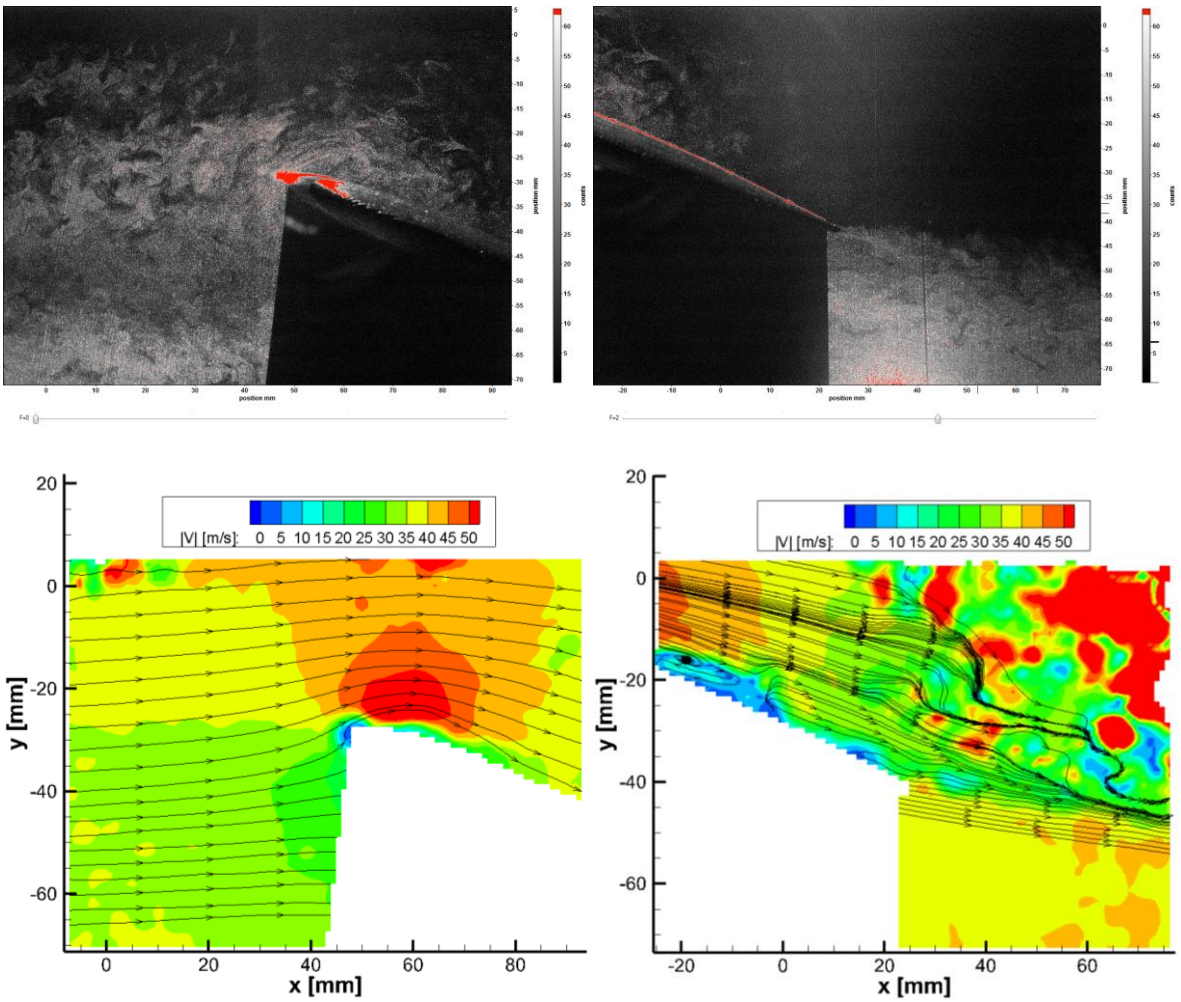

α = 20.6º↑, x/c = 0.8 (340)

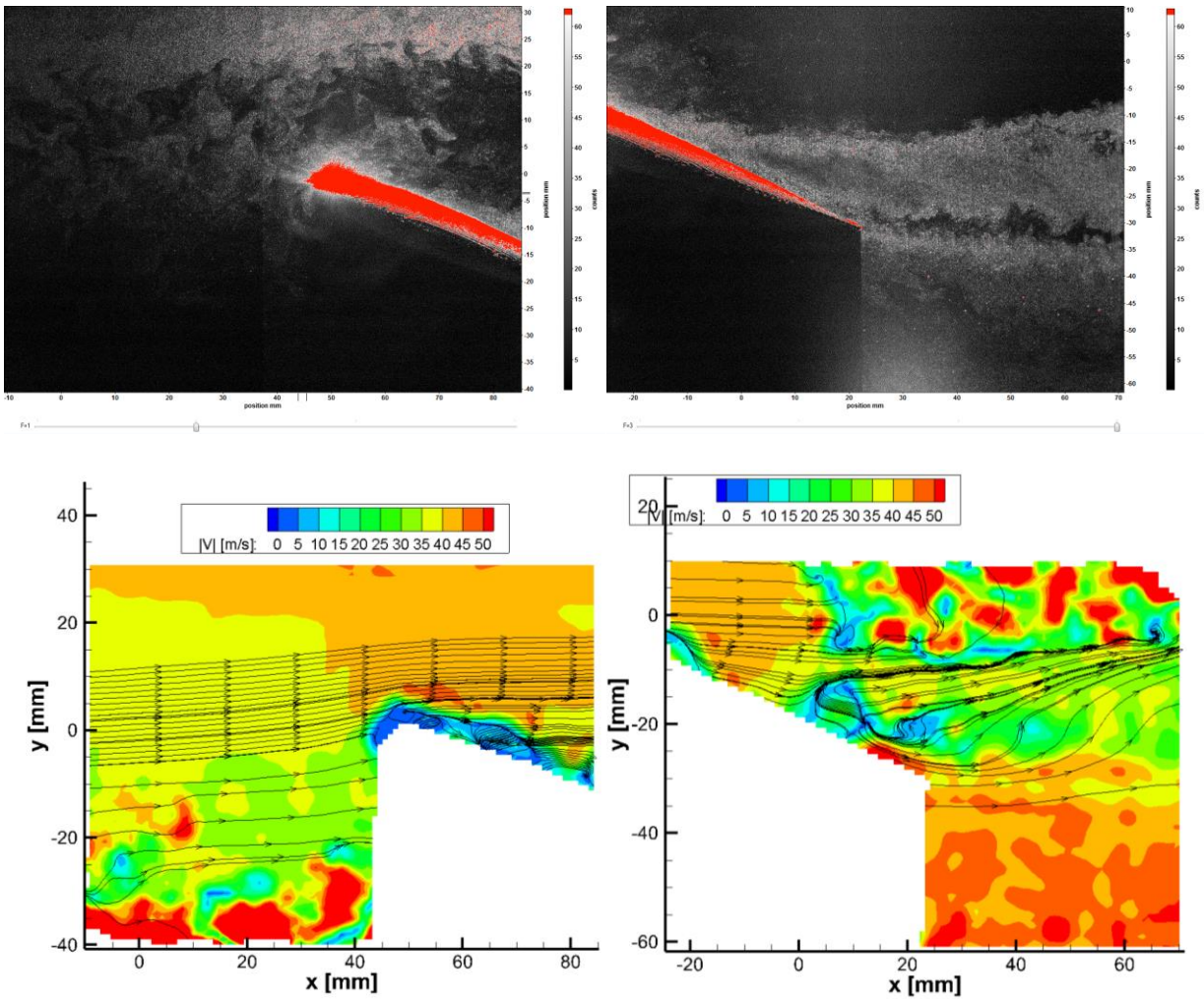

α = 21.2º↑, x/c = 1.0 (162)

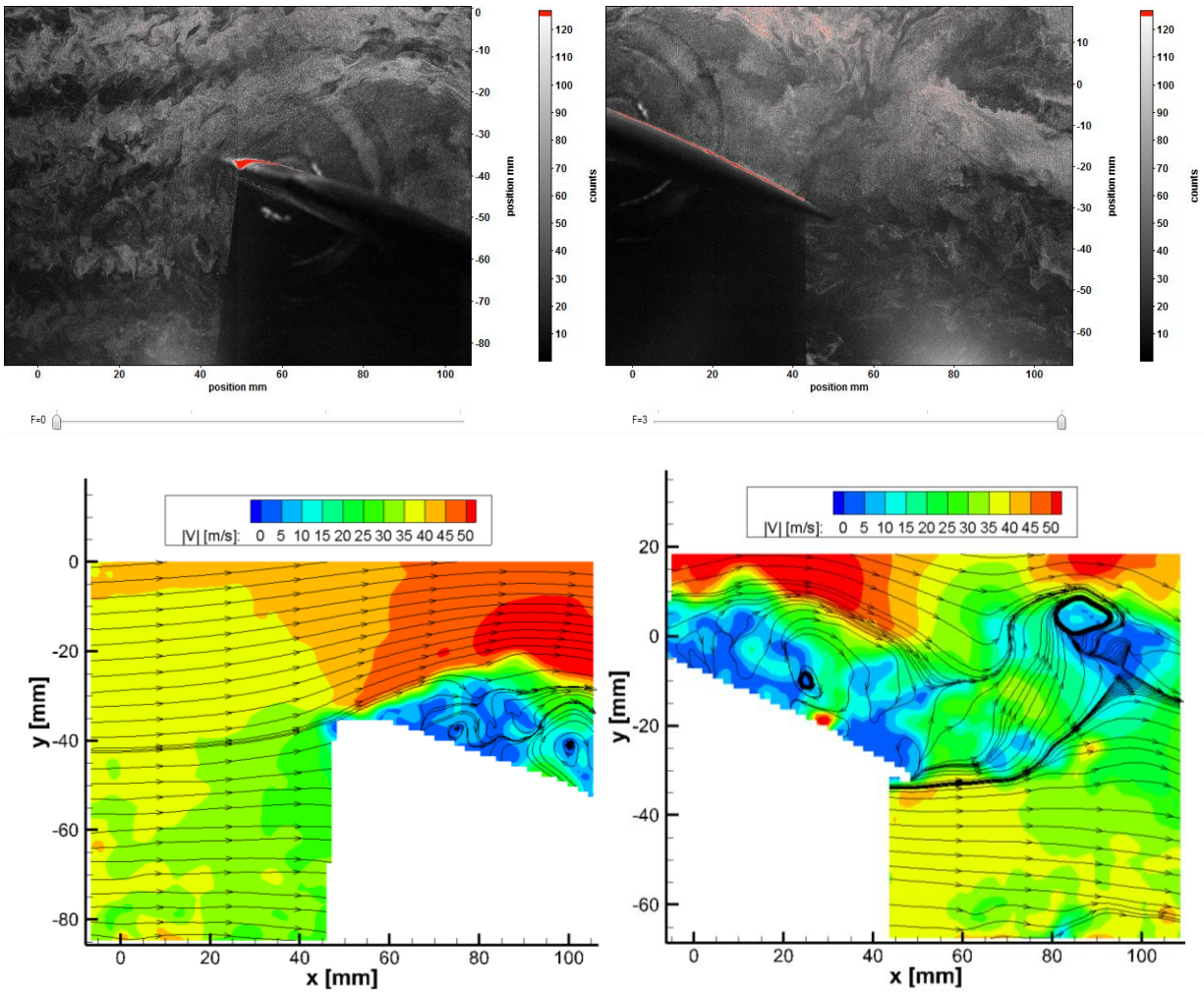

α = 21.2º↓, x/c = 0.4 (186)

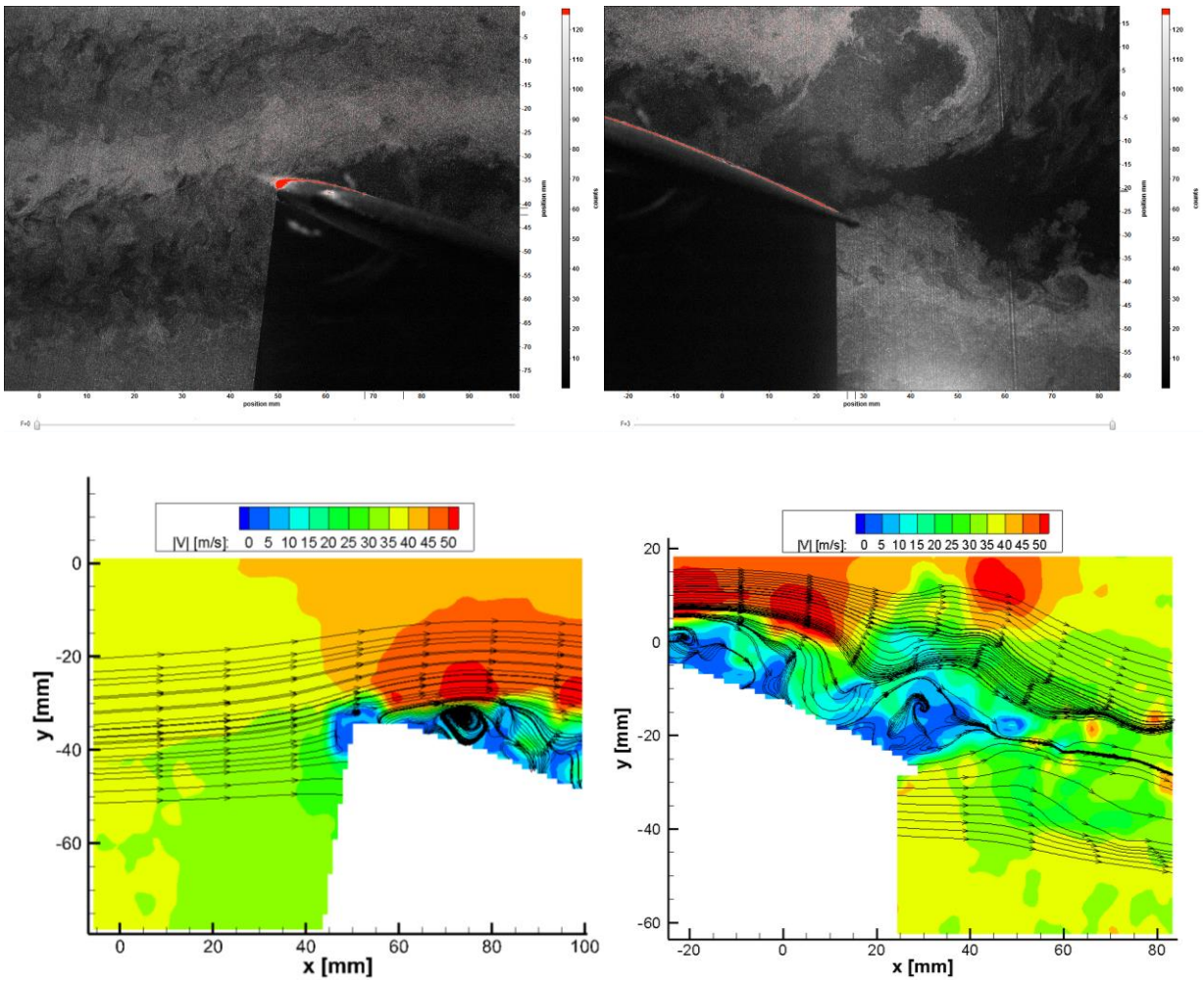

$\alpha = 21.0^{o}\downarrow$, x/c = 0.6 (248)

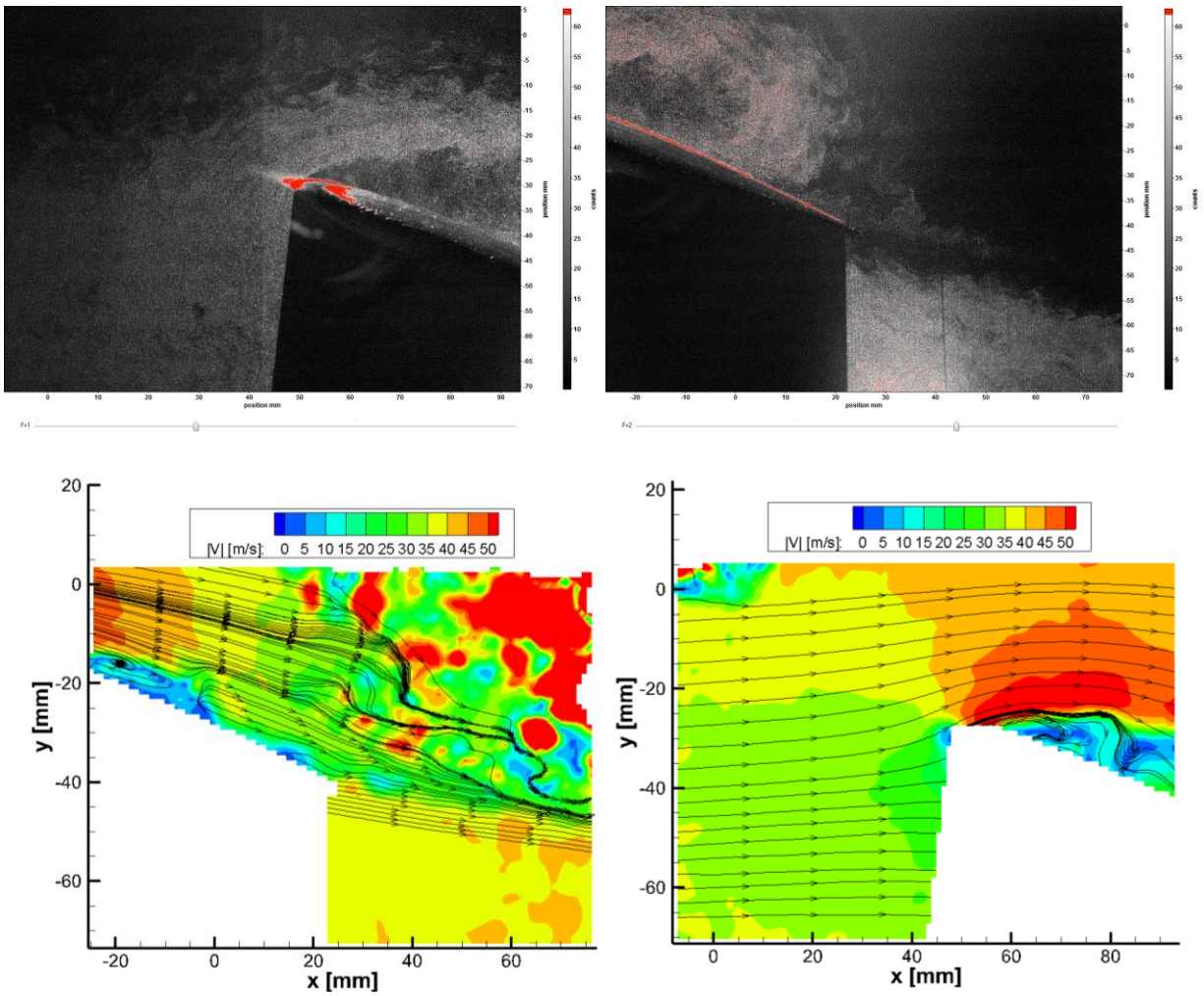

$\alpha = 20.3^{o}\downarrow$ x/c = 0.8 (341)

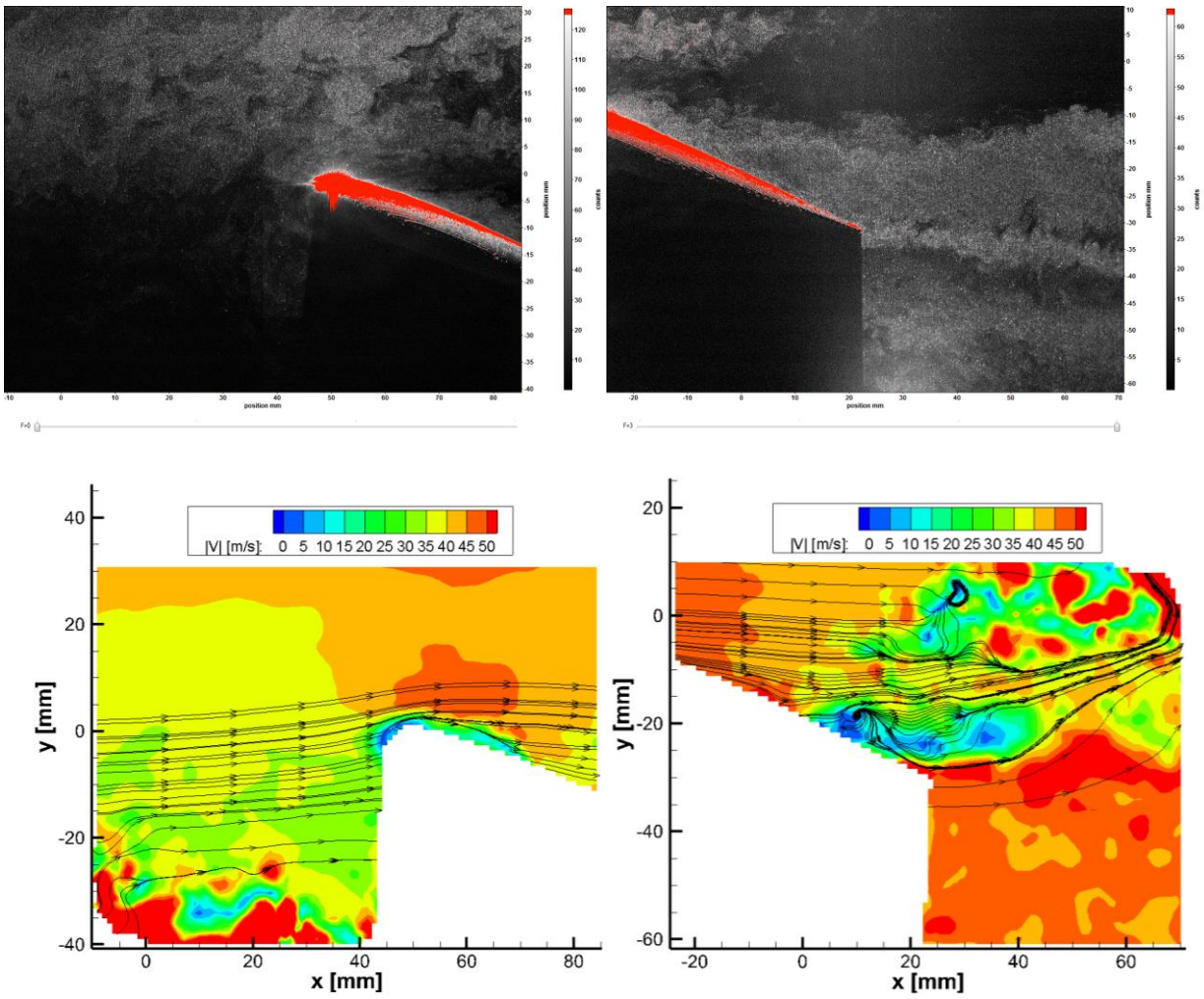

α = 21.9º↓, x/c = 1.0 (163)

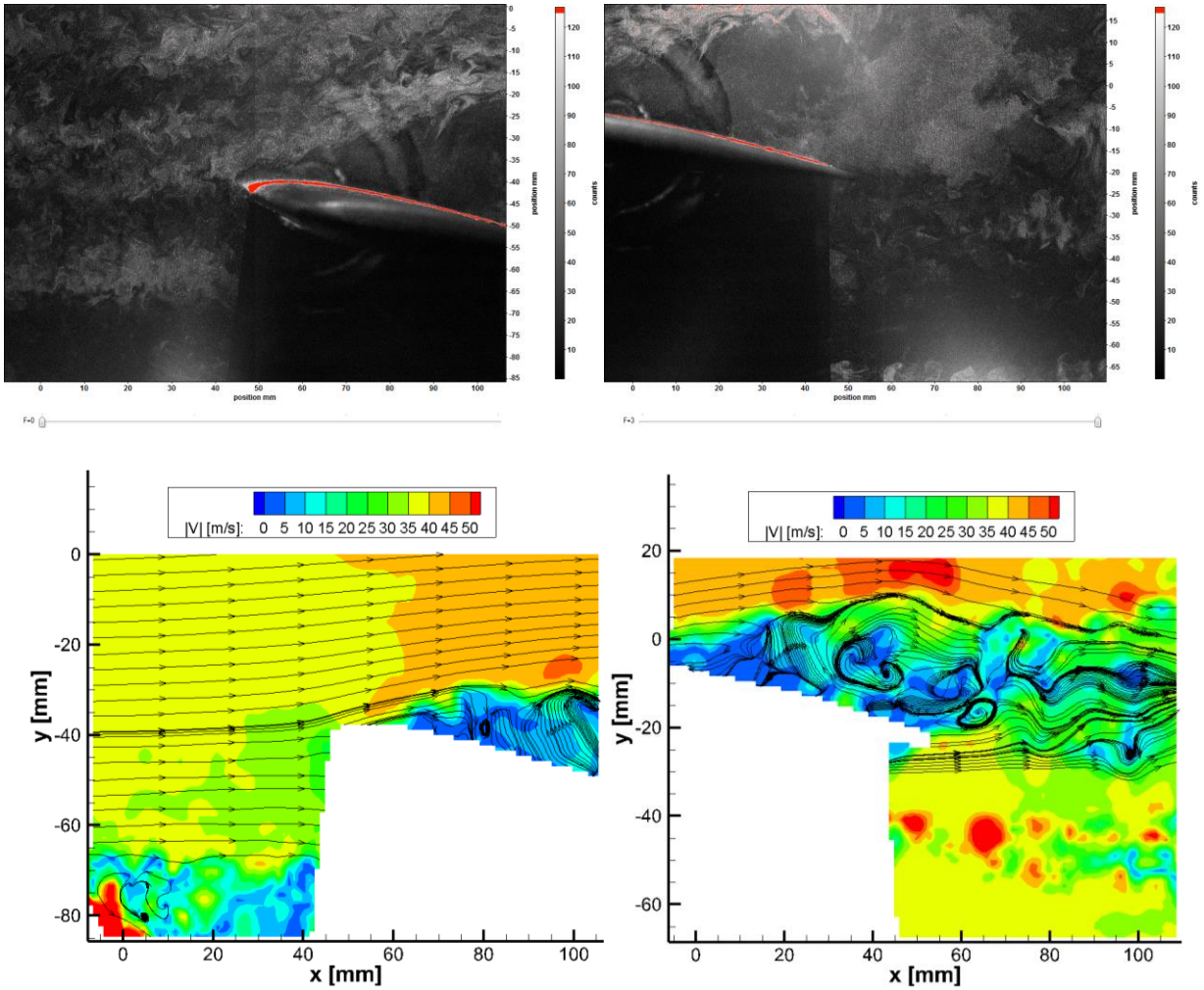

$\alpha = 14.4^{o}\downarrow$, x/c = 0.4 (328)

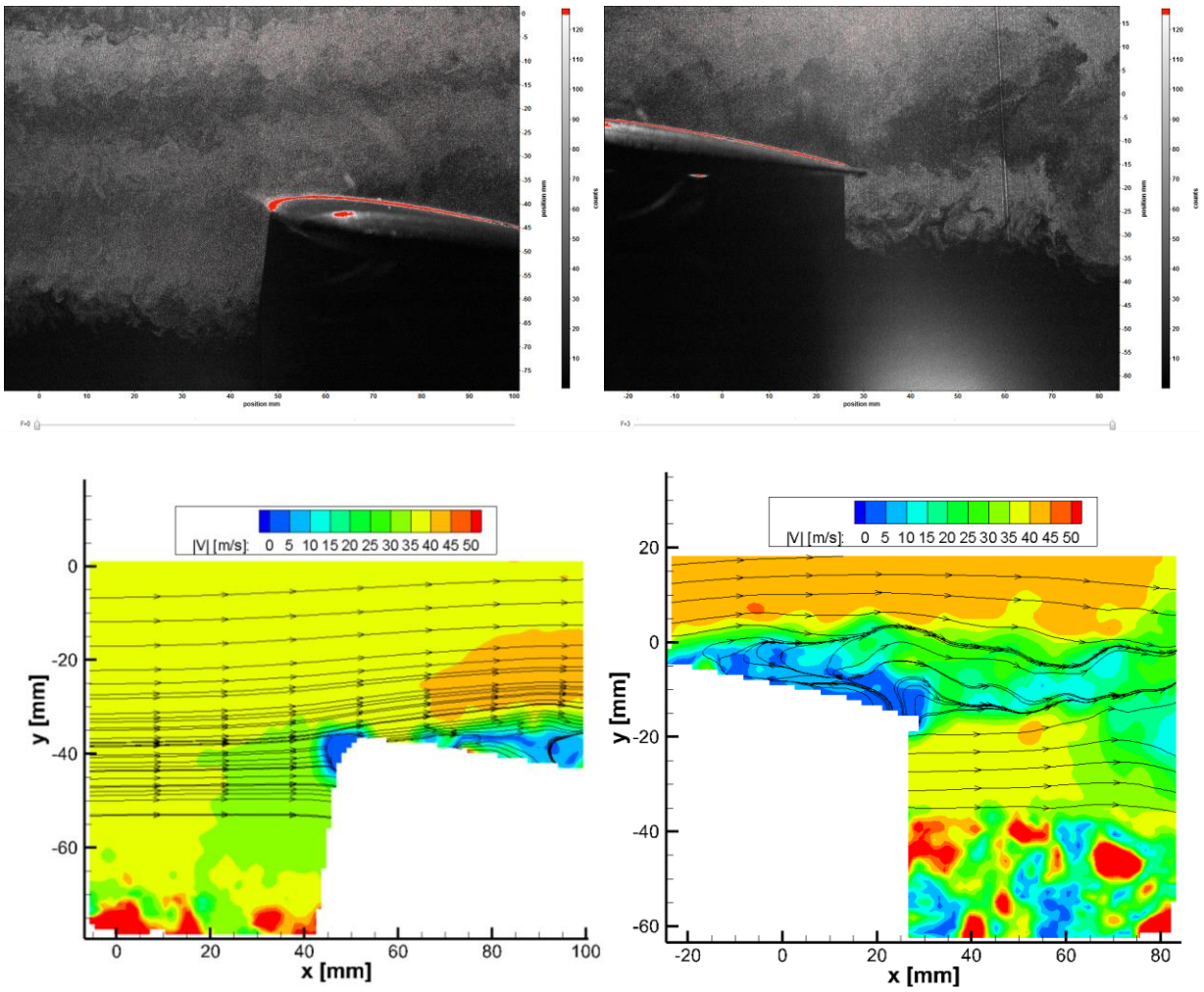

α = 14.8º↓, x/c = 0.6 (332)

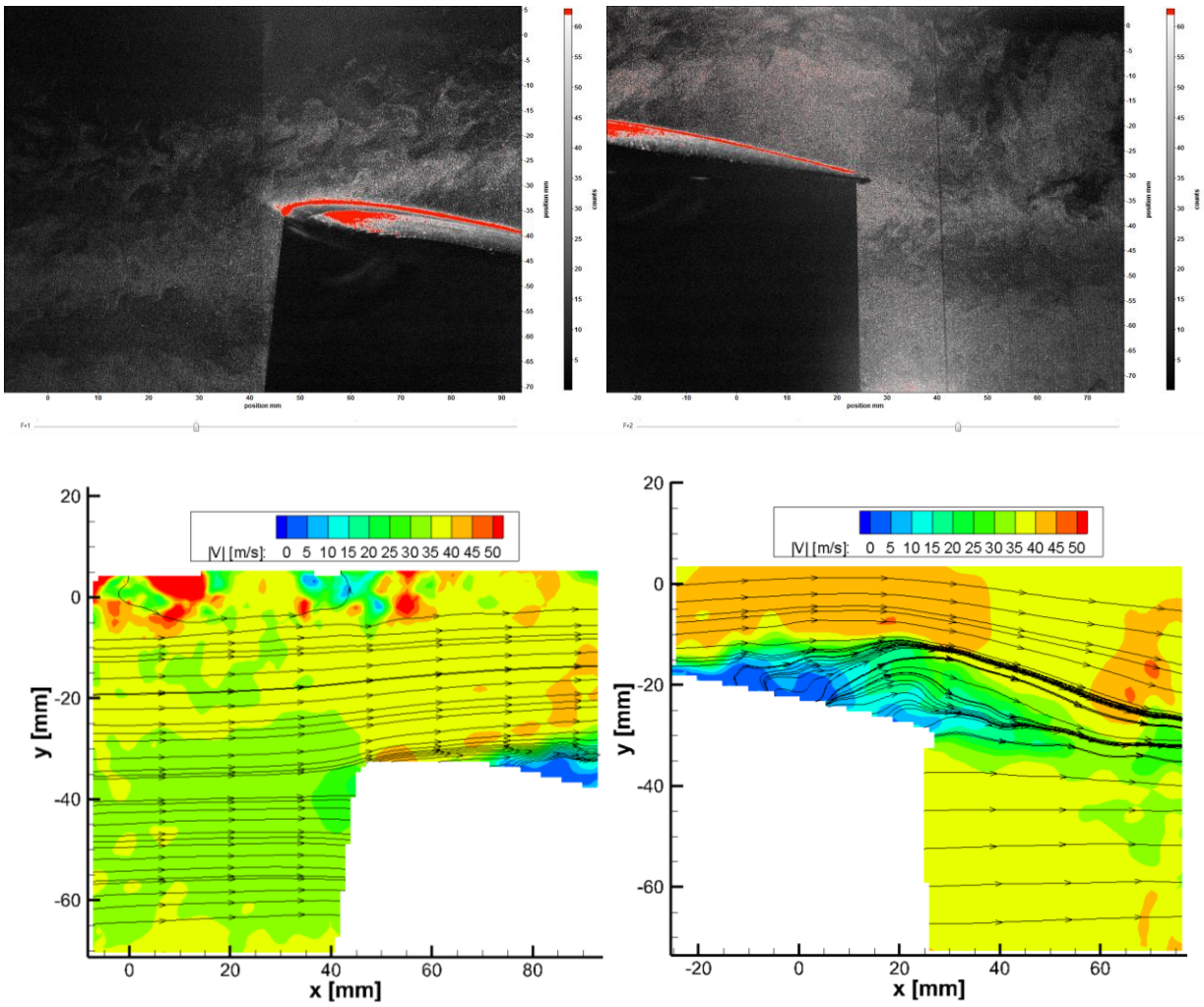

α = 14.7º↓, x/c = 0.8 (299)

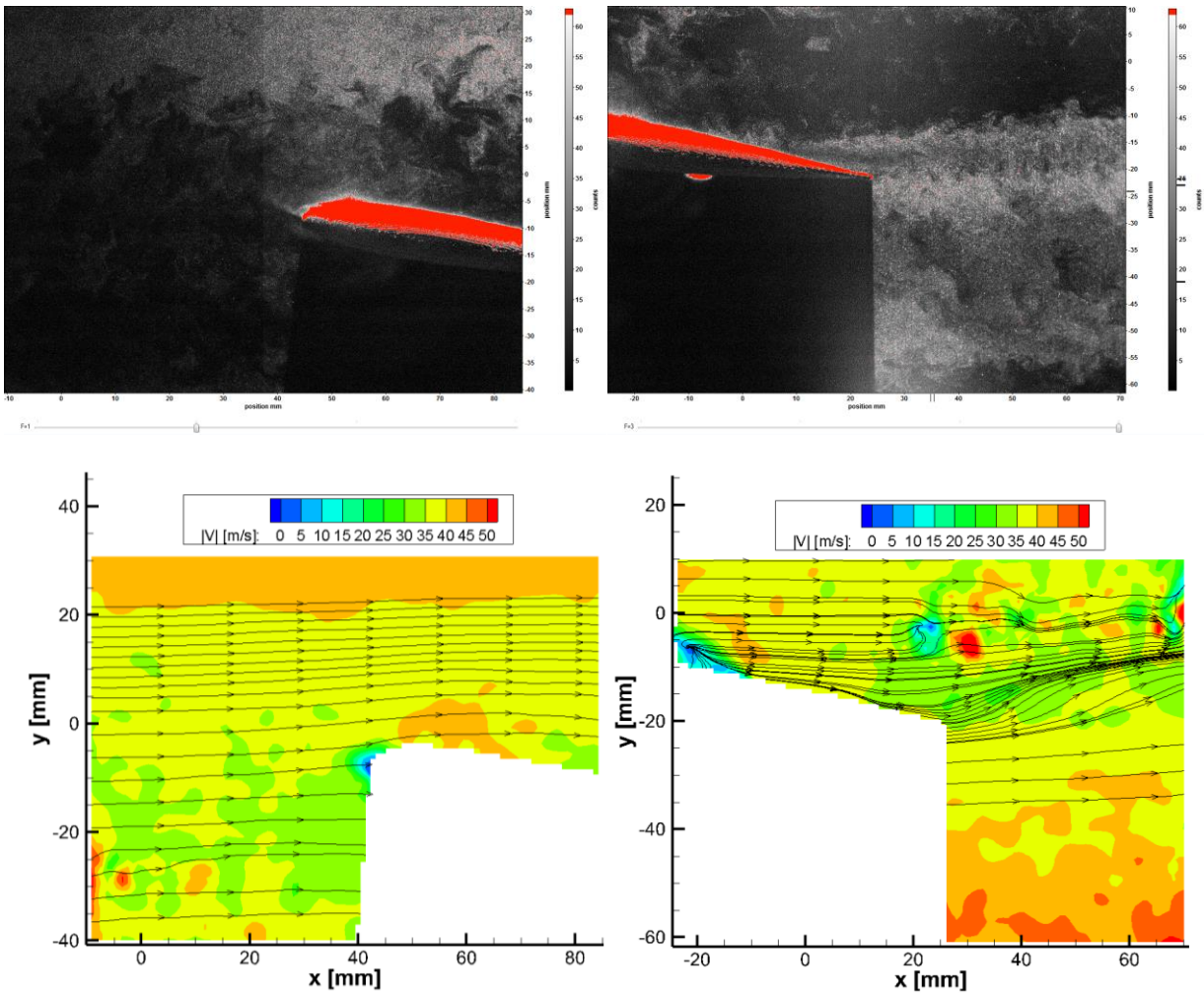

α = 12.3º↓, x/c = 1.0 (136)

APPENDIX C. EXTENDED RESULTS FOR FLOW STRUCTURE OVER $\Lambda=15^{o}$

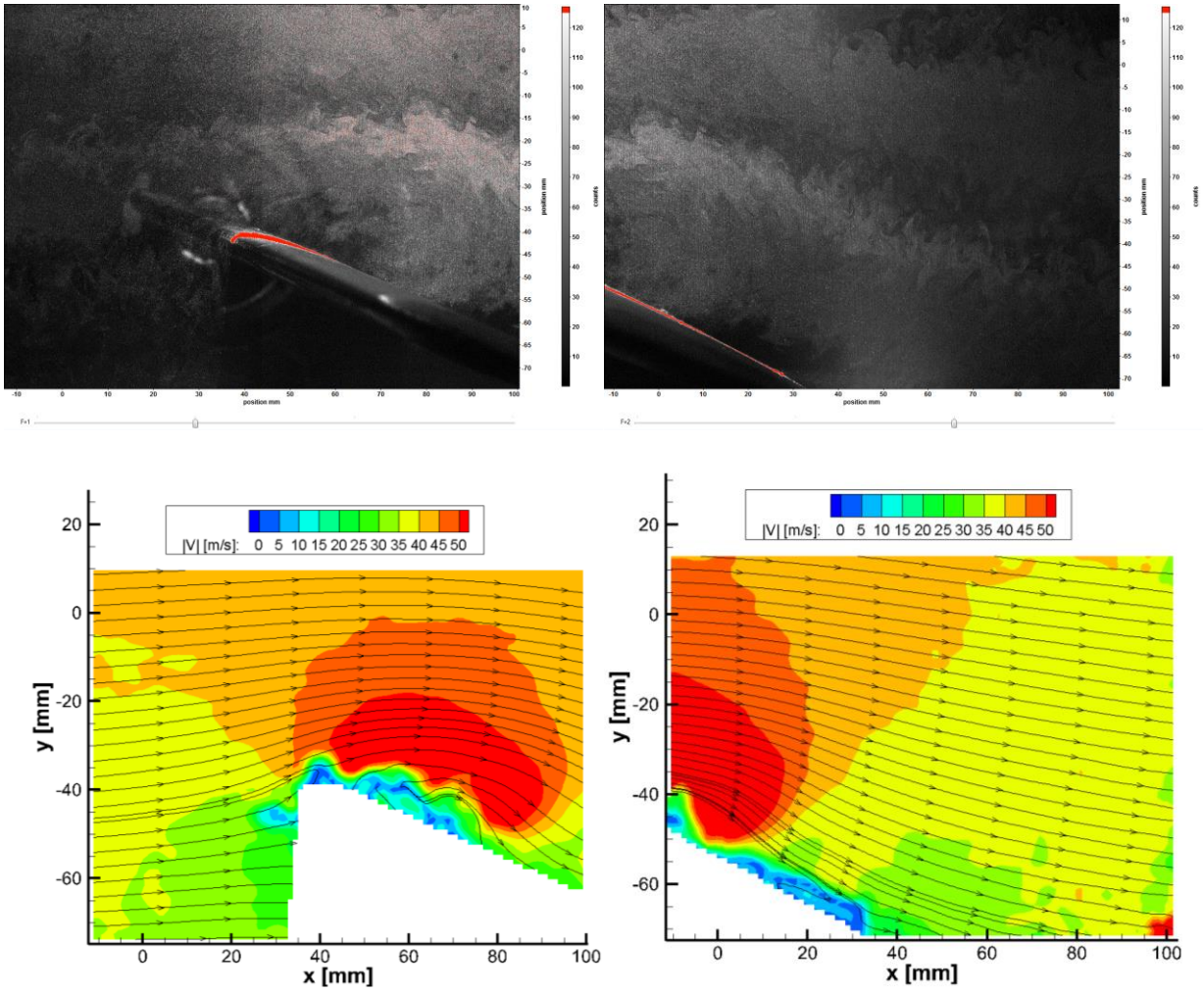

$\alpha = 22.1^{o}\uparrow$, x/c = 0.4 (424)

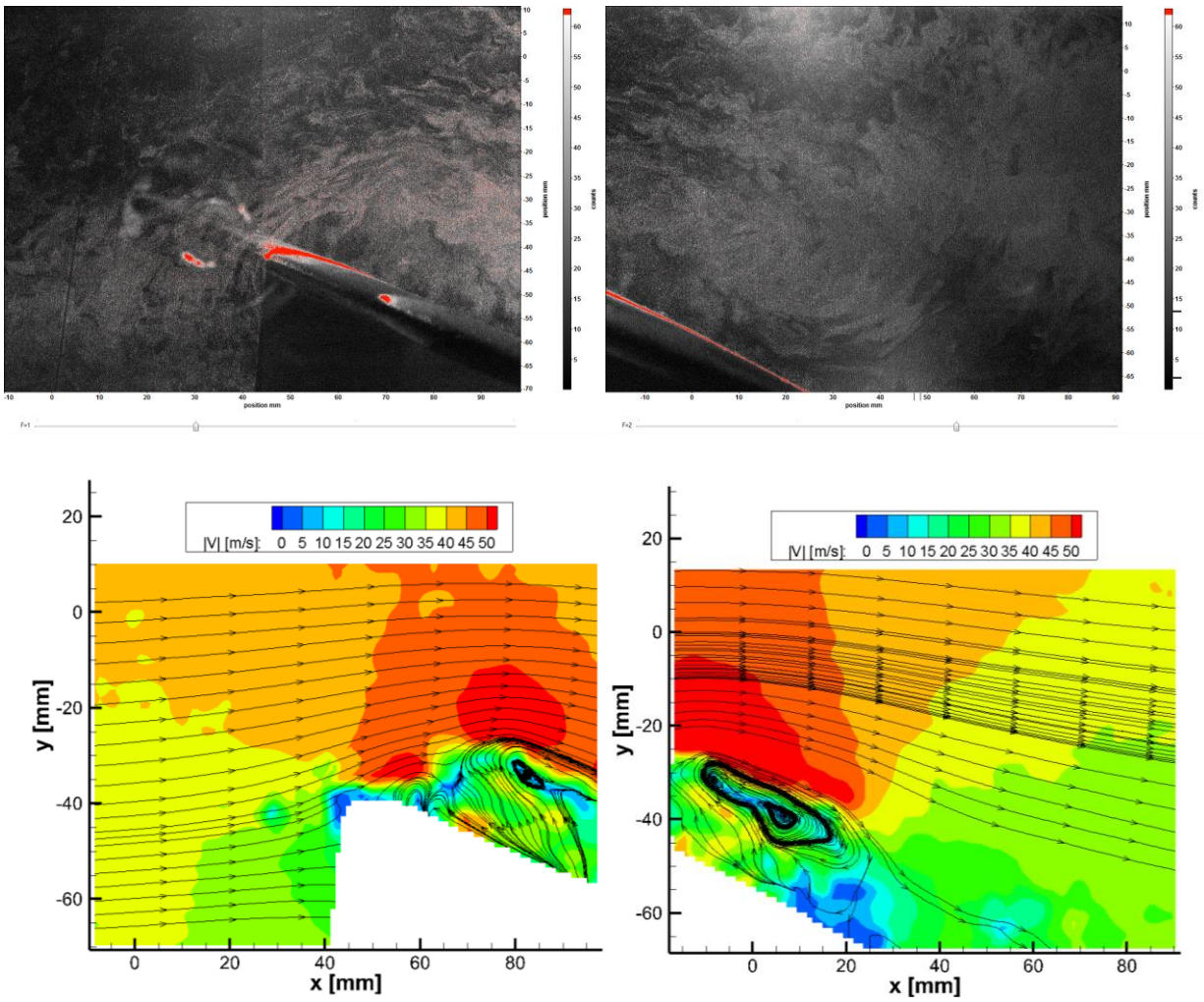

α = 21.8º↑, x/c = 0.6 (268)

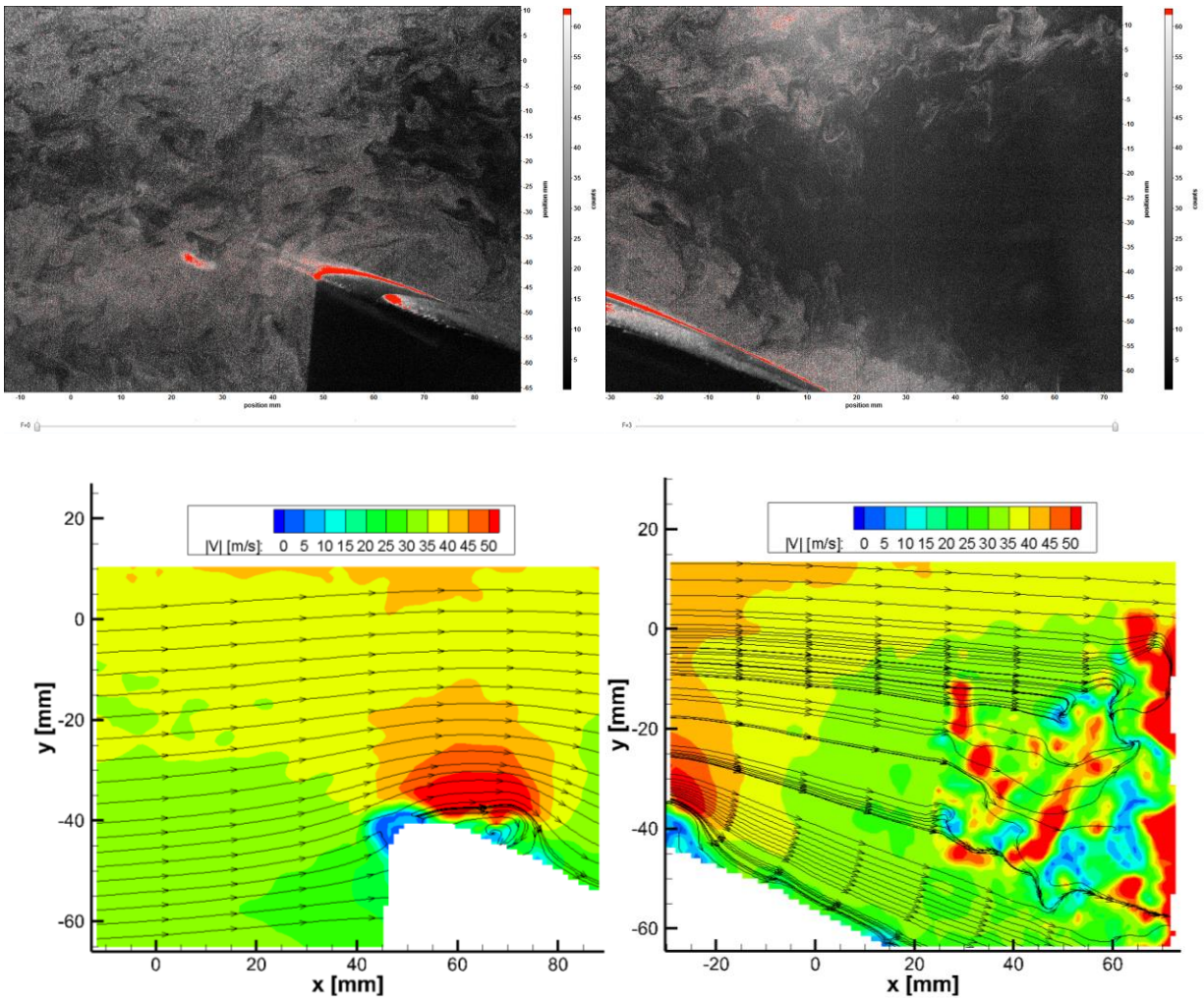

α = 22.1º↑, x/c = 0.8 (234)

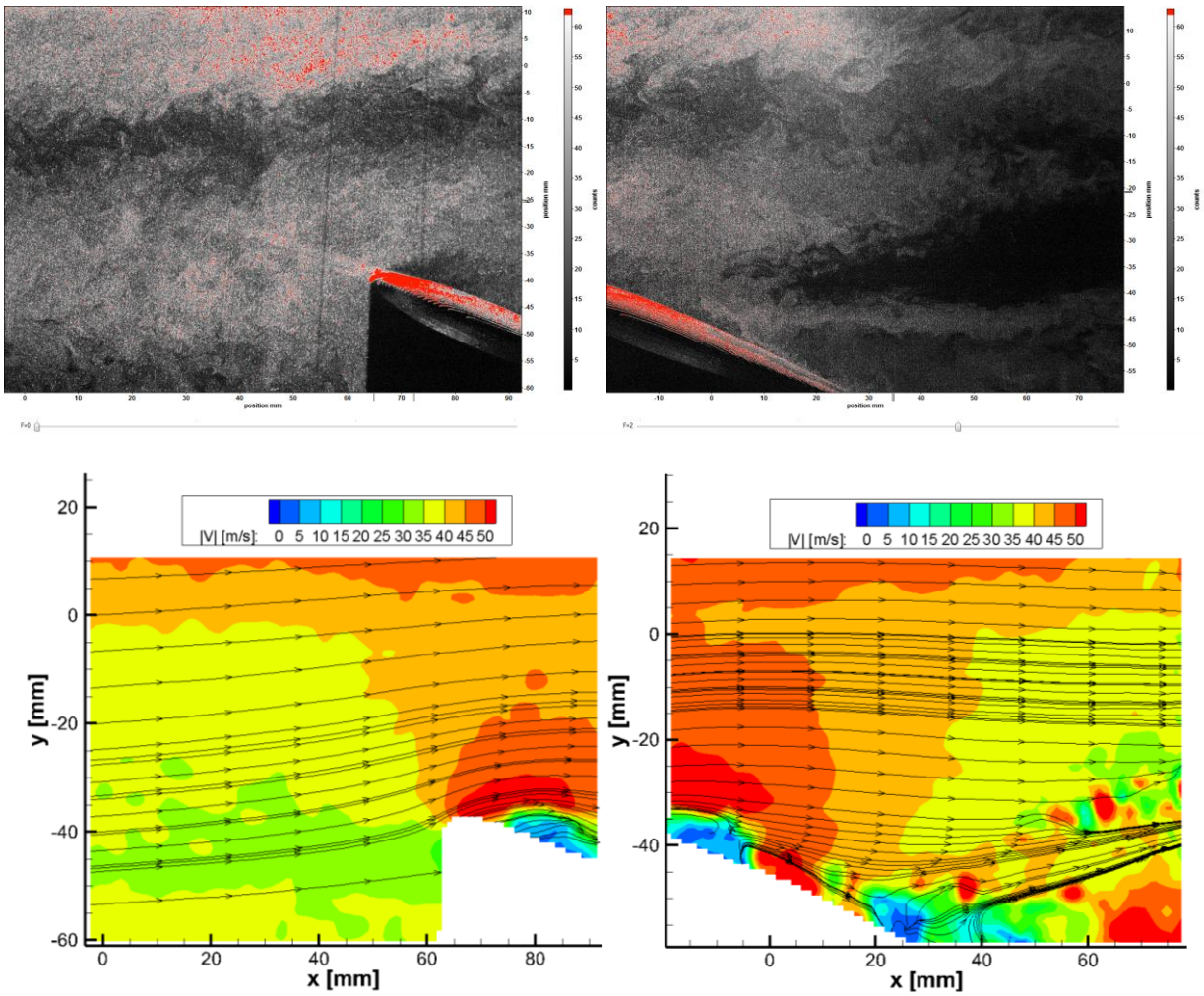

α = 21.7º↑, x/c = 1.0 (376)

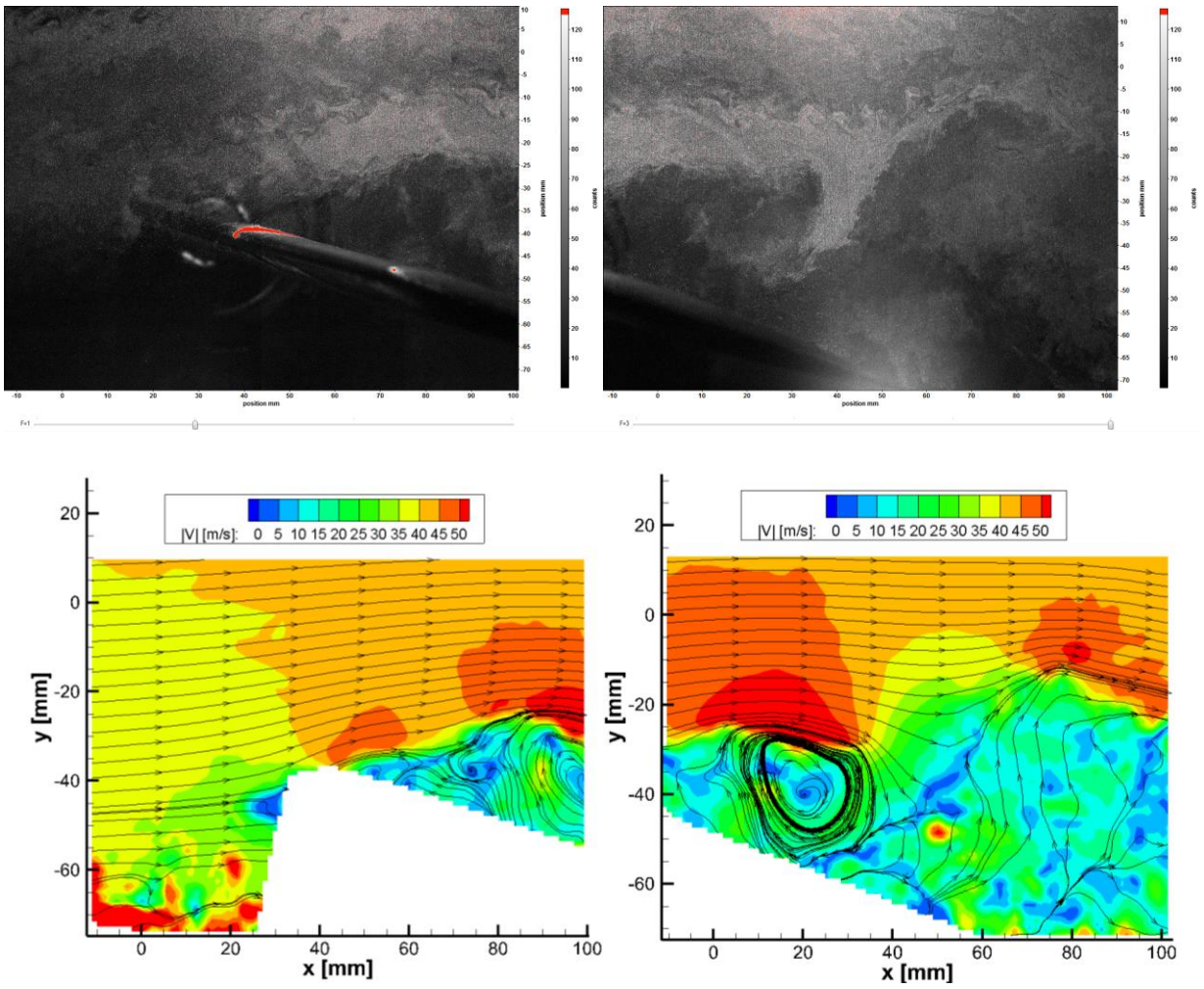

α = 19.5º↓, x/c = 0.4 (425)

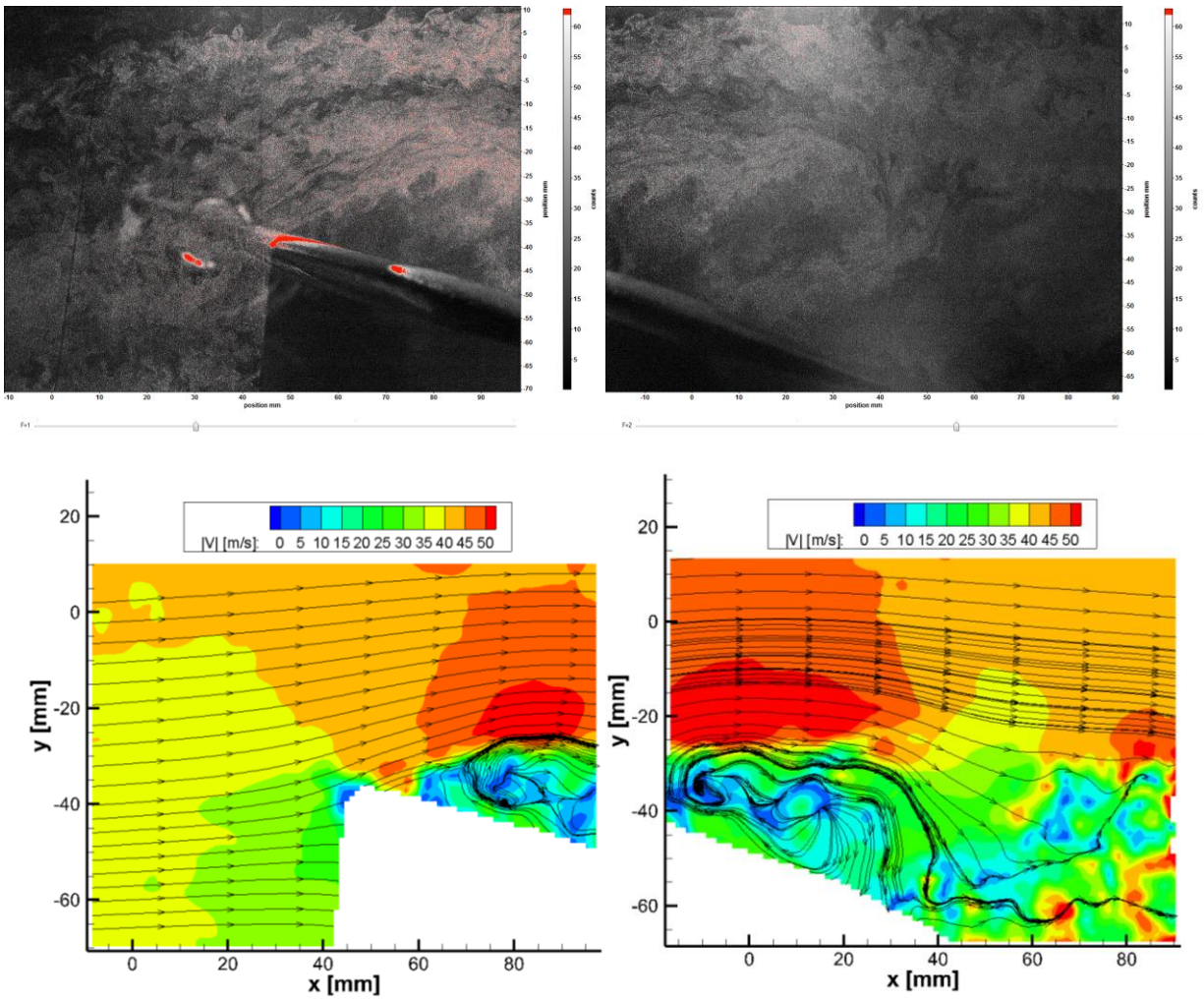

α = 19.0º↓, x/c = 0.6 (269)

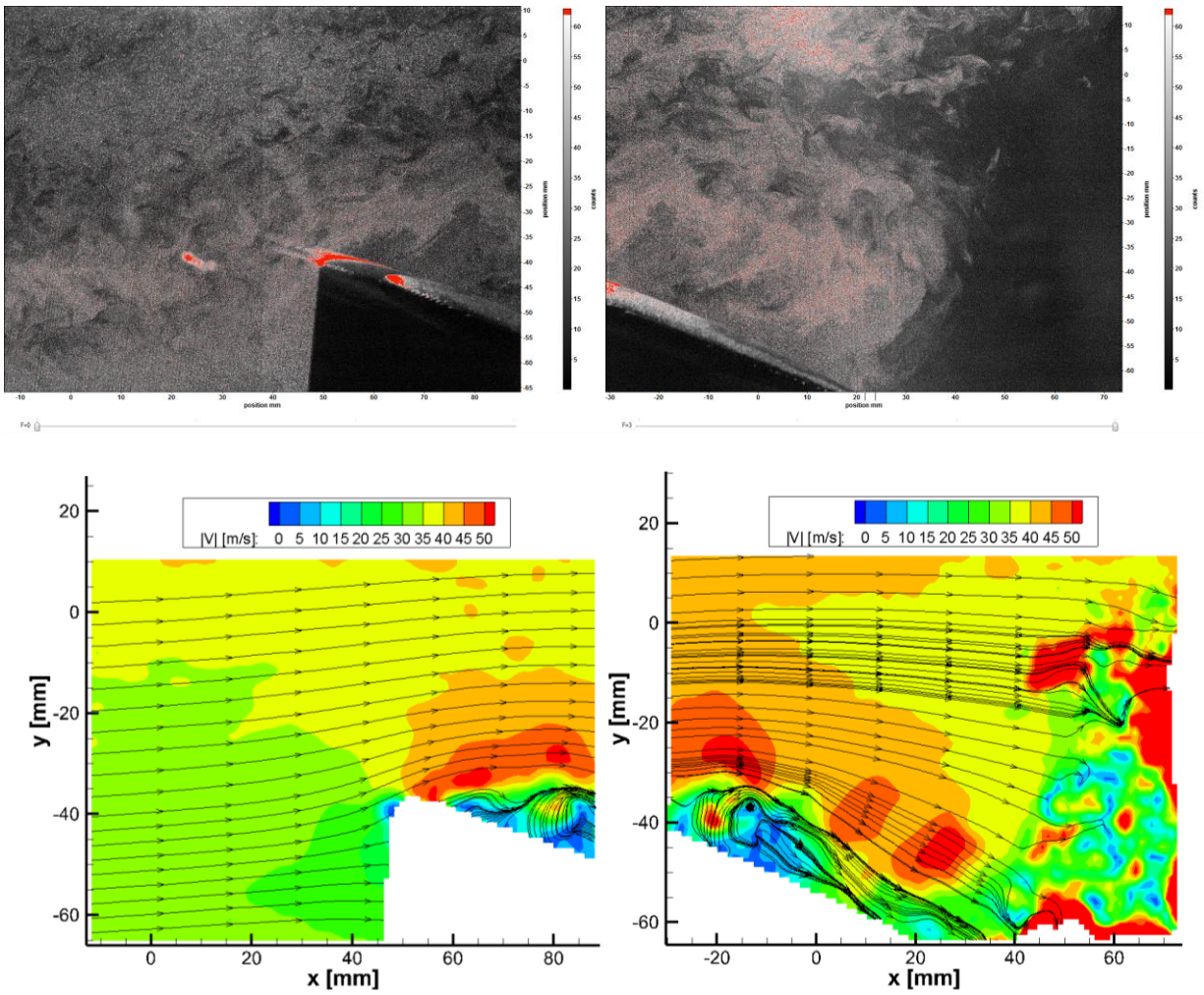

α = 22.1º↓, x/c = 0.8 (235)

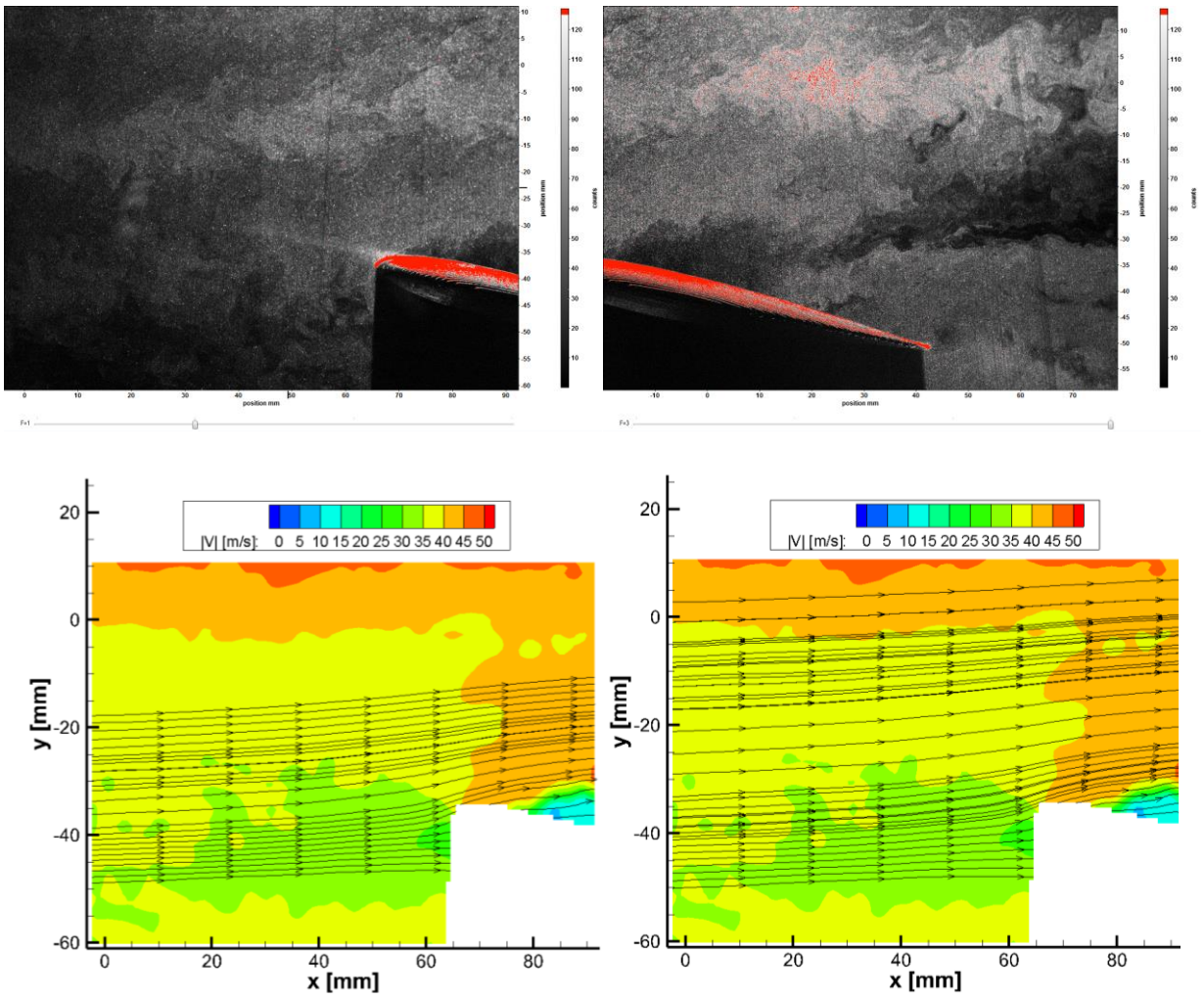

α = 17.6º↓, x/c = 1.0 (378)

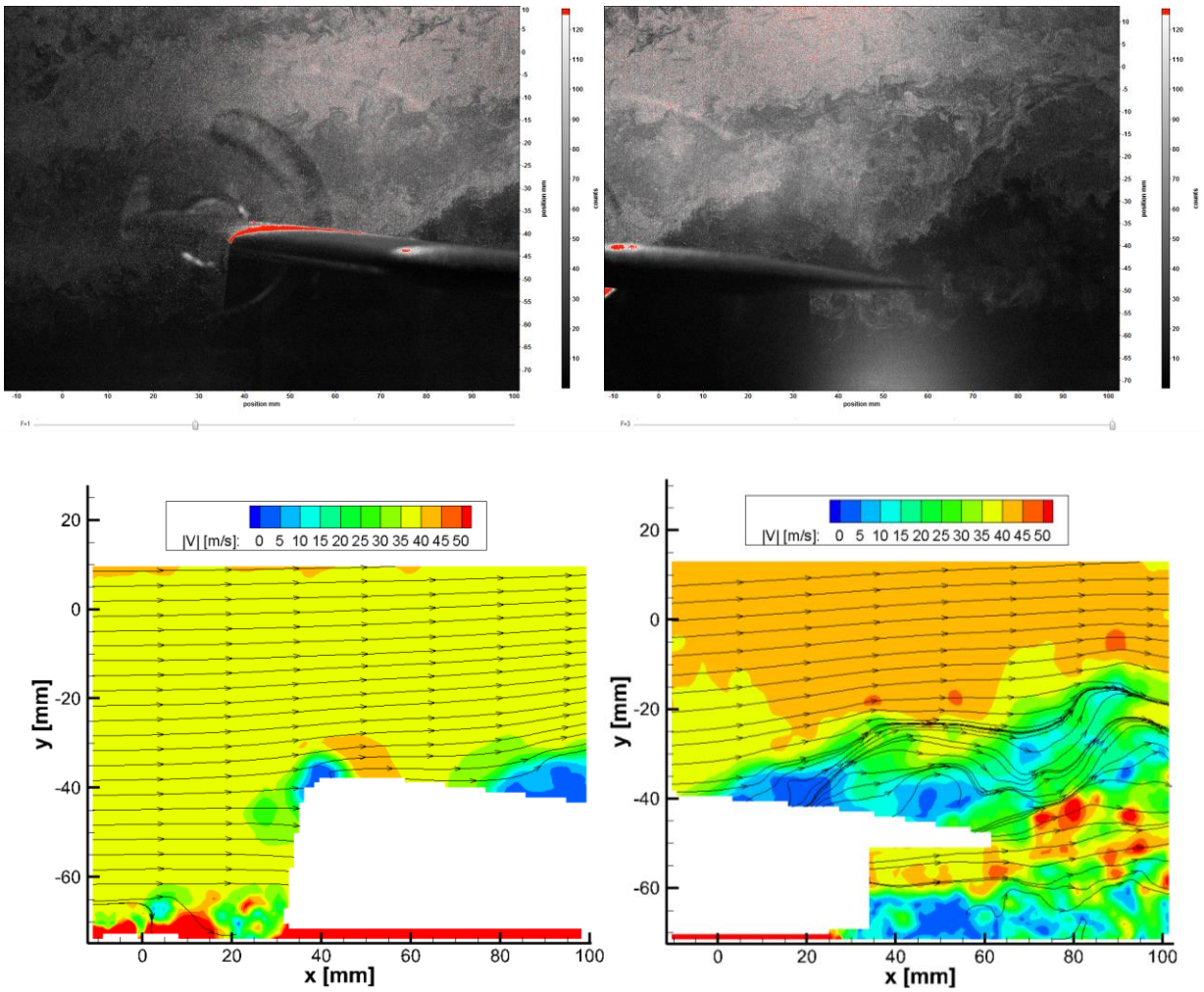

α = 12.8º↓, x/c = 0.4 (426)

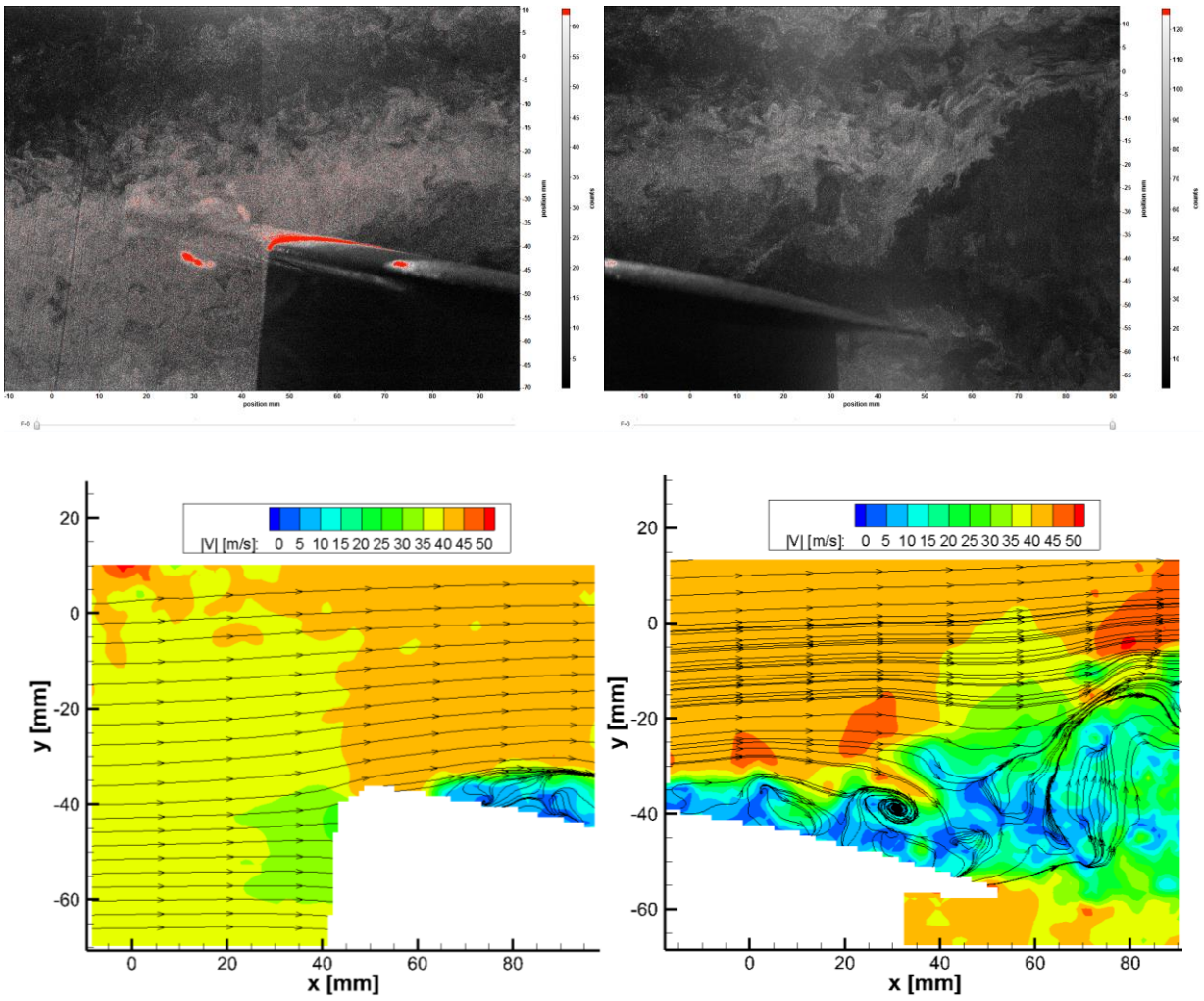

α = 14.5º↓, x/c = 0.6 (270)

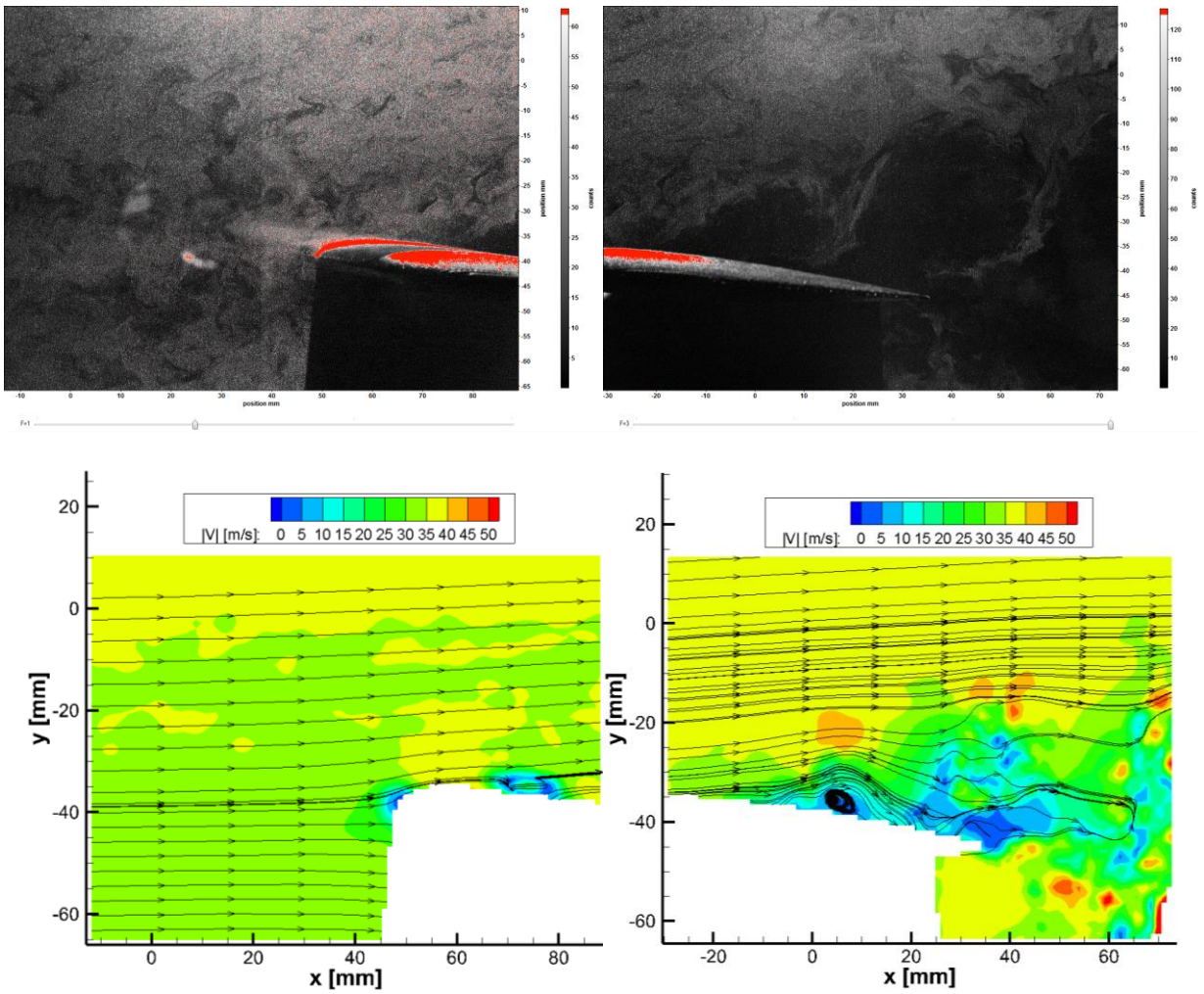

α = 11.3º↓, x/c = 0.8 (258)

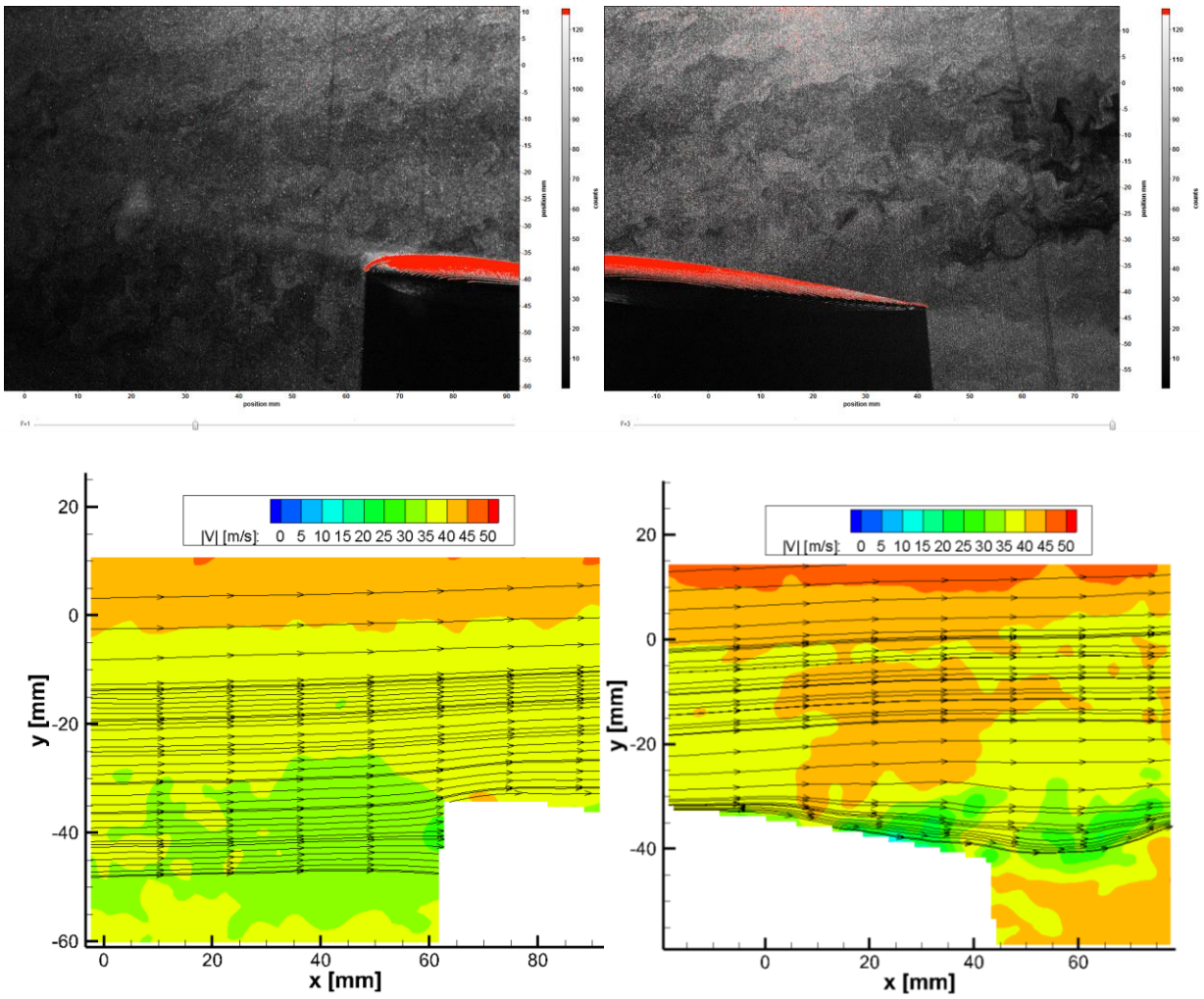

α = 9.8º↓, x/c = 1.0 (379)

APPENDIX D. EXTENDED RESULTS FOR FLOW STRUCTURE OVER Λ=27.6º

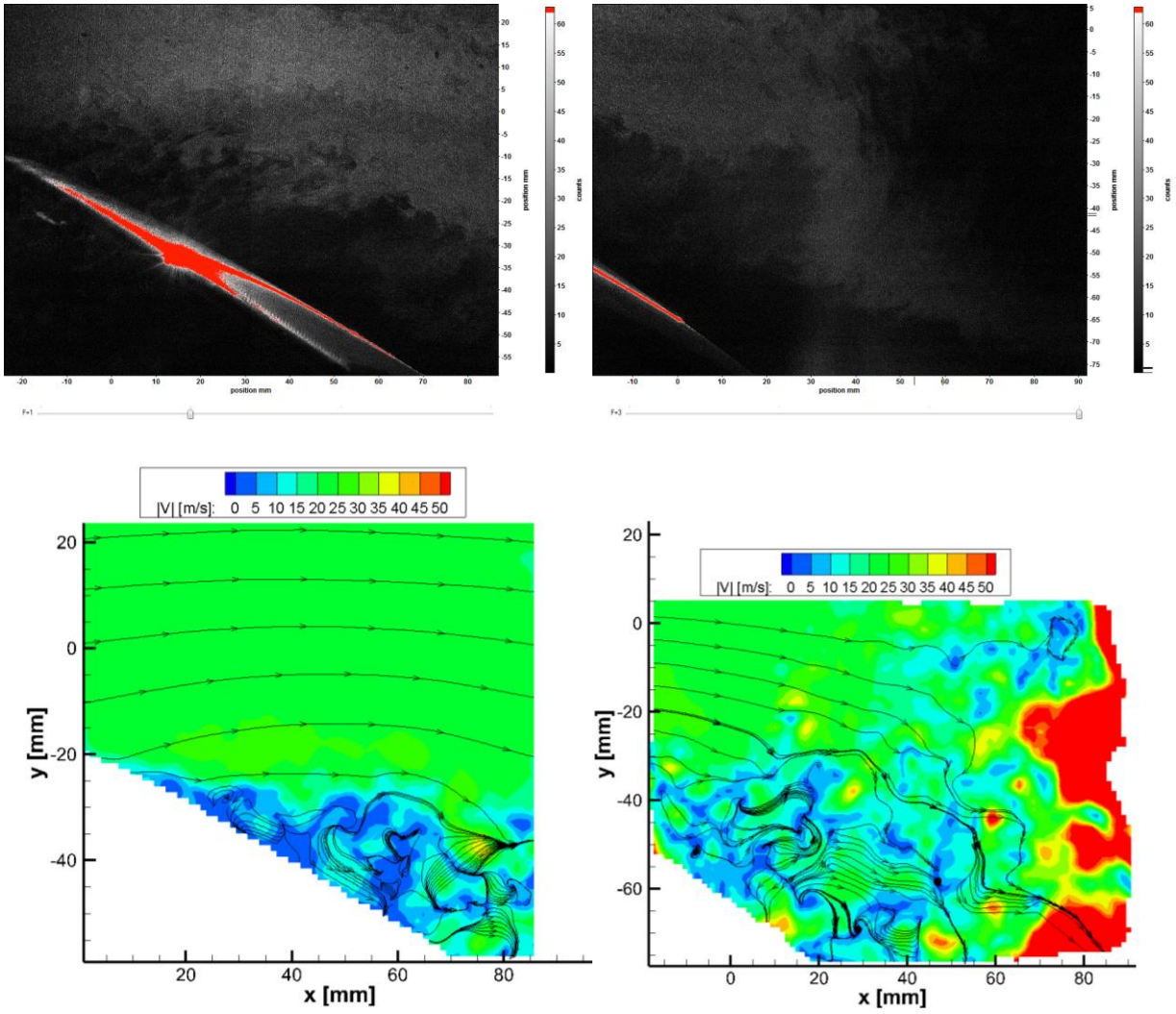

α = 22.5º↑, x/c = 0.6 (372)

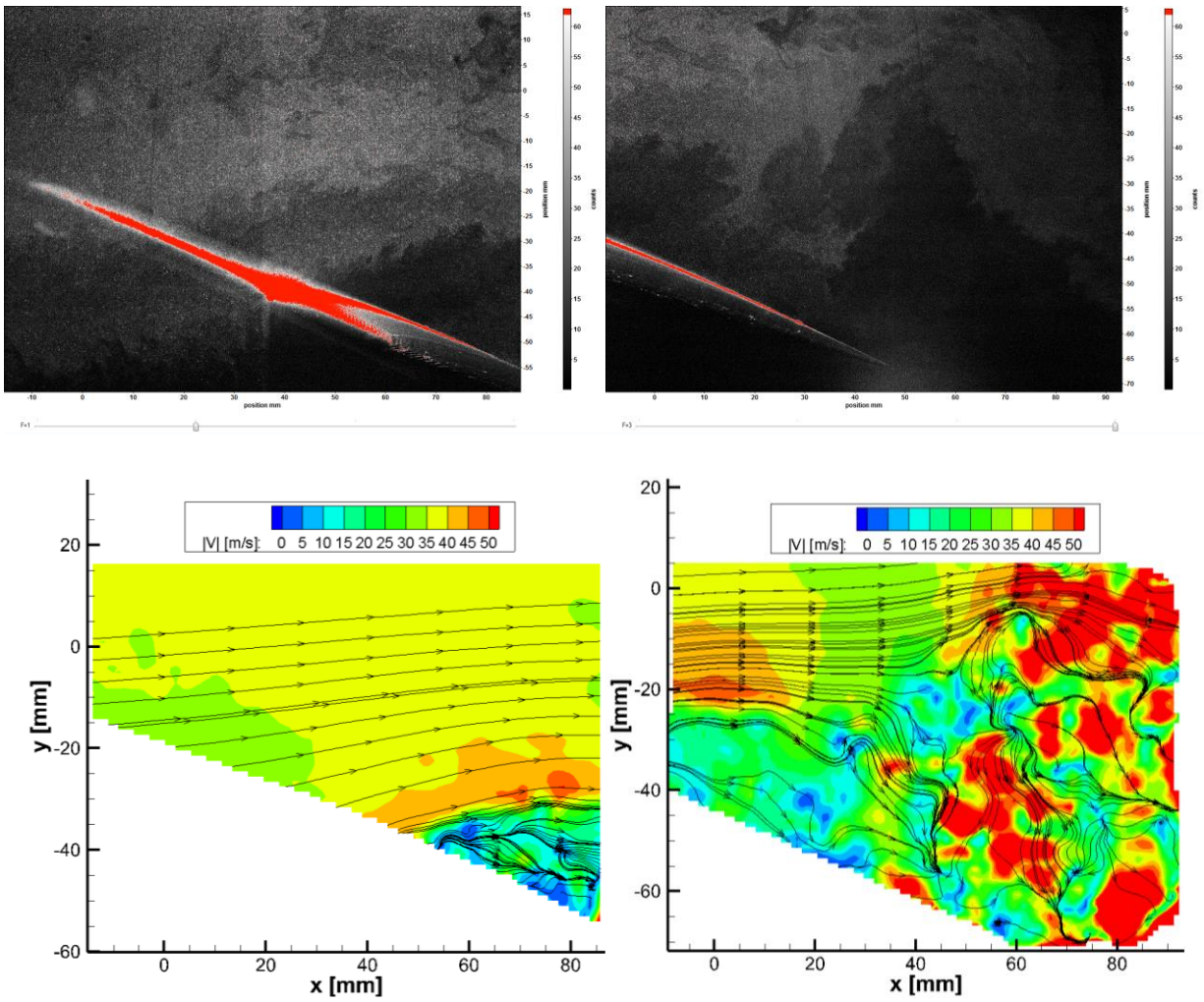

α = 22.3º↑, x/c = 0.8 (120)

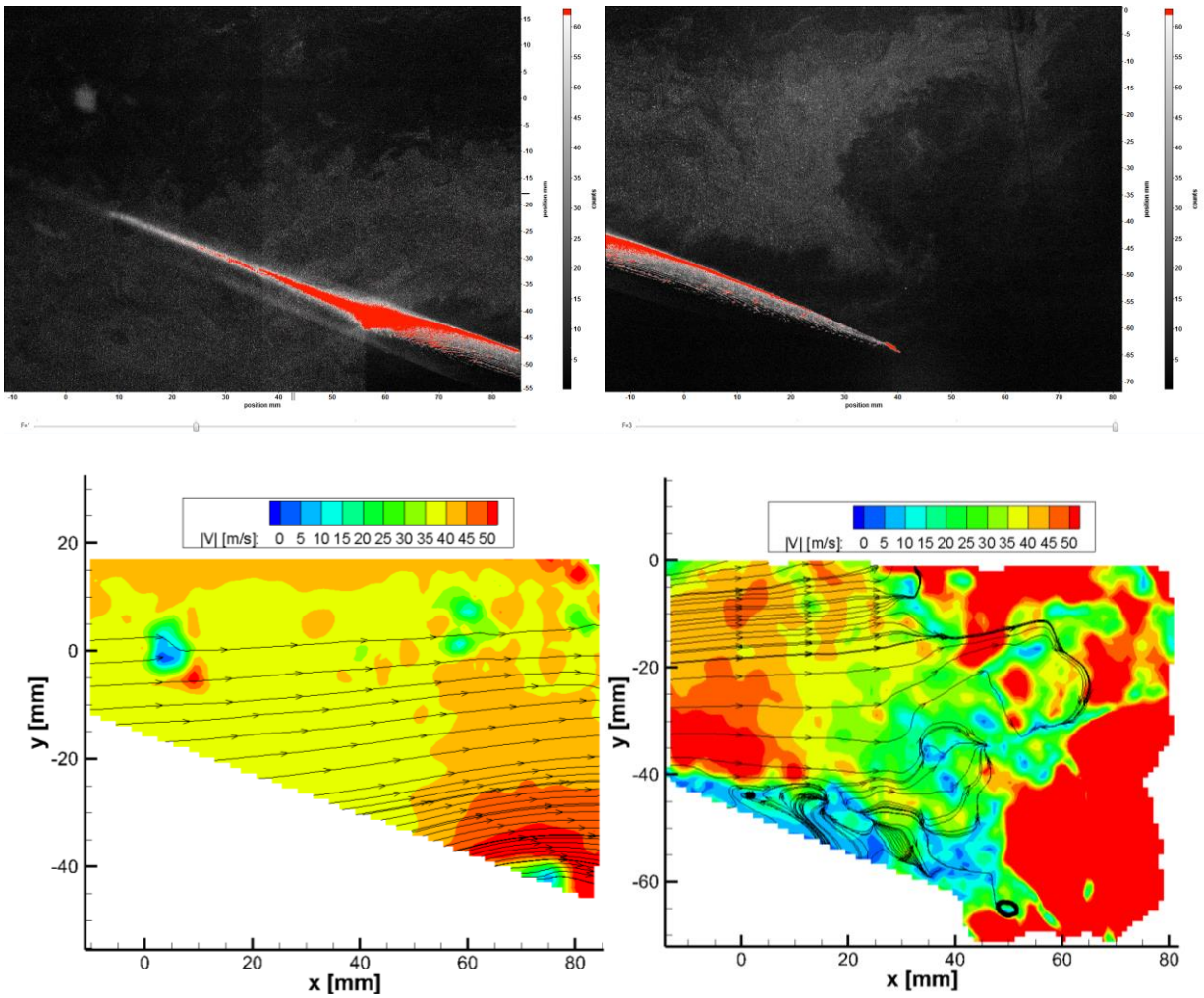

α = 19.1º↑, x/c = 1.0 (271)

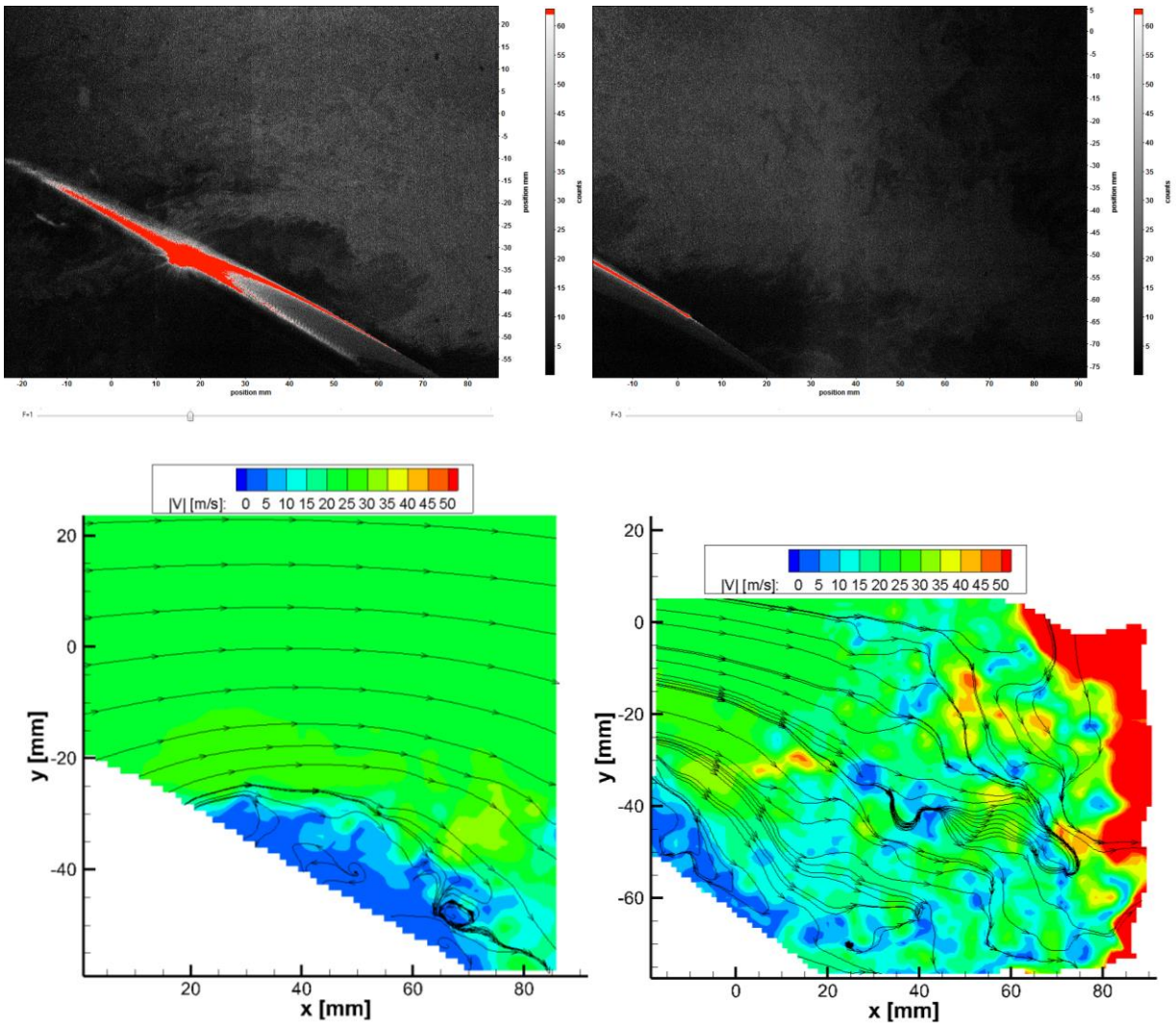

$\alpha = 22.0^{o}\downarrow$, x/c = 0.6 (349)

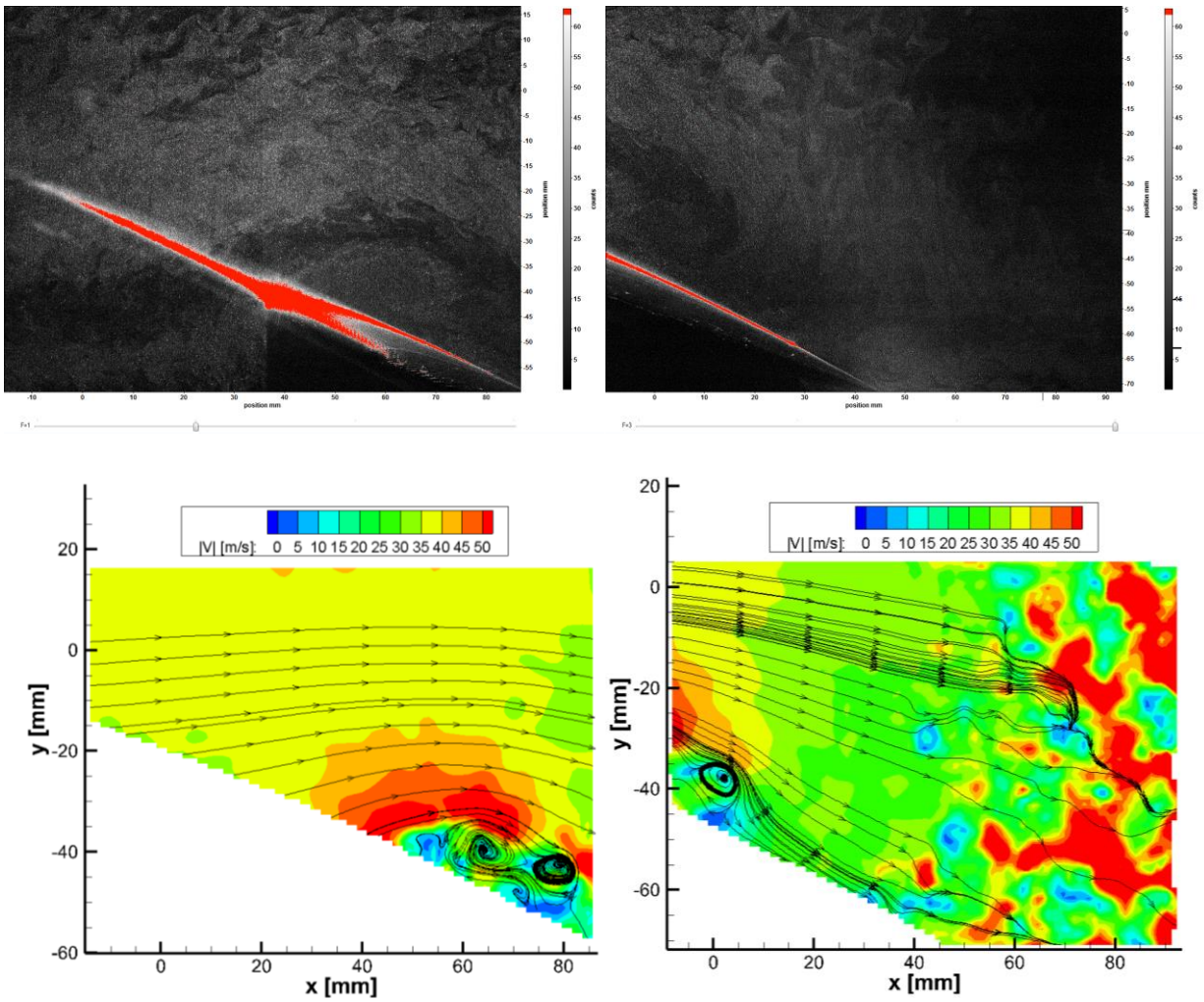

α = 21.9º↓, x/c = 0.8 (134)

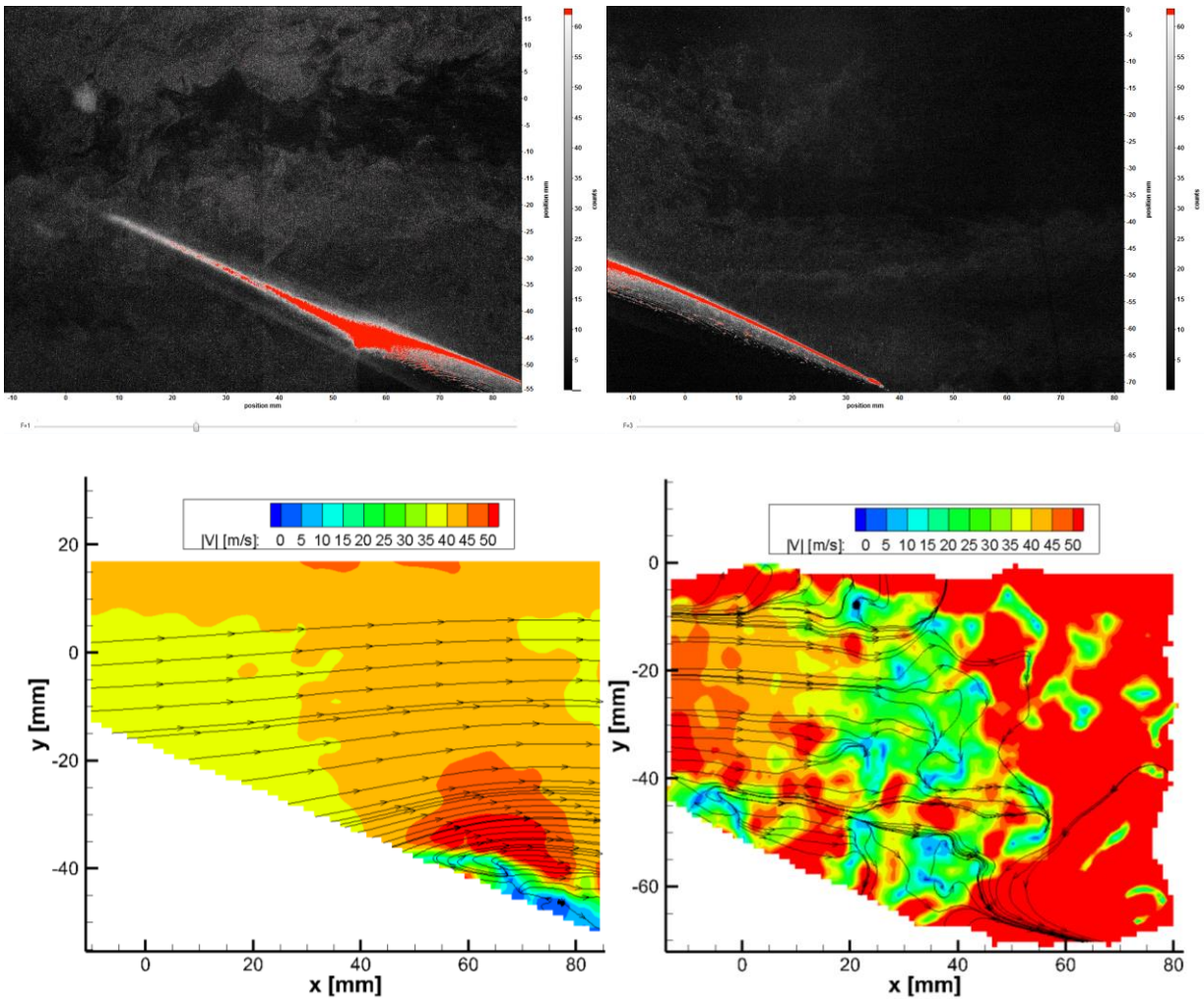

α = 21.9º↓, x/c = 1.0 (291)

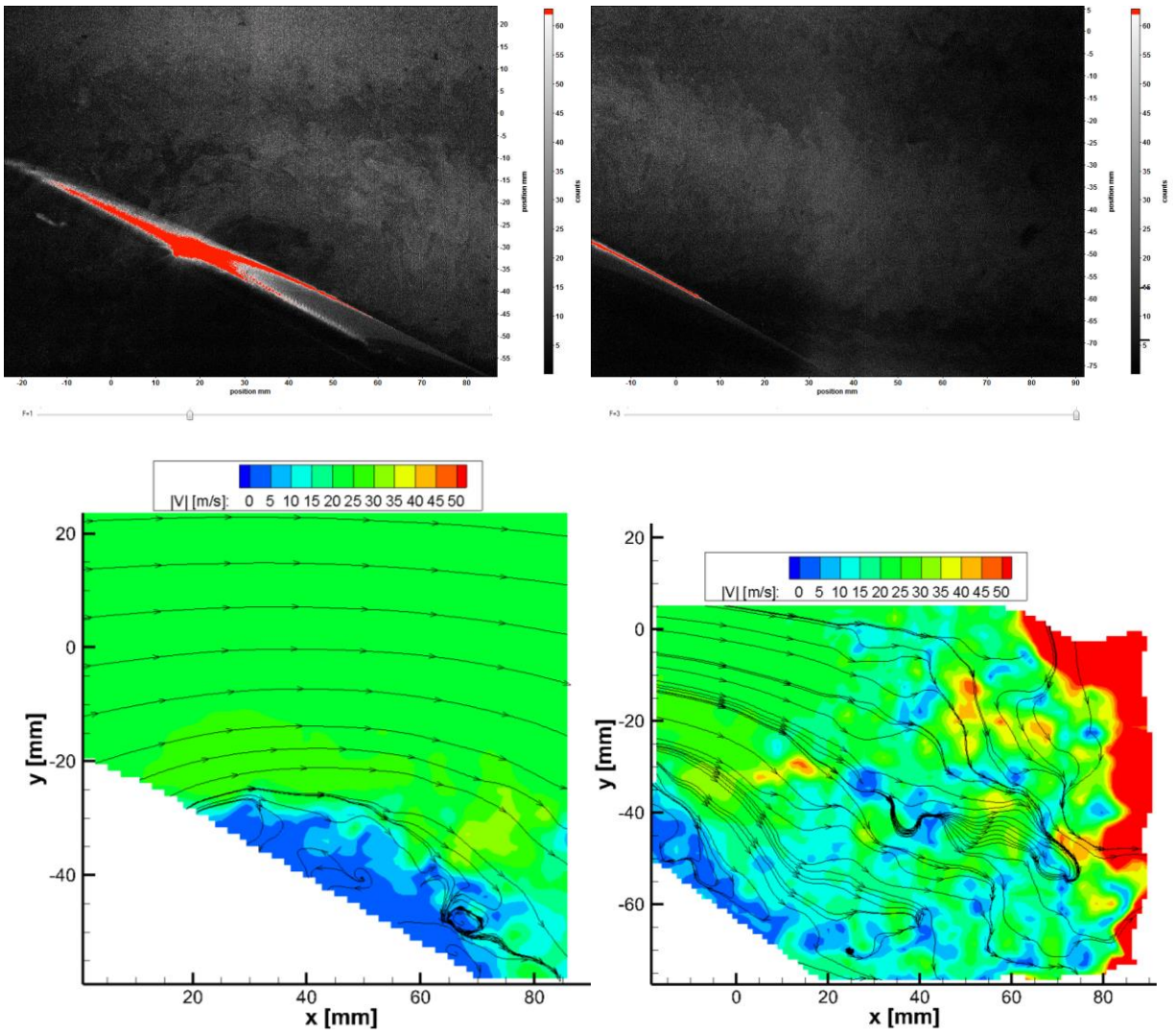

α = 21.1º↓, x/c = 0.6 (198)

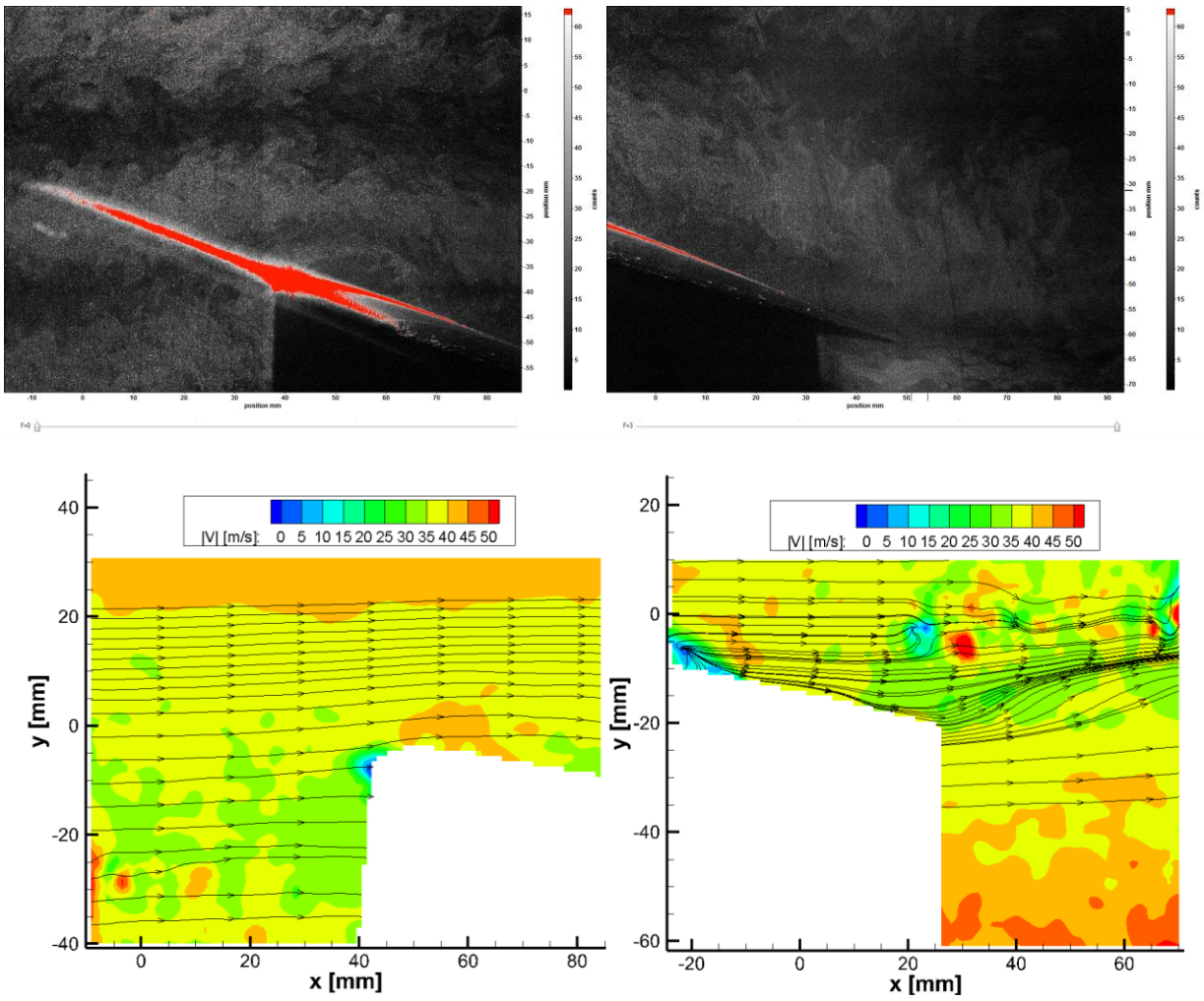

α = 17.3º↓, x/c = 0.8 (136)

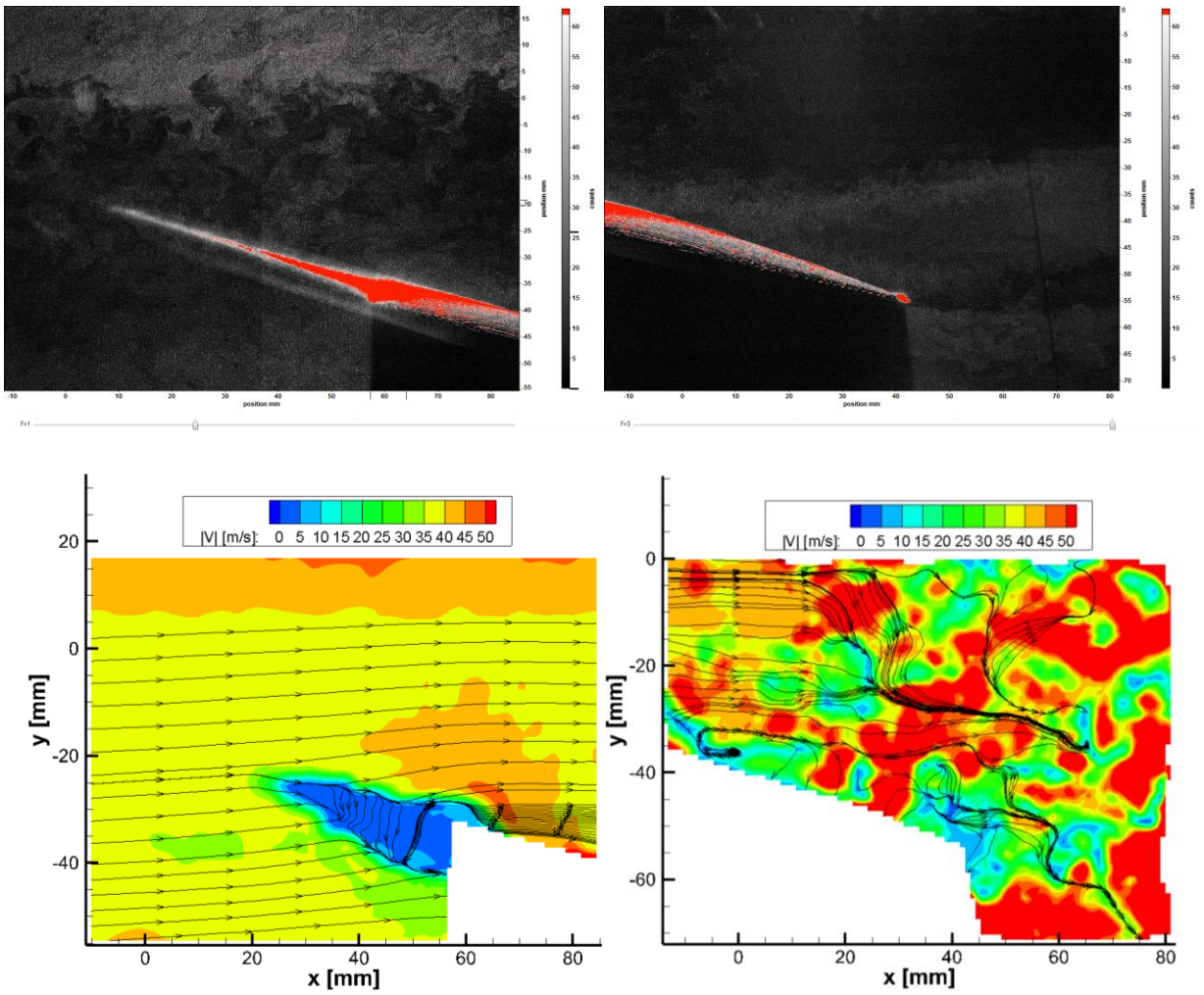

α = 14.3º↓, x/c = 1.0 (297)